DISSECTING FUNCTIONS OF PARTITIONING DEFECTIVE PROTEIN 3 (PARD3) IN CORTICAL DEVELOPMENT

A Dissertation

Presented to the Faculty of the Weill Cornell Graduate School

of Medical Sciences

in Partial Fulfillment of the Requirements for the Degree of

Doctor of Philosophy

by

Wenying Liu

December 2018

DISSECTING FUNCTIONS OF PARTITIONING DEFECTIVE PROTEIN 3 (PARD3) IN CORTICAL DEVELOPMENT

Wenying Liu, PhD

Cornell University 2018

Proper organization and orderly mitosis of radial glial progenitors (RGPs) drive the formation of a laminated mammalian cortex in correct size. However, the molecular underpinnings of the intricate process remain largely unclear. By generating various genetic engineered mouse lines, I investigated the roles of one ancient polarity protein, partitioning defective protein 3 (PARD3), in cortical development.

In the neocortex, the birthplace of excitatory neurons, my mutant analysis showed that RGP behavior and cortical development are controlled by temporally distinct actions of PARD3 in concert with dynamic HIPPO signaling. RGPs lacking PARD3 exhibit developmental stage-dependent abnormal switches in division mode, resulting in an initial over-production of RGPs largely located outside the ventricular zone at the expense of deep-layer neurons. Ectopically localized RGPs subsequently undergo accelerated and excessive neurogenesis, leading to the formation of an enlarged cortex with massive heterotopia and increased seizure susceptibility. Simultaneous removal of HIPPO pathway effectors YAP and TAZ suppresses cortical enlargement and heterotopia formation. These results define a dynamic regulatory program of mammalian cortical development and highlight a progenitor origin of megalencephaly with ribbon heterotopia and epilepsy.

In the medial ganglionic eminence/ preoptic area (MGE/PoA), where most cortical interneurons are born, PARD3 deletion impairs the asymmetric division of RGPs in a temporal-distinct fashion as well, and results in the overproduction of early-born somatostatin (SOM) -expressing interneurons at the expense of constantly generated parvalbumin (PV) -expressing interneurons. Moreover, by analyzing one of the few well-established interneuron subtypes, chandelier cells, I found that the disruption of asymmetric division in MGE/PoA RGPs by PARD3 deletion leads to a significant reduction in the generation of chandelier cells. The results together suggest a putative link between division mode and interneuron subtype specification.

BIOGRAPHICAL SKETCH

Wenying Liu was born in China. She has lived in Beijing for more than 20 years until she earned Bachelor's degree in Pharmaceutical Sciences from Peking University, Beijing, China in 2011.

In the fall of 2011, Wenying enrolled in the BCMB program at the Weill Cornell Graduate School of Medical Sciences of Cornell University in the New York City. There, she joined the laboratory of Dr. Song-Hai Shi in the Department of Developmental Biology at Memorial Sloan Kettering Cancer Center, and carried out her thesis research which focuses on investigating the function of polarity protein, PARD3, in cortical neurodevelopment. Since then, she has published two first-authored papers on Dev. Cell and Genes and Dev, and has another first-authored manuscript under revision. Wenying's thesis work was also selected as an invited talk in the Keystone Symposia Conference on Neurogenesis during Development and in the Adult Brain.

In the summer of 2018, Wenying worked as an intern of Clinical Pharmacology group at Roche, New York, NY. There, she conducted the extensive research on the translational value from preclinical efficacy findings to clinical benefits in the field of small-molecule oncology drugs with the aim of accelerating dose finding during the clinical trials. This experience prompted her to pursue her career in industry after the graduation.

ACKNOWLEDGEMENTS

I would like to, first and foremost, thank my advisor Dr. Song-Hai Shi for giving me the opportunity to join your lab and for your continuous support through my PhD study. You exemplify the virtues of a good researcher: always be passionate, critical, and hardworking. All I learnt from you, as a scientist, will become my treasure and benefit me through my future career.

I am also grateful to all members of the Shi lab, past and present, for their support which makes my thesis research possible over the years. A special thank you goes to Sonia Das for helping me arrange this wonderful thesis defense.

I would like to acknowledge my committee members: Dr. Elizabeth Ross, Dr. Alexandra Joyner for your insightful advice and personal encouragements throughout my PhD training. I want to thank Dr. Zhirong Bao for agreeing on being my examining committee chair on short notice. I am also grateful to my program director, Dr. Mary Baylies for her tremendous help during my thesis defense preparation and internship working permit application. I am extremely fortunate to have your guidance.

Furthermore, I want to thank my mentors during my internship at Roche, Dr. Yu Li, Dr. Bonnie Brennan, and Dr. Peter Morcos. You introduced me to a new world: clinical pharmacology, and inspired me to pursue my future career in industry. I will never forget the nurturing and friendly working environment at Roche and this wonderful internship experience.

Last but definitely not least, I would like to express my deepest gratitude to my family. I want to thank my parents and parents-in-law for their patience and unwavering support during past seven years. I want to thank my little beautiful angel, Huahua, for sparking my life. Most importantly, I want to express my deepest love and thanks to my

husband, Dr. Guanshi Wang. You are the one who is always standing strong by my side and keeping me motivated in difficult times. Without you, I wouldn't make it this far. Please continue taking Huahua and me with you to more exciting future endeavors.

TABLE OF CONTENTS

LIST OF FIGURES

LIST OF TABLES

Chapter 1 PAR proteins: the discovery, molecular identity and cellular functions

1.1 Introduction

The size of different brain regions depends on the size of the contributing proliferative progenitors, which is in turn determined by the mode of progenitors' division. This well-known 'radial unit model' (Rakic, 1988), formulated by Rakic thirty years ago, delineates the crucial roles of neural progenitors in the enlargement of the cerebral cortex during evolution as well as the size difference of distinct brain regions. According to this hypothesis, the number of symmetric proliferative divisions determines the progenitor pool and thereby the surface area of each brain region, whereas the number of asymmetric divisions, which generate neurons during neurogenesis, determines the thickness of the cortex. Indeed, this concept has been well supported through the identification of special neural stem cells, radial glial progenitor xscells (RGPs), and its unique dividing behavior during distinct cortical developmental stages.

Data obtained through various advanced techniques, including immunofluorescent staining, confocal microscopy, time-lapse imaging and surgical manipulation of cortical development identified the existence of RGPs and their temporal distinct division mode in the developing dorsal telencephalon, the birthplace of excitatory neurons. At the early stage of neurogenesis (embryonic day 11-12, E11-12 in mice), RGPs, whose cell bodies reside in the ventricular zone (VZ), largely divide in a symmetric proliferative mode, generating two RGPs to expand the progenitor pool extensively (Florio and Huttner, 2014; Homem et al., 2015; Kriegstein and Alvarez-Buylla, 2009). During the peak phase of neurogenesis, the majority of RGPs switch to

the asymmetric neurogenic division mode to self-renew and simultaneously produce post-mitotic neurons through either direct or indirect way. That is, a given RGP could divide at the VZ surface to produce a daughter RGP as well as either a postmitotic neuron (direct neurogenesis) or an intermediate progenitor cell (IP) which divide symmetrically in the sub-ventricular zone (SVZ) to give rise to two neurons (indirect neurogenesis) (Englund et al., 2005; Noctor et al., 2004; Tamamaki et al., 2001) **(Figure1.1)**. Newborn neurons use the long radial glial fibers of their mother RGPs as scaffolds to migrate along in order to reach their final destination in the cortical plate (Angevine and Sidman, 1961; Hatten, 1999; Marín and Rubenstein, 2003; Noctor et al., 2001; Rakic, 1971, 1988).

RGPs also exist in the medial ganglionic eminence (MGE) and the preoptic area (PoA), the transient structures in the ventral telencephalon where approximately 70% of cortical interneurons are generated. A previous study combining mouse genetics and in utero retrovirus injection elegantly labeled individual dividing progenitors and their progeny in the MGE/PoA. The results indicated that MGE progenitors are radial glial in nature (Brown et al., 2011). Similar to their dorsal counterparts, RGPs in the MGE/PoA undergo interkinetic nuclear migration in the VZ and divide asymmetrically to self-renew and simultaneously produce either a neuron or an IP. The generated IP then migrates into the SVZ and undergoes symmetric division to produce interneurons. Thus, during cortical development, the determinants balancing symmetric proliferative division and asymmetric neurogenic division regulate the area size and thickness of the cortex. Although the dynamic progression in the dividing behavior of RGPs in the embryonic cortex has been well examined, the molecular mechanisms governing division mode switch are not well understood.

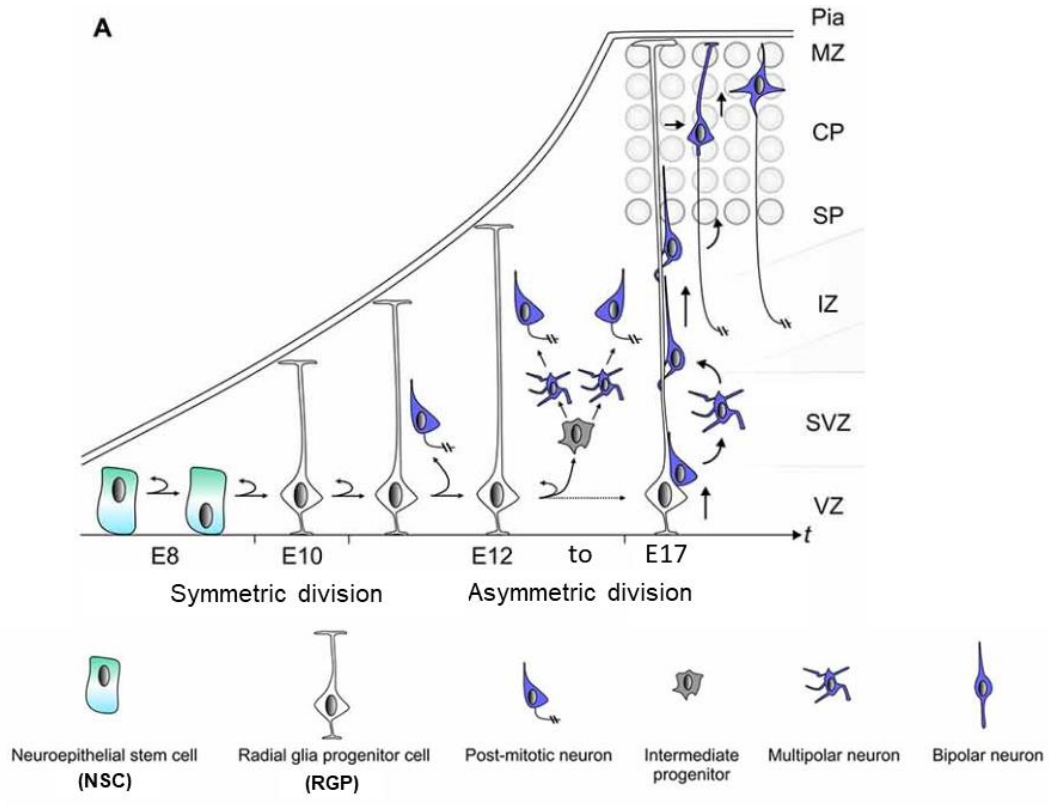

Figure 1.1: Neurogenesis process in cerebral cortex development.

(A) The early neuroepithelium is composed of highly polarized neuroepithelial stem cells (NSCs, apical-basal polarity is indicated). NSCs give rise to RGPs which exhibit even more polarized cellular morphology with an extended basal process. During neurogenesis, symmetric RGP divisions may generate two RGPs but asymmetric divisions produce a renewing RGP and a neuron or an IP. IPs further divide symmetrically in the SVZ to produce neurons. The basal processes of RGPs serve as a scaffold for nascent post-mitotic neurons, which migrate in a step-wise fashion coupled with changes in cell polarity, from the VZ/SVZ through the intermediate zone (IZ) in order to reach the cortical plate (CP). IZ intermediate zone; SP, subplate; CP: cortical plate; MZ: marginal zone. Adapted from Hansen et al, 2017

One promising strategy to probe the mechanisms regulating division mode switch would be to study the characteristics distinguishing RGP from IPs, given the different division mode carried by these two types of neuronal progenitors. One of such characteristics is the apical-basal polarity. RGPs are highly polarized with two characteristic processes: a short apical fiber that contacts the ventricular surface, and a long basal fiber that spans the width of the developing neocortex to reach the pial surface

(Kriegstein and Götz, 2003; Tamamaki et al., 2001). By contrast, IPs lack apical-basal polarity in that extensive studies have shown that IPs are multipolar cells constantly extend and retract various short processes (Noctor et al., 2004; Pontious et al., 2008). Interestingly, the apical domain of RGPs is enriched with the conserved polarity proteins PARD3, PARD6, aPKC (atypical protein kinase C) that is excluded from the basolateral membrane domain through adherens junctions (Afonso and Henrique, 2006; Cappello et al., 2006; Manabe et al., 2002; von Trotha et al., 2006), whereas none of the proteins exist in the IPs. The above-mentioned polarity proteins have been shown to regulate asymmetric division in *C. elegans* zygote and *Drosophila* neuroblast. Scientists were therefore prompted to investigate the function of polarity proteins in regulating division mode of RGPs during cortical neurogenesis (Goldstein and Macara, 2007).

In this chapter, I will introduce, with a focus on PARD3 which is the major player in my thesis, the discovery of par genes, the molecular identity of PAR proteins and their biochemical interactions. The cell biological roles of PAR proteins in *C. elegans* zygote, *Drosophila* neuroblast, and epithelial cells will also be discussed. Finally, I will review several recent studies on the function of PARD3 during neocortical development and discrepancies among their findings, which will serve as the primer for the next two chapters on the function of PARD3 in cortical neurogenesis.

1.2 Early embryonic development in *C. elegans* and the discovery of *par* genes

In this section, I will introduce the seminal genetic screen performed in nematode *C. elegans* zygote leading to the identification of *par* genes. The early embryonic polarity establishment and asymmetric division of *C. elegans* zygote will be discussed first to lay the foundation for understanding the phenotypes of *par* mutants from the genetic screen.

1.2.1 Overview of early embryonic polarity and asymmetric cell division in *C. elegans*

Cell polarity and asymmetric division have been best studied in the first embryonic cell division of *C. elegans*. This is due to not only the features of this animal model, such as short life cycle, big progeny size, and ease of maintenance (Sin et al., 2014), which make it an invaluable tool for genetic screen, but the developing nature of *C. elegans* zygote as well.

From unfertilized oocyte to a juvenile worm, a series of asymmetric divisions accompanied with uneven distribution of cytoplasmic components give rise to five somatic founder cells (AB, MS, E, C and D), one primordial germ cells (P_4), and establish the body plan of *C. elegans* (Sulston et al., 1983). **Figure 1.2** summaries the asymmetries of early embryo. Early in the first embryonic cell cycle, the symmetry of oocyte is broken by the polarity cue provided by the sperm entry from the future posterior pole of the embryo (Goldstein and Hird, 1996; Sadler and Shakes, 2000), and a serious of dramatic cytoplasmic reorganizations begin: (1) cortical cytoplasm streams anteriorly, whereas internal cytoplasm streams posteriorly (Hird and White, 1993). (2) The actomyosin cytoskeleton undergoes rapid rearrangements, leading to localized extensive actomyosin contractility in the anterior cortex which eventually results in the establishment of pseudocleavage furrow at 50% egg length (Rose et al., 1995). (3) The maternal pronucleus migrates toward the paternal pronucleus, the two meet in the posterior hemisphere and move together to the center of the embryo. Subsequently, the P granules, one of the best-known markers of early embryo polarity, start sitting in the posterior cortex, nuclear envelopes break down, the mitotic spindle sets up to the A-P

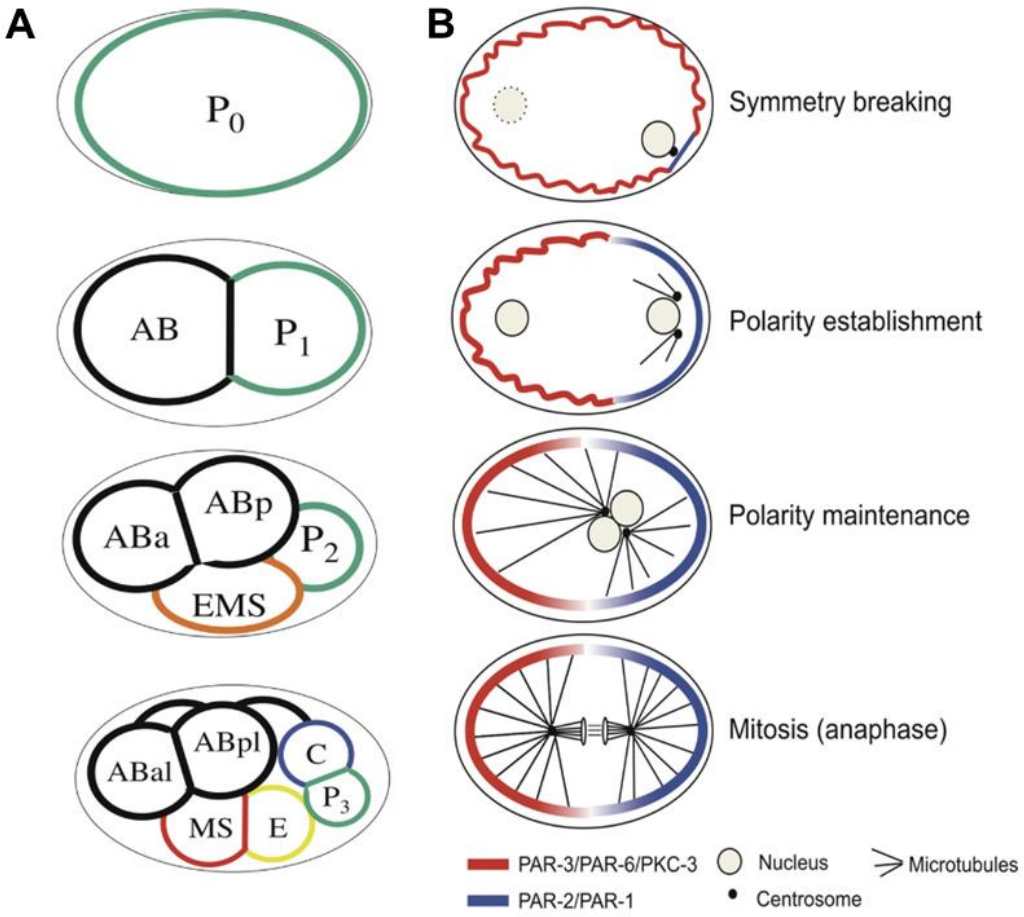

Figure 1.2: Asymmetry of the early *C. elegans* embryo.

Anterior is to the left, posterior is to the right, dorsal is up and ventral is down in this and all subsequent figures. **(A)** Schematic diagram of cell positions at different stages. The germ-line precursors (P cells) are shown outlined with green, and each of the founder cells generated by asymmetric division are indicated with a different color. The daughters of founder cells are named by their position; e.g., ABa is the anterior daughter of AB, whereas ABal is the left daughter of ABa. The embryo proper is surrounded by an eggshell, schematized by a black line. **(B)** Schematics illustrating the anterior-posterior asymmetry in one-cell stage embryos. At symmetry breaking, surface contractions of the cortical actomyosin network (red, wiggled line) cease in the vicinity of the centrosome, resulting in the generation of a small smooth cortical domain (blue, smooth line). During polarity establishment, the smooth cortical area expands anteriorly to eventually reach 50% egg-length. Concomitantly, PAR-3/PAR-6/aPKC expands towards the anterior, whereas PAR-2/PAR-1 retracts from the posterior. During centration/rotation and mitosis, AP polarity is maintained by the mutual inhibition of the anterior and posterior cortical domains. Adapted from WormBook.

axis (Strome and Wood, 1982, 1983). (4) Remarkably, the initially symmetrical spindle becomes polarized during metaphase. While the anterior aster remains firmly associated with cortex, the posterior aster swings from side to side and grows smaller than the anterior one (Albertson, 1984; Kemphues et al., 1988). (5) Morphology of the anterior centrosome becomes distinct from that of its posterior counterpart as mitosis progresses. The anterior centrosome is spherical, whereas the posterior one take on disc-shaped appearance (Hill and Strome, 1988; Keating and White, 1998). (6) Finally, the cleavage furrow bisects the asymmetric spindle, and produces two daughter cells with unequal size, a larger anterior somatic founder cell (AB) and a smaller posterior germ-line cell P1.

1.2.2 The discover of par genes

Thirty years ago, inspired by the ongoing genetic screens in yeast, Kemphues and Preiss set out to perform a series of mutant screen aiming to identify the maternal-effect lethal mutations caused by defective expression of several genes regulating early embryonic polarity and asymmetric division. This seminal work revealed six *par* (*par*-1 to *par*-6, for partitioning-defective) genes (Kemphues, 2000; Kemphues et al., 1988). The phenotypes in one-cell zygote resulted from mutation of these six *par* genes include disruption of pseudocleavage and cytoplasmic streaming, aberrant localization of P-granule, evenly placement of the mitotic spindle. The daughter cells come from first division do not display any polar behavior. In addition, subsequent development is abnormal, with alterations in spindle orientation, dividing timing, and cell fates.

Although the defective expressions of the six *par* genes influence the same processes, their functions are gene-specific (Cheng et al., 1995; Etemad-Moghadam et al., 1995; Kemphues et al., 1988; Morton et al., 1992), which is summarized in **table 1.1.** In particular, *par-3*, the studying subject of my thesis, strongly affects spindle

Table 1.1 Six PAR proteins and aPKC/PKC-3. (adapted from WormBook)

C. elegans	*Drosophila/ Vertebrates* [a]	Protein Distribution[b]	Molecular Nature & Function
PAR-1	Par-1/ MARK1		Serine/Threonine kinase of the MARK family; regulates cytoplasmic asymmetry of MEX-5/6.
PAR-2	-		Ring-finger protein of E3 ligase class; maintains polarity established by NMY-2 flows; in absence of flows, establishes polarity through microtubule-dependent mechanism.
PAR-3	Baz/ Pard3		Multiple PDZ-domain scaffold protein; recruits PAR-6 and PKC-3; excludes PAR-1 and PAR-2 from the anterior; required for all downstream asymmetries.
PAR-4	Lkb1/ STK11		Serine/Threonine kinase; modulates size of anterior/posterior polarity domains.
PAR-5	14-3-3ζ/ 14-3-3ε,ζ		14-3-3 protein; modulates size of anterior/posterior polarity domains and prevents their overlap.
PAR-6	Par-6/ Pard6		PDZ Domain protein; acts with PAR-3 to exclude PAR-1 and PAR-2 from the anterior; required for all downstream asymmetries.
PKC-3	aPKC/ PKCζ	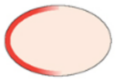	Atypical protein kinase C; acts with PAR-3 to exclude PAR-1 and PAR-2 from the anterior; required for all downstream asymmetries.

orientation in the AB cell, while exerts a weaker effect on P-granule localization (Etemad-Moghadam et al., 1995). Furthermore, *par-3* mutation shares many similar phenotypes to *par-6*, and PAR-3 protein was found to function as a complex with PAR-6 and aPKC in regulating polarity and asymmetric division through extensive later studies (Tabuse et al., 1998; Watts et al., 1996).

The identification of *par* genes revealed a set of machinery at the heart of cell polarization in one-cell phase of *C. elegans* embryo, pioneered the study on polarity and asymmetric division regulation, and prompted scientists to explore the biochemical interactions and cellular biological roles of par proteins.

1.3 Molecular identity of PAR proteins and their biochemical interactions

In this section, I will discuss the molecular identity and biochemical interactions of Par proteins, with a focus on PAR-3/PAR-6/aPKC complex given the context of this

dissertation. In the end of the section, evolution conservative roles of this complex will also be touched upon for the transition to the next section.

1.3.1 Molecular identity of PAR proteins

Shortly after the discovery of par genes, Kemphues and coworkers successfully cloned all six par genes between 1994 and 2002 (Etemad-Moghadam et al., 1995; Guo and Kemphues, 1995; Hung and Kemphues, 1999; Levitan et al., 1994; Morton et al., 1992; Watts et al., 1996). The sequences suggested distinct molecular identity of each gene, which together could constitute a novel intracellular signaling pathway. PAR-1 and PAR-4 are categorized into the family of serine threonine kinase. PAR-5 encodes a 14-3-3 like protein. PAR-3 and PAR-6 have PDZ domains but lack enzymatic structure, suggesting that they could act as a scaffold to recruit signaling proteins. PAR-2 has a RING finger domain and is involved in the ubiquitination pathway.

The suggested molecular identity initially failed to link PAR proteins to any cellular components, such as microtubule and molecular motors, that have been proved to drive asymmetry of C. elegans embryo development. Among all six PAR proteins, only PAR-1 has a distant relative which functions in yeast to mediate cell polarization (Tassan and Le Goff, 2004). Therefore, for the most part, the PAR proteins appeared to form a new signaling pathway, which makes the further study of PAR protein localization and biochemical interactions a necessity to understand their cellular roles.

1.3.2 PAR-3 protein domains and their functions

Studies on cellular localization of PAR proteins might bring some insight into functions of these proteins: while PAR-3 and PAR-6 are restricted in the anterior cortex, PAR-1 and PAR-2 become enriched in the opposite end of *C. elegans* zygote. PAR-4

and PAR-5 distribute in a symmetric pattern, and are both cortical and cytoplasmic through the period (Kemphues, 2000). It is likely appeared that PAR proteins drive their asymmetric distribution by establishing the polarized localization of cellular components. The results prompt a series of studies investigating PAR protein domains. In this section, given the context of my thesis, I will specifically discuss the well-studied domains on PAR-3 protein and their functions.

Figure 1.3 demonstrates the domain organization and interaction network of

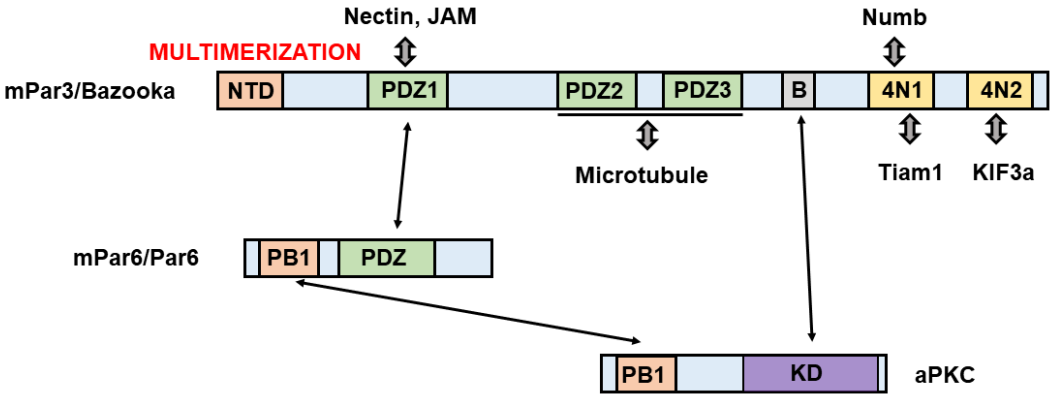

Figure 1.3: The domain organization and interaction network of PAR complex.

PAR complex is composed of three members: mPar3/Bazooka, mPar6/Par6 and aPKC. Their domain organization and interaction network are shown here. Solid lines with double arrow heads represent the direct association between two proteins. NTD: N-terminal domain; B: aPKC binding site; KD: kinase domain.

PAR-3 protein. PAR-3 is composed of a conserved N terminal domain (NTD, also called CR1), 3 PDZ domains, and the C-terminal region containing multiple protein binding sites (Benton and St Johnston, 2003; Mizuno et al., 2003). NTD mediates self-oligomerization of PAR-3, and thus leads to the enrichment of PAR-3/PAR-6/aPKC. complex and its binding partners at specific membrane locations (Feng et al., 2007). The first PDZ domain of PAR-3 is reported to bind with several cell adhesion molecules (CAMs) including junction adhesion molecule (JAM), nectin and p75 (Chan et al., 2006; Ebnet et al., 2003; Itoh et al., 2001; Takekuni et al., 2003). These interactions are

likely to signal the membrane targeting of PAR-3. The first PDZ domain is responsible for PAR-6 recruitment as well via a PDZ-PDZ interaction (Joberty et al., 2000; Lin et al., 2000; Suzuki et al., 2001). The two PDZ domains downstream of PDZ1 element, through binding with lipid membranes, are crucial for the localization of PAR-3 at tight junction (TJ) and establishing the apical-basal polarity in Drosophila and mammalian epithelial cells (Wu et al., 2007; Yu and Harris, 2012). The third PDZ domain itself is reported to directly bind with phosphatase and tension homolog (PTEN), and thus makes PAR-3 an ideal platform for PIP signaling events during cell polarization (Feng et al., 2008). One previous study from our lab also reported the strong microtubule binding and bundling activity of N-terminal of PARD3 (mammalian homolog of PAR3), and disruption of this activity would impair neuronal axon specification (Chen et al., 2013).

The C-terminal region of PAR3 consists of an aPKC binding site and two conserved elements named 4N1 and 4N2. The coiled-coil domain 4N1 interacts with the endocytic adaptor protein Numb, and thus contributes to cell migration (Nishimura and Kaibuchi, 2007). Membrane lipids are found to bind with 4N1 as well for the cortical localization of PAR-3 (Krahn et al., 2010). 4N1 is also capable of Rac1- specific guanine nucleotide exchange factor (GEF) Tiam 1/2, and regulates TJ formation during axon/dendrite development in neuronal system (Chen and Macara, 2005; Nishimura et al., 2005; Zhang and Macara, 2006). The 4N2 domain is required for neuronal polarization by binding with microtubule motor KIF3A (Nishimura et al., 2004). Our lab reported an intra-molecular auto-inhibition mechanism of PAR-3 in which C-terminal half suppresses microtubule bundling activity of PAR3 by binding with N-terminal domain (Chen et al., 2013).

In addition to distinct roles played by distinct domains of PAR-3, it is reported, in *C. elegans*, that different domains are required at different stages during development:

NTD and PDZ2 function only during early embryogenesis while aPKC binding site is important in later development (Li et al., 2010).

1.3.3 Evolutionary conservation of PAR proteins

Roles of PAR proteins in cell polarization were exclusively in *C. elegans* until 1998. In 1998, bazooka, a fly cell polarization gene, was cloned and found to encode a protein closely related to PAR-3 (Kuchinke et al., 1998). In the same year, a mammalian PAR-3 homolog, PARD3, that can form a complex with aPKC was found to adopt an apical-basal asymmetric localization in mammalian epithelial cells, and resulted in the identification of aPKC as a member of anterior PAR complex in *C. elegans*, like PAR-3 and PAR-6 (Izumi et al., 1998; Tabuse et al., 1998). One year later, mammalian PAR-3, PAR-6 and aPKC were reported to exist in a complex with CDC42 (Joberty et al., 2000; Lin et al., 2000), an ancient small GTPase that was first discovered in budding yeast (Johnson, 1999). Members of this asymmetrically distributed complex were also found in Xenopus oocytes and ascidian embryonic cells (Nakaya et al., 2000; Patalano et al., 2006). The other PAR proteins turned out to be highly conserved as well, and to play critical roles in cell polarization and asymmetric division in diverse contexts. All the above identifications suggest that PAR proteins have fundamental and conserved functions in animal cell polarization and asymmetric division.

In the next section, I will introduce the roles of PAR complex played in various systems including *Drosophila* neuroblast development, epithelial polarization, and asymmetric division of RGPs.

1.4 The Fundamental Roles of PAR Complex in Animal Cell Polarization and Asymmetric Division

1.4.1 PAR complex in *Drosophila* neuroblast asymmetric division

In the *Drosophila* embryonic central nervous system (CNS), progenitor cells called neuroblasts (NBs) undergo programmed asymmetric cell division to generate the diversity of cell fates. During embryogenesis, NBs delaminate from the epithelium layer and enter mitosis. Upon cytokinesis, each NB produces two daughter cells with distinct properties: a bigger apical cell which maintains a NB identity and continue to divide in a progenitor-like way, whereas the smaller basal daughter cell becomes a ganglion mother cell (GMC) and adopts a terminal division fashion to give rise to two postmitotic neurons or glial cells (Betschinger and Knoblich, 2004; Chia and Yang, 2002; Jan and Jan, 2001).

The evolutionary conserved PAR complex consisting of Bazooka (Baz, the fly homolog of C. elegans par-3), PAR6 and aPKC mediates the establishment of apical-basal polarity and asymmetric division of NBs. Once a NB delaminates from the epithelium, 'apical stalk', a special cellular structure was formed to keep the association between NB and the surrounding epithelial cells. The PAR complex binds with NB-specific protein Inscuteable (Insc) to form the Insc/PAR complex and establish the apical-basal polarity in delaminating NB (Schaefer et al., 2000). During mitosis, Insc/PAR complex is restricted in the apical cortex as a crescent and recruits another conserved polarity complex, which is composed of Partner of Inscuteable (Pins) and the heterotrimetic G protein subunit Gαi (Parmentier et al., 2000; Yu et al., 2000). Insc/PAR works together with Pins/ Gαi complex and regulates the asymmetric division of NB.

Interestingly, Insc/PAR and Pins/ Gαi complexes have distinct primary roles. Whereas Pins/ Gαi plays critical roles in mitotic spindle orientation, Insc/PAR is involved in the basal localization of cell fate determinants, such as Prospero (Pros), Numb, and their adaptor proteins Miranda (Mira) and Partner of Numb (Pon) (Izumi et al., 2004; Schober et al., 1999; Wodarz et al., 1999). The key member of PAR complex, aPKC, can limit basal protein, Lethal giant larvae (Lgl), to basal area through phosphorylation as well (Ohshiro et al., 2000; Peng et al., 2000). Non-phosphorylated Lgl normally is restricted at the basal cortex of NBs in an active state and attracts basal cell-fate determinants. Upon entering the anterior region, the territory guarded by Insc/PAR complex, Lgl is phosphorylated and inactivated by aPKC, and thus be pushed back to posterior end (Betschinger and Knoblich, 2004).

1.4.2 PAR complex in epithelial polarization

The apical-basal polarity establishment is fundamental to the epithelial sheets. During organogenesis, the internal sheets fold into villi, cysts and duct, and external sheets form the contact surface between the organism and surrounding environment. Epithelial cells can also form junctions with their neighbors in order to control ions and molecules' permeability. PAR complex is reported to control epithelial polarization throughout the metazoa. In *C. elegans*, the apical-basal polarity replaces the antero-posterior asymmetry by the end of the four-cell stage of embryogenesis, during which PAR-3 and PAR-6 become localized to the apical surface and mediate the apical-basal polarity associated with gastrulation (Nance et al., 2003). In *Drosophila* epithelial cells, the fly ortholog of PAR3 can be both functionally and spatially separated from PAR6 and aPKC. It localizes at the adherens junctions which is below PAR6 and aPKC, acts upstream of CDC42 which plays a crucial role in localizing PAR6/aPKC at the cell cortex (Kuchinke et al., 1998). PAR3 drives polarity establishment and maintenance

through the interactions with two other sets of polarity proteins including Crumbs (CRB) and Scribble (SCRB)/Discs-large (DLG)/Lethal-giant-larvae (LGL) complex. The SCRB group suppresses apical membrane identity on the basolateral surface by inhibiting PAR3, whereas PAR complex maintains the integrity of apical domain via recruiting CRB, which antagonizes the function of SCRB at the apical surface (Bilder et al., 2003; Tanentzapf and Tepass, 2003). PAR3 complex is also known to keep PAR1 off the apical surface in fly as well. Once phosphorylated by aPKC from PAR complex, PAR1 is forced to bind with PAR5, which suppresses the kinase activity of PAR1 and blocks its membrane binding capability. Conversely, PAR3 that diffuses down to the basal region, the territory of PAR1, is phosphorylated by this basal polarity protein, and similarly forced to bind PAR5 and is excluded from basal domain (Hurov et al., 2004). *Drosophila* PAR3 is also involved in controlling phosphoinositide metabolism. In fly photoreceptor epithelial cells, PAR3 binds to the phosphoinositide phosphatase PTEN, recruits it to the lateral adherens junctions, and thus results in an enrichment of PIP_3 on the apical surface, which is required for microvilli organization (von Stein et al., 2005). PAR3 works in an independent fashion in mammalian MDCK epithelial cells as well. In these cells, PARD3 sits predominantly to the tight junctions to maintain apical-basal polarity, whereas PAR6 and aPKC localize on the apical surface and in the cytoplasm (Izumi et al., 1998).

1.4.3 PAR complex in mammalian embryonic neocortical neurogenesis

By taking advantage of shRNA knockdown method, two elegant studies have investigated the function of PARD3 during mammalian embryonic neocortical neurogenesis (Bultje et al., 2009; Costa et al., 2008). Costa and coworkers revealed the strong enrichment of PARD3 at the apical surface of the VZ at E12, and the gradually reduction in the expression level at ensuing development stages. By performing *in utero*

injection of PARD3 shRNA-containing lentiviral vectors into the lateral ventricle of E12 mouse embryos, they reported PARD3 knockdown forces the transduced RGPs to exit the cell cycle, and hence differentiated into deep-layer neurons at the expense of superficial neuron generation. On the other hand, PARD3 overexpression drives over-proliferation of RGPs by keeping them in an undifferentiated state. One year later, our lab published a paper in which more detailed investigation into the function of PARD3 was conducted. This paper revealed the dynamic distribution of PARD3 in RGPs, and identified a direct association between asymmetric division of RGPs and PARD3. Upon examining the expression pattern of PARD3 at distinct cell phase, the authors reported a temporal distinct distribution pattern of PARD3: Whereas PARD3 exhibits preferential localization at ring-like junction structures in RGPs during interphase, it delocalized from the junction and become more dispersed in the cytosol of RGPs during mitosis. Furthermore, the authors discovered the asymmetric distribution of PARD3 in most of E14 dividing RGPs, and hence the uneven inheritance of PARD3 by the two daughter cells generated by RGPs. Next the authors modified the level of PARD3 either by RNAi knockdown or by overexpression, and analyzed its role in regulating daughter cell fate specification and asymmetric cell division, they found that although both manipulations impair asymmetric division in E14 RGPs, the outcome of generated daughter cell fate is rather different. While PARD3 depletion results in symmetric terminal division and thus an increase in neuronal differentiation, overexpression triggers the presence of PARD3 in both daughter cells, and forces them become RGPs.

Although both studies reported the division mode switch of RGPs from asymmetric division to symmetric terminal division upon PARD3 knockdown, the results are somehow the opposite of the studies done in zebrafish neural system (Alexandre et al., 2010; Dong et al., 2012). Whether the discrepancy simply comes from

the species difference? Is there a better way to investigate the function of endogenous PARD3 protein in asymmetric division of RGPs? Since RGPs serve as the neuronal progenitors in all regions of the central nervous system, what is the function of RGPs' asymmetric division in other brain areas? Can PARD3 still be a conserved player regulating the division mode of RGPs in the regions other than neocortex? The first two questions set the foundation of the first part of my thesis work (chapter 2), in which the genetic PARD3 conditional knockout mouse model was used to study the function of this protein during neocortical development. Question 3 and 4 trigger the second part of my study (chapter 3), which is to explore the role of PARD3 during interneuron development.

Chapter 2 [1]PARD3 dysfunction in conjunction with dynamic HIPPO signaling drives cortical enlargement with massive heterotopia

2.1 Introduction

The cerebral cortex is responsible for all higher-order brain functions, such as sensory perception, motor control, and cognition. A defining feature of the cortex is its lamination. Individual laminae or layers are segregated largely by cell type and neuronal connections (Greig et al., 2013; Kwan et al., 2012). Therefore, laminar formation is of central importance to both the structural and functional development of the cortex. Cortical lamination relies on the intricate organization and behavior of radial glial cells, the principal progenitor cells responsible for producing neurons as well as glia in the cortex (Anthony et al., 2004; Florio and Huttner, 2014; Homem et al., 2015; Kriegstein and Alvarez-Buylla, 2009; Malatesta et al., 2000; Miyata et al., 2001; Noctor et al., 2001, 2004; Tamamaki et al., 2001). Radial glial progenitors (RGPs) possess a highly characteristic morphology with the cell body located in the ventricular zone (VZ), a long radial glial fiber extending to the pia, and a short ventricular endfoot reaching the lateral ventricle (Rakic, 2003). Moreover, the cell bodies of RGPs in the VZ are organized in a pseudostratified manner and the neighboring ventricular endfeet form junctions at the luminal or apical surface of the VZ (i.e., the VZ surface) (Bultje et al., 2009; Chenn et al., 1998).

---

[1]Liu WA, Chen S, Li Z, Lee CH, Mirzaa G, Dobyns WB, Ross ME, Zhang J, and Shi SH. **PARD3 dysfunction in conjunction with dynamic HIPPO signaling drives cortical enlargement with massive heterotopia**. Genes Dev. 32: 763-780 (2018).

During cortical development, RGPs actively divide at the VZ surface. At the early stage (e.g., before embryonic day 11-12, E11-12, in mice), RGPs largely undergo symmetric proliferative division to amplify the progenitor pool (Florio and Huttner, 2014; Homem et al., 2015; Kriegstein and Alvarez-Buylla, 2009). After that, RGPs predominantly undergo asymmetric neurogenic division to self-renew and simultaneously produce neurons either directly or indirectly via transit amplifying progenitors (TAPs), such as outer subventricular zone RGPs (oRGs; also known as basal RGPs or intermediate RGPs) and intermediate progenitors (IPs) that further divide in the subventricular zone (SVZ) (Betizeau et al., 2013; Englund et al., 2005; Fietz et al., 2010; Hansen et al., 2010; Haubensak et al., 2004; Kelava et al., 2012; Noctor et al., 2004; Reillo et al., 2011; Wang et al., 2011). RGPs also produce short neural precursors located in the VZ (Gal et al. 2006). While IPs are the predominant TAPs in the developing mouse cortex, additional types of TAPs with expanded neurogenic capacity are more abundant in the developing ferret and primate cortices (Betizeau et al., 2013; Fietz et al., 2010; García-Moreno et al., 2012; Geschwind and Rakic, 2013; Hansen et al., 2010). Towards the late stage, RGPs mostly undergo terminal neurogenic or differentiation division to exit the cell cycle, whereas a defined fraction remains proliferative to produce glial cells (Anthony et al., 2004; Gao et al., 2014; Kessaris et al., 2006; Noctor et al., 2004). Newborn neurons migrate radially along the mother radial glial fiber to progressively constitute future cortical layers in a birth date-dependent inside-out manner (Angevine and Sidman, 1961; Hatten, 1999; Marín and Rubenstein, 2003; Noctor et al., 2001; Rakic, 1971, 1988; Thomsen et al., 2016). Early-born neurons occupy deep layers, whereas late-born neurons occupy superficial layers.

The orderly processes of neurogenesis and neuronal migration supported by RGPs orchestrate the intricate development of the cortex to the correct size and form. In particular, asymmetric division of RGPs represents an elaborate balance of

proliferation and differentiation and is responsible for producing virtually all cortical neurons. However, the molecular underpinnings of RGP organization and asymmetric division remain poorly understood. Previous studies in C. elegans and Drosophila have identified key molecular pathways that control asymmetric cell division (Doe et al., 1998; Jan and Jan, 2001; Kemphues, 2000; Knoblich, 2008; Wodarz and Huttner, 2003). Among them, the evolutionarily conserved Partitioning defective (PARD) protein complex, consisting of PARD3, PARD6, and atypical protein kinase C (aPKC), is at the top of the genetic regulatory hierarchy (Johnson and Wodarz, 2003). Notably, the PARD complex is abundantly expressed in the developing vertebrate nervous system (Manabe et al., 2002). Despite the fact that the PARD complex represents an essential entry point of dissecting the molecular control of vertebrate neural progenitor asymmetric division, its precise function in vertebrate neural progenitor remains debated (Alexandre et al., 2010; Bultje et al., 2009; Costa et al., 2008; Dong et al., 2012). Thus far, a genetic deletion analysis of *Pard3* in the mammalian brain has not yet been conducted. Moreover, the key signaling pathway that mediates the action of PARD3 in controlling RGP division behavior and orderly cortical development is largely unknown.

Disruptions in neurogenesis and neuronal migration are well-known to cause cortical malformations and human diseases. Early defects in RGP division lead to brain growth dysregulation and changes in cortical size, such as microcephaly (small brain) and megalencephaly (large brain) (Bizzotto and Francis, 2015). On the other hand, aberrant neuronal migration results in cortical heterotopia, such as periventricular heterotopia (PH; neurons located along the ventricles) and subcortical band heterotopia (SBH; neurons located in the white matter under the cortex) (Bielas et al., 2004; Ross and Walsh, 2001). Interestingly, these abnormalities may co-exist in complex forms. For example, there have been individuals reported with megalencephaly and massive subcortical ribbon-like heterotopia, distinct from the classic SBH (Barkovich et al.,

2012). The compound abnormalities in volume increase and massive heterotopia represent new types of human cortical malformations that are currently poorly understood.

In this study, we found that loss of PARD3 in mouse cortical RGPs causes severe malformations of the cortex, including increased volume, systematic and drastic changes in neuronal subtype composition, and massive ribbon-like heterotopia. These defects in neuronal production and organization arise progressively from temporally distinct abnormal RGP mitotic behaviors regulated by dynamic HIPPO as well as NOTCH signaling. The mutant mice exhibit elevated seizure susceptibility. Interestingly, simultaneous removal of Yes-associated protein (YAP) and Transcriptional co-activator with PDZ-binding motif (WWTR1/TAZ), two essential effectors of the HIPPO pathway, suppresses cortical enlargement and giant heterotopia formation caused by PARD3 loss. Together, our findings define a key molecular program controlling RGP behavior and cortical organization and provide insights into unusual cortical malformation characterized by megalencephaly with giant ribbon-like heterotopia and epilepsy.

2.2 Results

2.2.1 *Pard3* deletion in RGPs leads to an enlarged cortex with giant SBH

To dissect the molecular control of RGP organization and division underlying mammalian cortical development, we generated a conditional *Pard3* mutant mouse line, *Pard3*$^{fl/fl}$ (fl, floxed; see Methods), and crossed it to the *Emx1-Cre* mouse line, in which Cre recombinase is selectively expressed in RGPs of the developing cortex starting at ~embryonic day (E) 9.5 (Gorski et al., 2002). While PARD3 was abundantly expressed in RGPs, especially at the VZ surface, in the littermate wild type control cortex, it was depleted in the VZ of the *Emx1-Cre;Pard3*$^{fl/fl}$ conditional knockout (referred to as *Pard3*

cKO hereafter) cortex at E12.5 **(Figure 2.1A, arrows and insets)**. The residual PARD3 expression near the pial surface was likely from migrating interneurons originated from the ventral telencephalon or post-mitotic neurons produced prior to *Cre* recombination **(Figure 2.1A, asterisks)**. Western blot assay also showed a drastic loss of PARD3 expression in the *Pard3* cKO cortex compared to the control **(Figure 2.1B)**. Notably, while PARD3 was ablated in RGPs, no obvious defects in junction organization and centrosome localization at the VZ surface were observed at this stage **(Figure 2.2A-D)**.

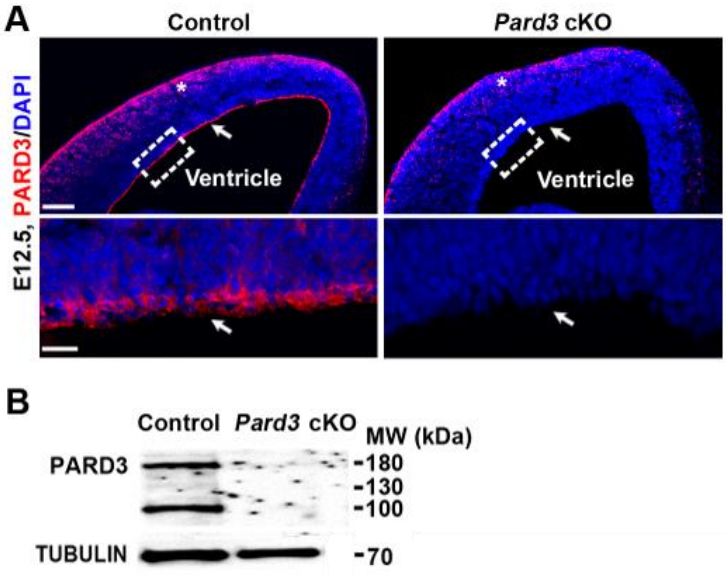

Figure 2.1: PARD3 protein is selectively deleted in the neocortical RGPs in *Pard3* cKO brains.

(A) Representative confocal images of E12.5 control and *Pard3* cKO cortices stained for PARD3 (red) and counter-stained for DAPI (blue). High-magnification images of the VZ surface (broken line rectangles and arrows) are shown at the bottom. Asterisks indicate the residual PARD3 signal in the cortical plate likely in migrating interneurons originated from the ventral telencephalon or post-mitotic neurons produced prior to the *Cre* recombination. Scale bars: 150 μm (top) and 20 μm (bottom). (B) Western blot assay of PARD3 expression in control and *Pard3* cKO cortices using an antibody against the N-terminus of PARD3. Note that the expression of both the long (~180 KDa) and short (~100 KDa) isoforms of PARD3 is largely abolished in the *Pard3* cKO cortex.

Figure 2.2: *Pard3* deletion does not disrupt junction integrity initially.

(A) Representative confocal images of E12.5 control and *Pard3* cKO cortices stained for centrosomal marker PCNT (red) and junction marker ZO-1 (green) and counter-stained for DAPI (blue). High-magnification images of the VZ surface (broken line rectangles) are shown at the bottom. Note no obvious junction disruption in the *Pard3* cKO cortex at this stage. Scale bars: 20 μm (top) and 10 μm (bottom). **(B, C)** Representative confocal images of E12.5 control and *Pard3* cKO cortices stained for N-CADHERIN (green, D) and β-CATENIN (red, E), and counter-stained for DAPI (blue). Scale bars: 10 μm. **(D)** Representative confocal images of control and *Pard3* cKO cortices stained for centrosomal marker PCNT (green) and junction marker ZO-1 (red), and counter-stained for DAPI (blue) at E13.5 (left), E15.5 (middle) and E17.5 (right). Arrows indicate the junction disruption at E15.5 and E17.5. Scale bar: 30 μm.

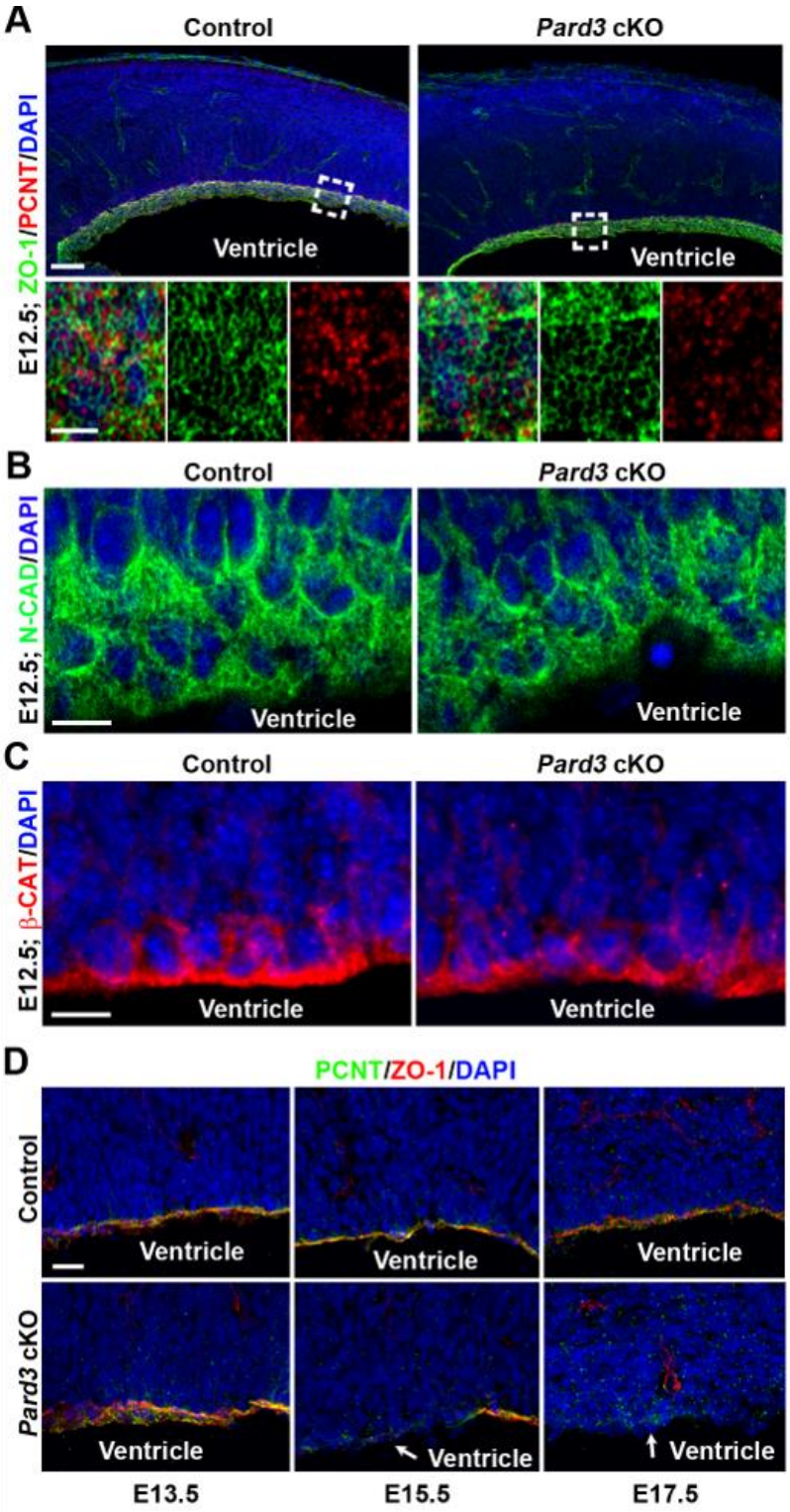
A
Control
Pard3 cKO
E12.5; ZO-1/PCNT/DAPI
Ventricle
Ventricle
B
Control
Pard3 cKO
E12.5; N-CAD/DAPI
Ventricle
Ventricle
C
Control
Pard3 cKO
E12.5; β-CAT/DAPI
Ventricle
Ventricle
D
PCNT/ZO-1/DAPI
Control
Pard3 cKO
Ventricle
Ventricle
Ventricle
Ventricle
Ventricle
Ventricle
E13.5
E15.5
E17.5

Pard3 cKO mice were born at the expected frequency and survived to adulthood. The brain of *Pard3 cKO* mice appeared similar to that of littermate control mice at postnatal day (P) 21-30 **(Figure 2.3A)**. However, histological examination revealed a striking phenotype in the *Pard3* cKO cortex compared with the control **(Figure 2.3B)**. A massive ribbon-like tissue mass was found underneath an apparently layered but thinner cortex. The heterotopic cortical tissue ('HC', asterisks) exceeded the seemingly normotopic cortex ('NC') in thickness in the mediodorsal region, where the expression of Cre recombinase initiates (Gorski et al., 2002; Li et al., 2003), and the overall cortical region was thicker in the *Pard3 cKO* brain than in the control **(Figure 2.3B, right)**.

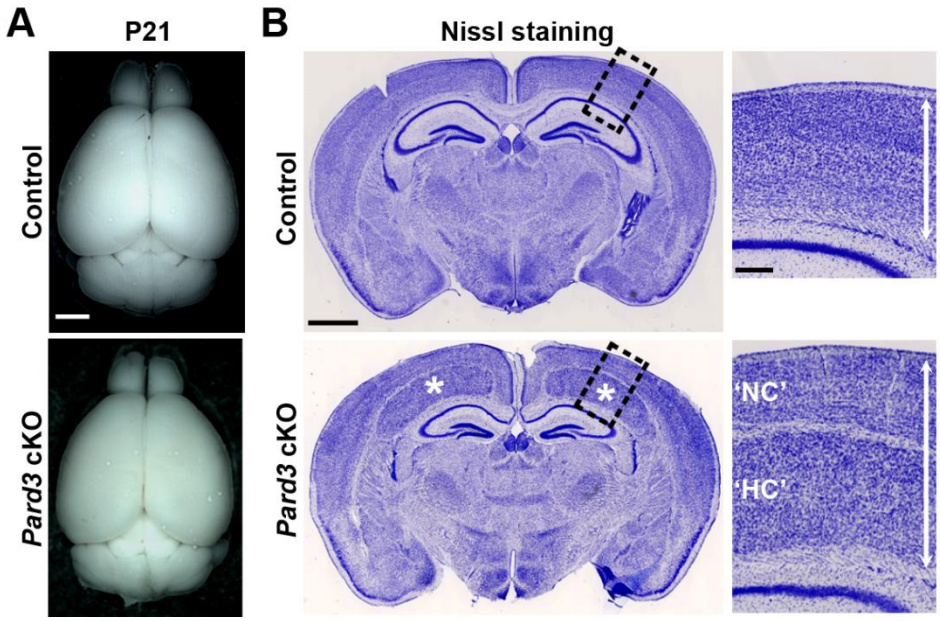

Figure 2.3: *Pard3* deletion in RGPs leads to an enlarged cortex with giant SBH.

(A) Representative whole-mount images of control and *Pard3* cKO brains at P21. Scale bar: 2.5 mm. **(B)** Representative Nissl staining images of the control and *Pard3* cKO brain coronal sections at P21. Asterisks indicate the giant heterotopia. High-magnification images of the cortex (broken lines) are shown to the right. Double-headed arrows indicate the overall thickness of the cortex. 'NC' stands for the normotopic cortex and 'HC' stands for the heterotopic cortex. Scale bars: 1.25 mm (left) and 25 μm (right).

Given that the 'NC' and 'HC' in the *Pard3 cKO* brain harbored the neural progeny of cortical RGPs marked by *Emx1-Cre*, they were both considered as the cortical tissue. Of note, selective deletion of *Pard3* in post-mitotic neurons using the *Nex-Cre* mice (Schwab et al. 2000) did not cause any obvious defect in cortical development **(Figure 2.4A-D)**. Together, these results suggest that selective removal of PARD3 in RGPs, but not in post-mitotic neurons, leads to a thicker cortex with massive ribbon-like heterotopia.

To determine whether the heterotopia in the *Pard3* cKO cortex represents PH or SBH, we stained brain sections with antibodies against SMI-312 (green), a pan-axonal neurofilament protein, and ISOLECTIN B4 (red) that labels blood vessels **(Figure 2.5)**. We found that the heterotopia was surrounded by the axonal fibers and contained blood vessels, indicative of SBH in nature. No obvious change in the number of blood vessels was observed **(Figure 2.5)**, consistent with the fact that Cre is not expressed in blood vessels in *Emx1-Cre*. In line with the increase in cortical thickness, the whole-brain magnetic resonance imaging (MRI) analysis showed that the cortical volume in the *Pard3* cKO brain including the giant heterotopia (orange, asterisks) was substantially larger than that of the control **(Figure 2.6A-C)**. These results demonstrate that PARD3 removal in RGPs results in an enlarged cortex with giant SBH.

2.2.2 *Pard3* cKO mice display increased seizure susceptibility

Cortical heterotopia is often associated with epilepsy in humans (Watrin et al., 2015). Mice with cortical heterotopia show different seizure susceptibilities depending on the genetic mutations (Croquelois et al., 2009; Gabel et al., 2013). To examine the seizure susceptibility of adult (3-4 months old) *Pard3* cKO and littermate control mice, we administered pilocarpine, a commonly used chemoconvulsant for seizure induction

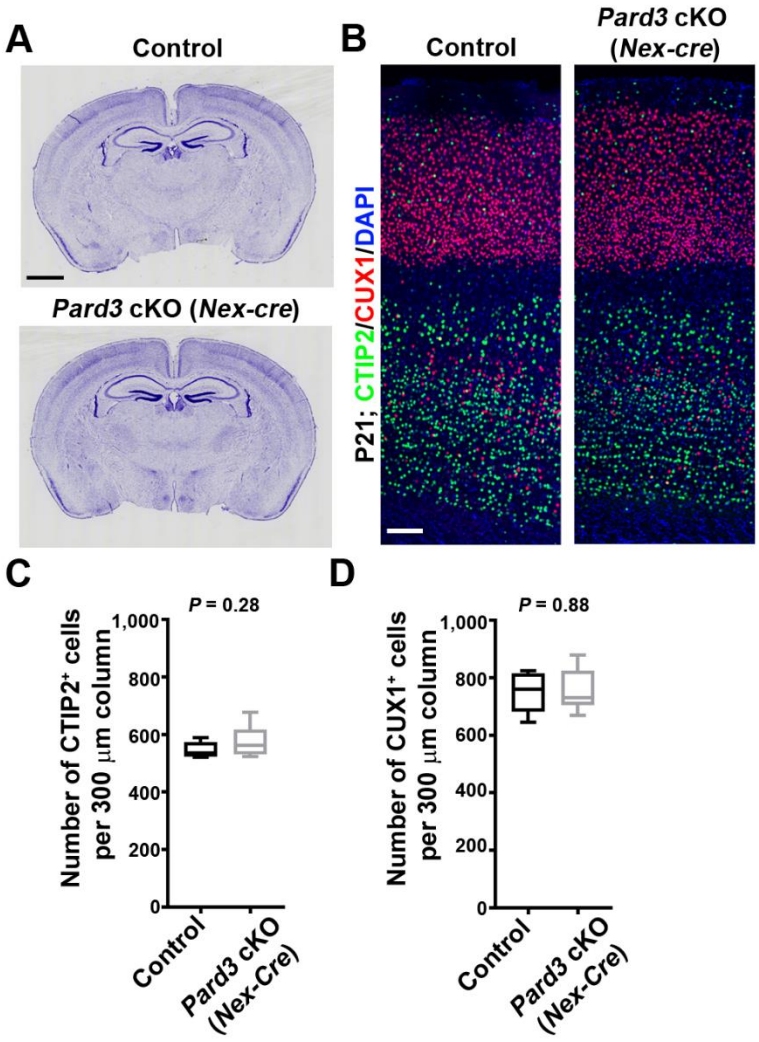

Figure 2.4: *Pard3* deletion in postmitotic neurons fails to result in the giant heterotopia.

(A) Representative Nissl-stained images of P21 control and *Nex-Cre;Pard3* cKO brain coronal sections. Not on obvious defect in cortical development in the *Nex-Cre;Pard3* cKO brain. Scale bar: 1.25 mm. **(B)** Representative confocal images of P21 control and *Nex-Cre;Pard3* cKO cortices stained for layer V/VI neuronal marker CTIP2 (green) and layer II-IV neuronal marker CUX1 (red), and counter-stained with DAPI (blue). Scale bars: 70 μm. **(C, D)** Quantification of the number of $CTIP2^+$ cells (C) and $CUX1^+$ cells (D) per 300 μm radial column in control and *Nex-Cre;Pard3* cKO mice at P21 (n=6 per genotype; unpaired two-tailed t-test with Welch's correction). Box-whisker plot: center line, median; box, interquartile range; whiskers, minimum and maximum.

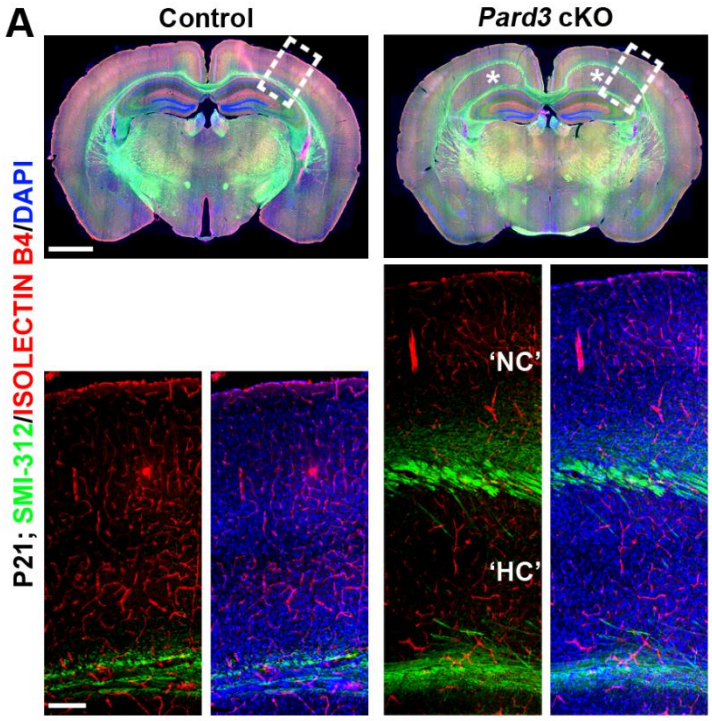

Figure 2.5: The heterotopia in the *Pard3* cKO cortex represents SBH.

(A) Representative confocal images of P21 control and *Pard3* cKO coronal sections stained for pan-axonal neurofilament marker SMI-312 (green), and blood vessel marker ISOLECTIN B4 (red), and counter-stained with DAPI (blue). High-magnification images of the cortices (broken line rectangles) are shown at the bottom. Asterisks indicate the giant SBH. Note the two axonal tracts surrounding the SBH and the abundance of blood vessels within the SBH. Scale bars: 150 μm (top) and 70 μm (bottom).

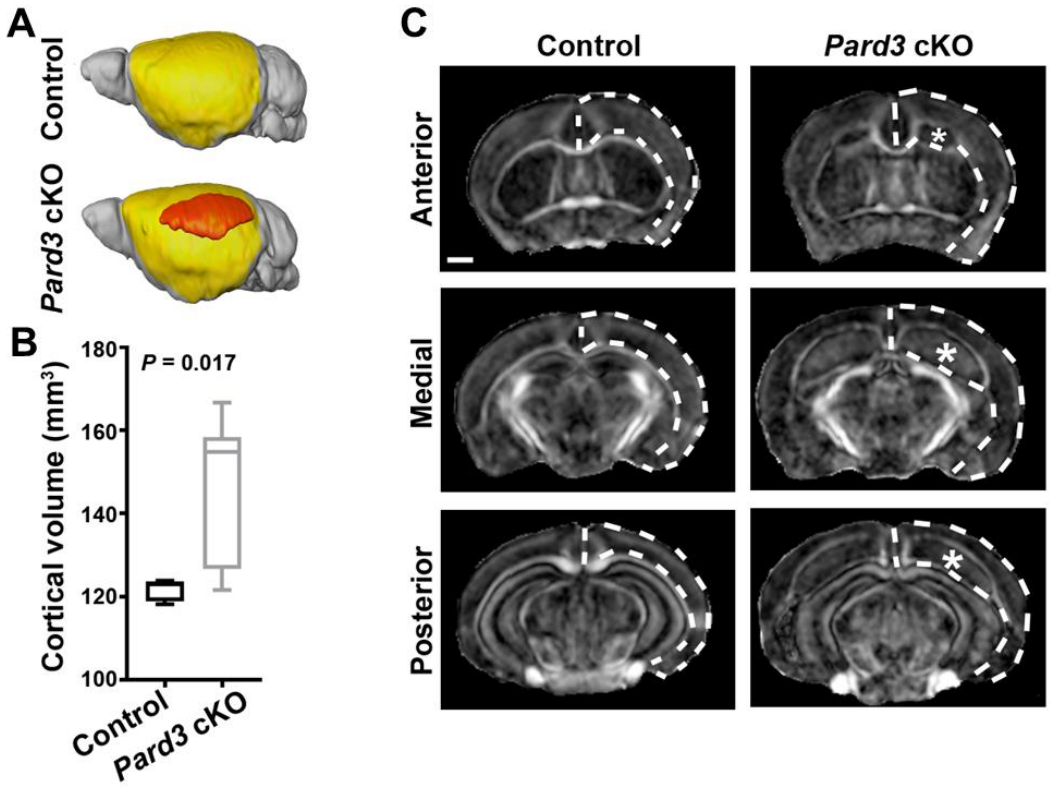

Figure 2.6: The whole-brain magnetic resonance imaging (MRI) analysis of the *Pard3* cKO cortex.

(A) Three-dimensional rendering images of the control and *Pard3* cKO brains at P21 based on MRI data. The normotopic cortex is highlighted in yellow and the heterotopia is highlighted in orange. **(B)** Representative fractional anisotropy (FA) maps of the control and *Pard3* cKO brains at P21 along the rostrocaudal axis. Broken lines indicate the overall cortical tissue, and asterisks indicate the giant heterotopia. Scale bar: 1 mm. **(C)** Quantification of the whole cortical volume (n=7 brains per genotype; unpaired two-tailed t-test with Welch's correction). Box-whisker plot: center line, median; box, interquartile range; whiskers, minimum and maximum.

(Kandratavicius et al. 2014), to animals and continuously monitored their behavioral response for 100 minutes **(Figure 2.7)**. Remarkably, all five *Pard3* cKO mice began to seize as soon as 10 minutes post injection and progressed to severe seizure behaviors ranging from violent convulsions to generalized seizures that lasted for 30-60 seconds, and two of them died from the seizures towards the end of the observation period. In contrast, none of the littermate controls exhibited severe seizure symptoms similar to

that of *Pard3* cKO mice. While three out of five control mice developed mild clonic episodes such as single or multiple short jerks for 1-2 seconds, the other two mice did not show any obvious seizure-like activity throughout the entire period. These results suggest that *Pard3* cKO mice exhibit increased seizure susceptibility compared with the control.

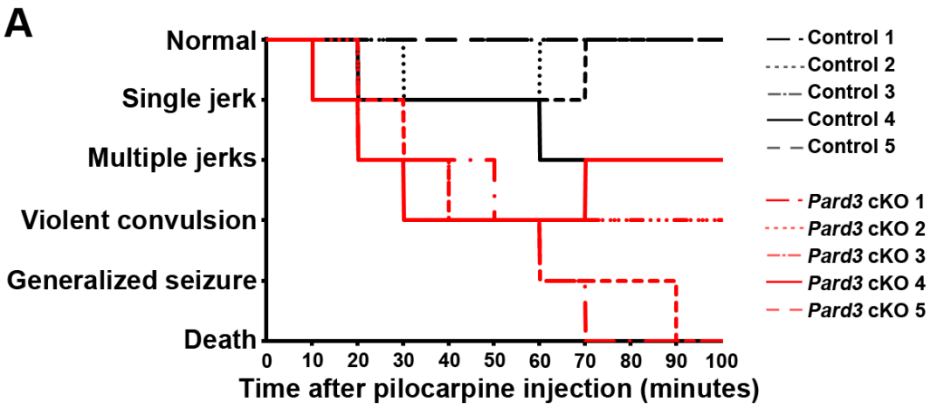

Figure 2.7: *Pard3* cKO mice display increased seizure susceptibility.

(A) Behavioral responses of the control (black lines, n=5) and *Pard3* cKO (red lines, n=5) mice at 3-4 months of age upon pilocarpine administration.

2.2.3 Systematic alterations in neuronal composition in *Pard3* cKO cortex

The enlarged cortex in the *Pard3* cKO brain including the NC and HC indicates abnormalities in neuronal production. To determine this, we stained P21 brain sections with antibodies against FOXP2 **(Figure 2.8A)**, a layer VI neuronal marker, or SATB2 **(Figure 2.8C)**, a pan-neuronal marker with enrichment in superficial layers (Greig et al. 2013). As expected, $FOXP2^+$ neurons were predominantly located in the deep layer VI in the control cortex **(Figure 2.8A, left)**. Notably, a much thinner band of $FOXP2^+$ neurons in the NC, in addition to a few scattered ones in the HC, was found in the *Pard3* cKO brain **(Figure 2.8A, right)**. The density as well as the total number of $FOXP2^+$ neurons was significantly decreased in the *Pard3* cKO cortex compared with the control

Figure 2.8: *Pard*3 deletion leads to systematic alterations in neuronal composition in the cortex.

(A) Representative confocal images of P21 control and *Pard3* cKO cortices stained for layer VI neuronal marker FOXP2 (green) and counter-stained with DAPI (blue). Scale bar: 70 μm. **(B)** Quantification of the number of $FOXP2^+$ cells per 300 μm radial column in control and *Pard3* cKO mice at P21 (n=4 brains per genotype; unpaired two-tailed t-test with Welch's correction). **(C)** Representative confocal images of P21 control and *Pard3* cKO cortices stained for layer II/III/V neuronal marker SATB2 (red) and counter-stained with DAPI (blue). Scale bars: 70 μm. **(D)** Quantification of the number of $SATB2^+$ cells per 300 μm radial column in control and *Pard3* cKO mice at P21 (n=4 brains per genotype; unpaired two-tailed t-test with Welch's correction). **(E)** Representative images of P21 control and *Pard3* cKO cortices stained for layer V/VI neuronal marker CTIP2 (green) and layer II-IV neuronal marker CUX1 (red), and counter-stained with DAPI (blue). Scale bars: 70 μm. **(F)** Quantification of the number of $CTIP2^+$ (left) and $CUX1^+$ (right) cells per 300 μm radial column in control and *Pard3* cKO mice at P21 (n=4 brains per genotype; unpaired two-tailed t-test with Welch's correction). **(G)** Quantification of the relative ratio of the respective neuronal (FOXP2, CTIP2, SATB2, and CUX1) numbers in *Pard3* cKO versus control cortices (n=4 brains per genotype; Chi-square test for linear trend). Note a progressive change in neuronal composition. **(H)** Percentage of $FOXP2^+$ (blue), $CTIP2^+$ (red), and $CUX1^+$ (green) cells in control and 'NC' and 'HC' of *Pard3* cKO cortices at P21 (n=4 brains per genotype; Chi-square test). Data are presented as mean ± SEM. For all box-whisker plots: center line, median; box, interquartile range; whiskers, minimum and maximum.

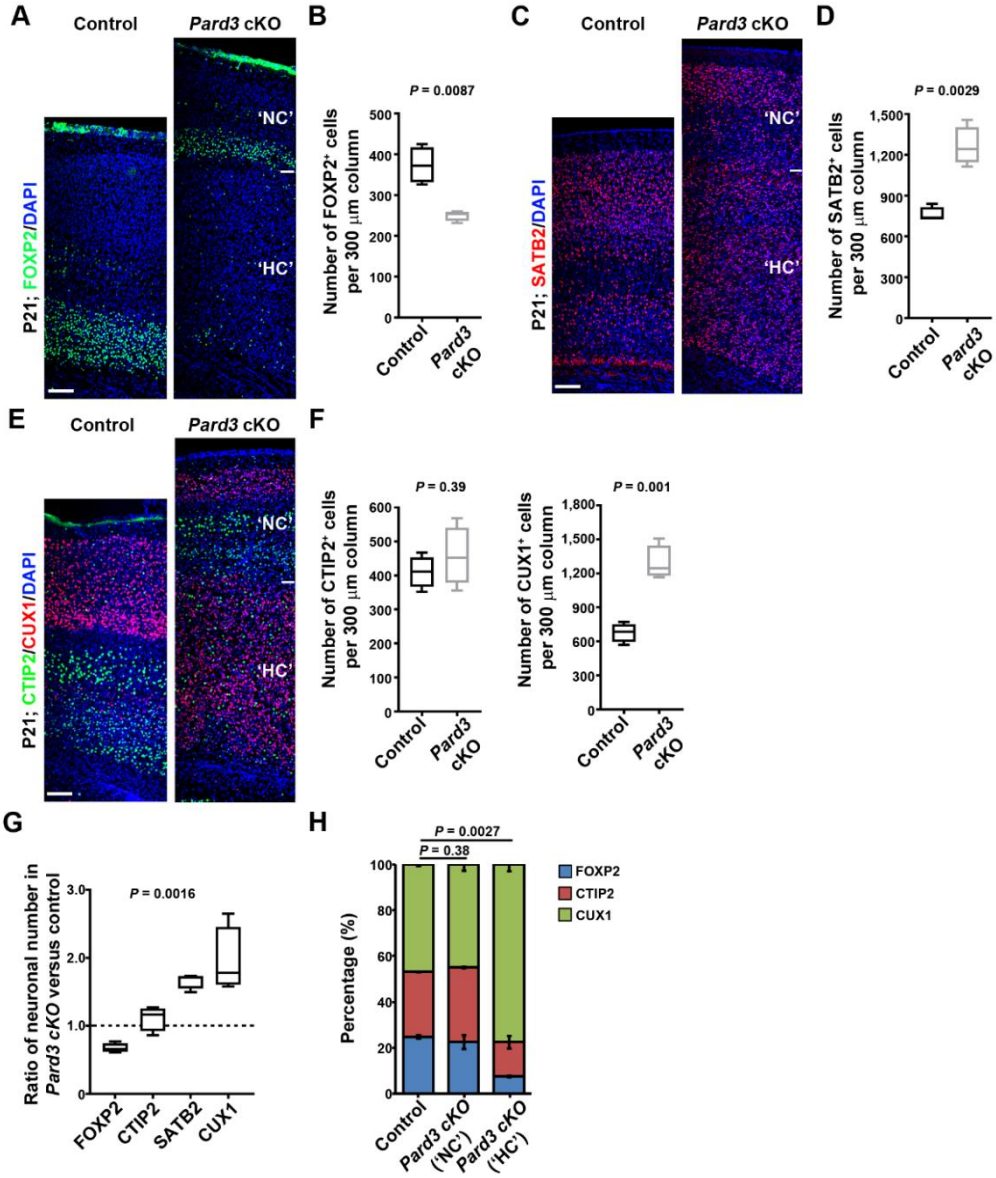
A
Control
Pard3 cKO
P21; FOXP2/DAPI
'NC'
'HC'
B
P = 0.0087
Number of FOXP2+ cells per 300 μm column
Control
Pard3 cKO
C
Control
Pard3 cKO
P21; SATB2/DAPI
'NC'
'HC'
D
P = 0.0029
Number of SATB2+ cells per 300 μm column
Control
Pard3 cKO
E
Control
Pard3 cKO
P21; CTIP2/CUX1/DAPI
'NC'
'HC'
F
P = 0.39
Number of CTIP2+ cells per 300 μm column
Control
Pard3 cKO
P = 0.001
Number of CUX1+ cells per 300 μm column
Control
Pard3 cKO
G
P = 0.0016
Ratio of neuronal number in Pard3 cKO versus control
FOXP2
CTIP2
SATB2
CUX1
H
P = 0.0027
P = 0.38
Percentage (%)
FOXP2
CTIP2
CUX1
Control
Pard3 cKO ('NC')
Pard3 cKO ('HC')

(Figure 2.8A, B and Figure 2.9A, B). In contrast, we observed a substantial increase in the density and total number of SATB2^{+} neurons in the *Pard3* cKO cortex compared with the control **(Figure 2.8C, D and Figure 2.9C, D)**. Together, these results suggest

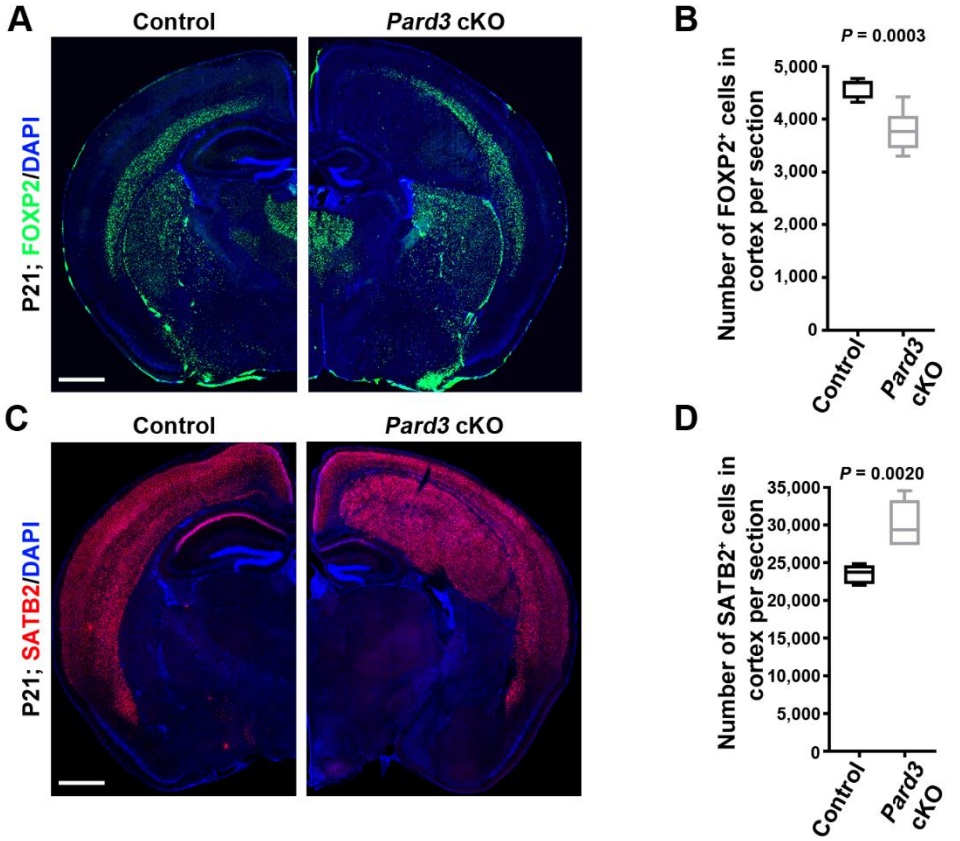

Figure 2.9: *Pard3* deletion leads to systematic alterations in the total number of excitatory neurons.

(A) Representative confocal images of P21 control and *Pard3* cKO coronal brain sections stained for layer VI neuronal marker FOXP2 (green) and counter-stained with DAPI (blue). Scale bar: 1 mm. **(B)** Quantification of the total number of FOXP2^{+} cortical neurons per section in control and *Pard3* cKO mice at P21 (n=8 per genotype; unpaired two-tailed t-test with Welch's correction). **(C)** Representative confocal images of P21 control and *Pard3* cKO coronal brain sections stained for layer II/III/V neuronal marker SATB2 (red) and counter-stained with DAPI (blue). Scale bars: 1 mm. **(D)** Quantification of the total number of SATB2^{+} cortical neurons per section to the NC. in control and *Pard3* cKO mice at P21 (n=6 per genotype; unpaired two-tailed t-test with Welch's correction).

that PARD3 removal in RGPs leads to a reduced production of deep layer neurons and a concomitant overproduction of superficial layer neurons.

To further characterize neuronal changes, we stained sections with antibodies against CTIP2 (green), a layer V/VI neuronal marker, and CUX1 (red), a layer II/III/IV neuronal marker (Greig et al. 2013) **(Figure 2.8E)**. Compared with the control, we observed similarly positioned but thinner layers of $CUX1^+$ and $CTIP2^+$ neurons in the NC of the *Pard3* cKO brain **(Figure 2.8E)**. On the other hand, neurons in the HC were predominantly $CUX1^+$ neurons with a few scattered $CTIP2^+$ neurons. Consequently, while the total density of $CTIP2^+$ neurons was comparable between the control and *Pard3* cKO cortices **(Figure 2.8F, left)**, the total density of $CUX1^+$ neurons in the *Pard3* cKO cortex was nearly double that of the control cortex **(Figure 2.8F, right)**. These results further demonstrate that PARD3 removal in RGPs leads to an excessive production of superficial layer neurons that predominantly occupy the HC in addition to the NC.

Interestingly, in comparison with the control, the changes in neuronal composition in the *Pard3* cKO cortex were systematic and progressive depending on laminar identity **(Figure 2.8G)**. While the deep layer VI $FOXP2^+$ neurons were significantly reduced, the superficial layers II-IV $CUX1^+$ as well as $SATB2^+$ neurons were concurrently and robustly increased. As a result, the total number of neurons in the cortex and the cortical volume were substantially increased. In addition, while the NC in the *Pard3* cKO brain contained a similar proportion of deep and superficial layer neurons to the control brain, the HC harbored predominantly superficial layer neurons **(Figure 2.8H)**. Coinciding with an overall increase in neuronal production, we also observed an increase in the number of glial cells in the *Pard3* cKO cortex **(Figure 2. 10A-C)**. Together, these results suggest that PARD3 removal in RGPs leads to a gradual but dramatic shift towards the production of late-born neurons at the expense of early-

born neurons, resulting in the formation of an enlarged cortex with two distinct parts: the NC with a relatively normal lamination but reduced in size, and the HC with no lamination and excessive superficial layer neurons.

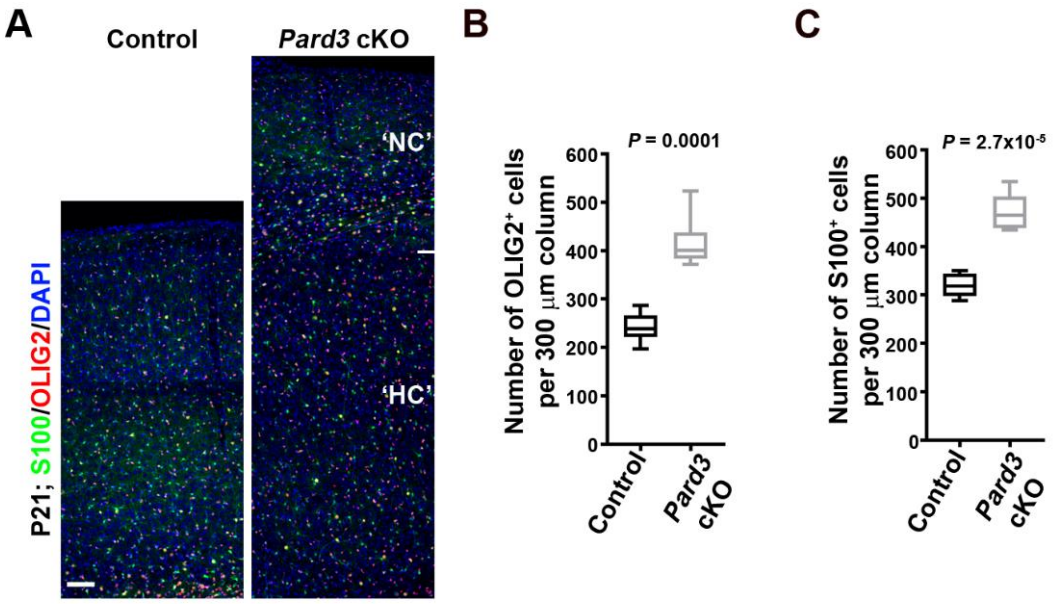

Figure 2.10: Pard3 deletion leads to the overproduction of glial cells.

(A) Representative confocal images of P21 control and *Pard3* cKO cortices stained for astrocyte marker S100 (green) and oligodendrocyte marker OLIG2 (red), and counter-stained for DAPI (blue). Scale bar: 70 μm. (B, C) Quantification of the number of $OLIG2^+$ (B) and $S100^+$ cells (C) per 300 μm radial column in P21 control and *Pard3* cKO mice (n=6 per genotype; unpaired two-tailed t-test with Welch's correction). For all box-whisker plots: center line, median; box, interquartile range; whiskers, minimum and maximum.

2.2.4 *Pard3* deletion causes abnormal RGP dynamics and organization

To understand the origins of altered neurogenesis and lamination in the *Pard3* cKO cortex, we next examined RGP behavior and organization at the embryonic stage. We systematically stained brain sections across the entire period of embryonic cortical development (i.e., E11.5-17.5) with an antibody against PAX6, a transcription factor highly expressed in cortical RGPs (Englund et al., 2005; Götz et al., 1998). While there

was no obvious change in the number or localization of PAX6$^+$ RGPs at E11.5, we observed a significant increase in the number of PAX6$^+$ RGPs in the VZ as well as outside of the VZ (i.e., extra-VZ, asterisks) at E12.5 in the *Pard3* cKO cortex compared with the control **(Figure 2.11A)**. Moreover, as development proceeded, RGPs in the *Pard3* cKO cortex exhibited distinct dynamic changes in the number and localization **(Figure 2.11A, B)**. While the density of RGPs in the control cortex remained largely comparable between E13.5-17.5, it exhibited a time-dependent biphasic change in the *Pard3* cKO cortex **(Figure 2.11B, left)**. It increased and peaked at E15.5, and then rapidly decreased after that. The changes in the VZ and extra-VZ appeared to be different **(Figure 2.11B, middle and right)**. Compared with the control, the density of RGPs in the VZ briefly increased at E12.5 and then gradually decreased after E13.5 **(Figure 2.11B, middle)**, whereas the density in the extra-VZ gradually increased till E15.5 and then decreased **(Figure 2.11B, right)**. Consistent with their RGP identity, PAX6$^+$ cells in both the VZ and extra-VZ expressed brain lipid-binding protein (BLBP) – a bona fide RGP marker (Hartfuss et al. 2001; Anthony et al. 2004) **(Figure 2.12)**, but not HOPX **(Figure 2.13A)**, PTPRZ1 **(Figure 2.13B)**, or TNC **(Figure 2.13C)** – previously suggested oRG markers (Pollen et al., 2015; Thomsen et al., 2016). While the VZ PAX6$^+$ cells possessed a typical bipolar morphology with a long radial glial fiber reaching the pia **(Figure 2.14A)**, the ectopic PAX6$^+$ cells in the extra-VZ possessed mostly a multi-polar morphology with several short processes but no obvious single long basal process **(Figure 2.14B-C)**, indicating that they are not typical oRGs previously characterized in the developing mouse cortex (Wang et al. 2011). Based on their expression of PAX6 and BLBP as well as their mitotic behavior (e.g., symmetric proliferation; see later Figures), we considered them RGPs or RG-like progenitors. Together, these results show that PARD3 removal leads to abnormal dynamic changes in RGP number and organization, but not oRG generation, in the embryonic cortex.

Figure 2.11: *Pard3* deletion causes abnormal RGP dynamics and organization in the embryonic cortex.

(A) Representative confocal images of control and *Pard3* cKO cortices stained for RGP marker PAX6 (green) and counter-stained with DAPI (blue) from E11.5 to E17.5. Double-headed arrows indicate the VZ and asterisks indicate ectopic RGPs or RG-like progenitors. Scale bars: 30 μm. **(B)** Quantification of the number of $PAX6^+$ cells per 200 μm radial column in the entire cortex (left), the VZ (middle), and outside the VZ (i.e., extra-VZ; right) in control (blue) and *Pard3* cKO (red) mice. E11.5: control, n=4; *Pard3* cKO, n=6; E12.5: control, n=6; *Pard3* cKO, n=4; E13.5: control, n=4; *Pard3* cKO, n=4; E14.5: control, n=6; *Pard3* cKO, n=5; E15.5: control, n=5; *Pard3* cKO, n=4; E16.5: control, n=4; *Pard3* cKO, n=10; E17.5: control, n=4; *Pard3* cKO, n=4. Data are presented as mean ± SEM. Two-tailed Mann-Whitney test was used to assess statistical significance.

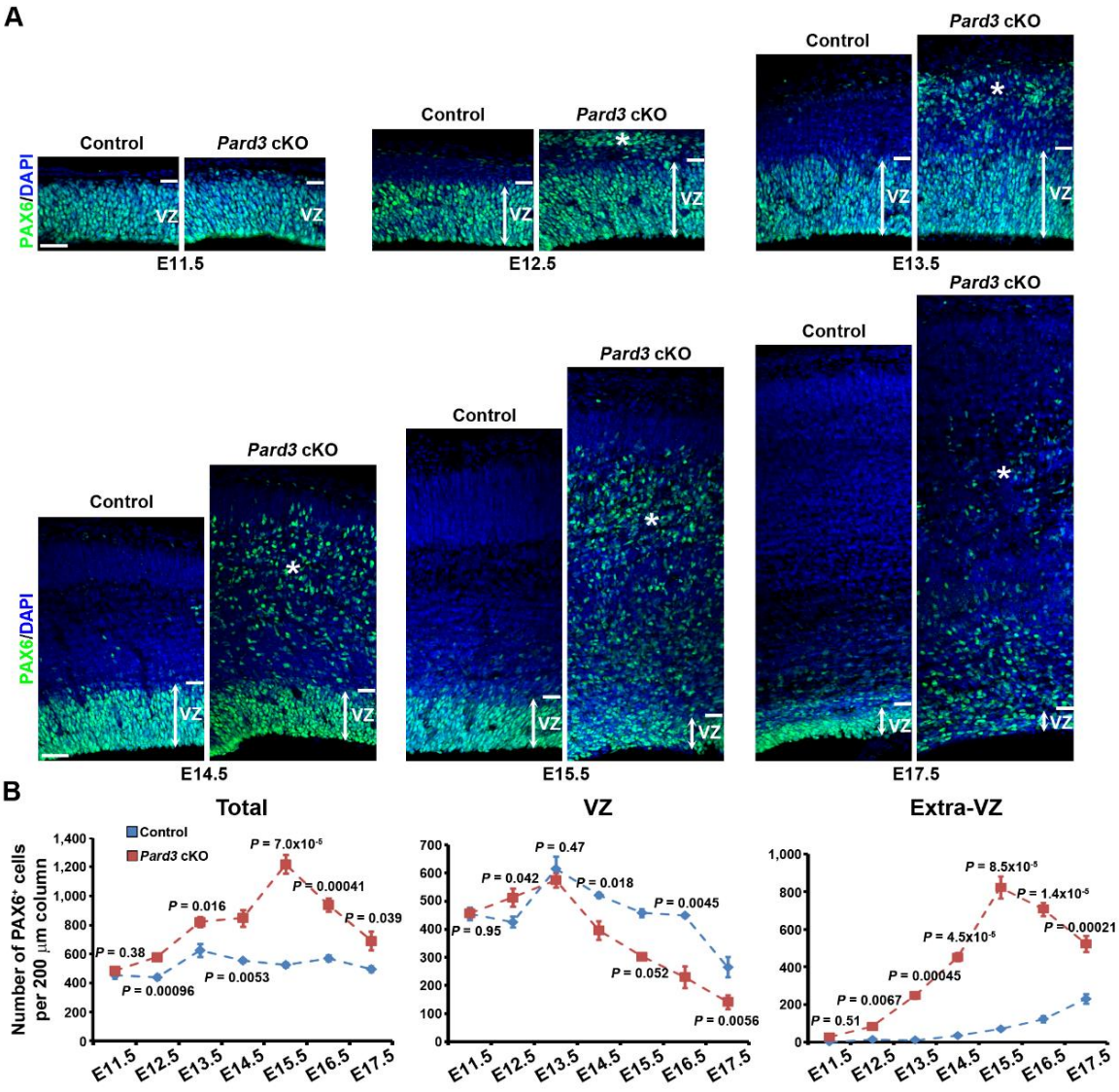
A
Control
Pard3 cKO
PAX6/DAPI
VZ
E11.5
E12.5
E13.5
E14.5
E15.5
E17.5
B
Total
VZ
Extra-VZ
Control
Pard3 cKO
Number of PAX6+ cells per 200 μm column
P = 0.38
P = 0.00096
P = 0.016
P = 0.0053
P = 7.0x10-5
P = 0.00041
P = 0.039
P = 0.95
P = 0.042
P = 0.47
P = 0.018
P = 0.0045
P = 0.052
P = 0.0056
P = 0.51
P = 0.0067
P = 0.00045
P = 4.5x10-5
P = 8.5x10-5
P = 1.4x10-5
P = 0.00021
E11.5
E12.5
E13.5
E14.5
E15.5
E16.5
E17.5

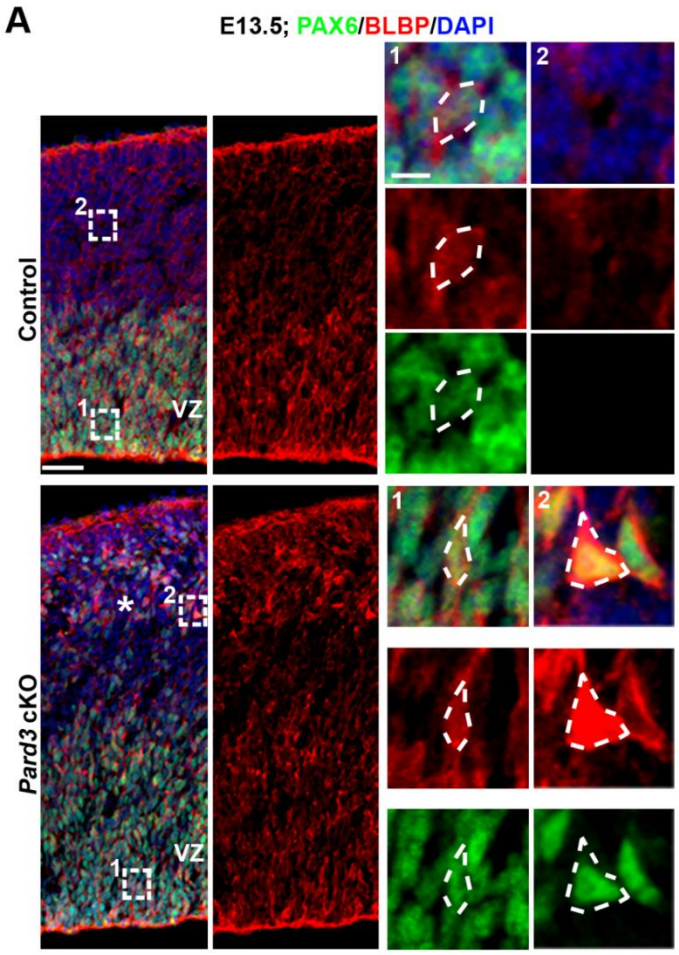

Figure 2.12: Ectopic PAX6^{+} RGPs express BLBP.

(A) Representative confocal images of E13.5 control and *Pard3* cKO cortices stained for PAX6 (green) and a bona-fide RGP marker BLBP (red), and counter-stained for DAPI (blue). High-magnification images of the VZ (areas 1) and extra-VZ (areas 2) are shown to the right. Broken line polygons indicate the cell bodies of representative progenitors in each group. Scale bars: 30 μm (left) and 10 μm (right).

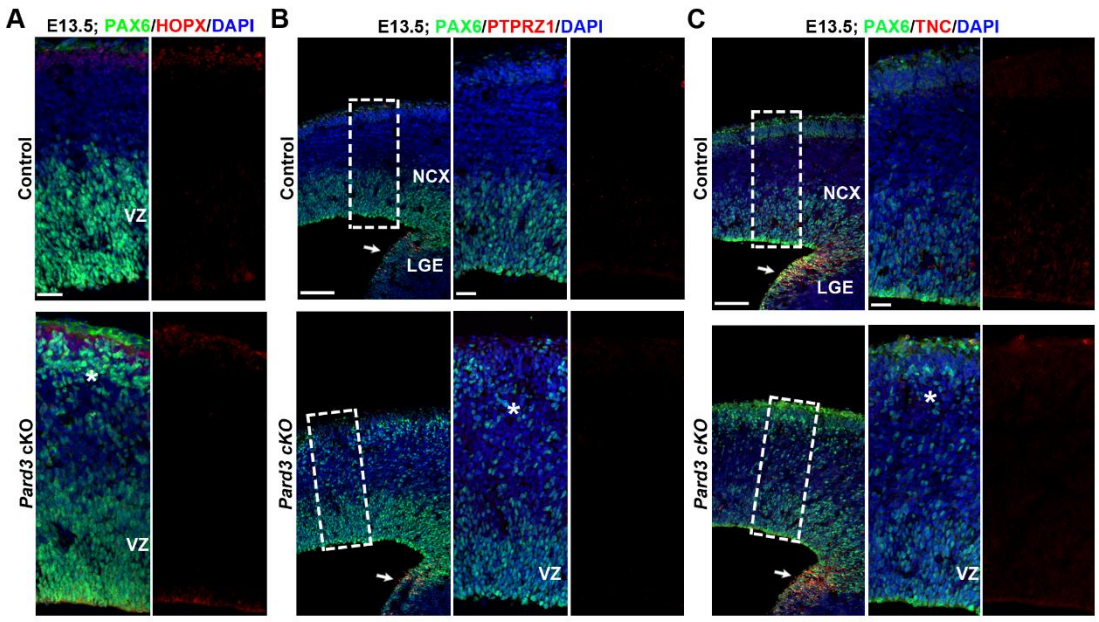

Figure 2.13: Ectopic RGPs in *Pard3* cKO cortex do not express oRG markers.

(A) Representative confocal images of E13.5 control and *Pard3* cKO cortices stained for PAX6 (green) and oRG marker HOPX (red), and counter-stained for DAPI (blue). Asterisk indicates ectopic $PAX6^+$ progenitors in *Pard3* cKO cortex. Scale bars: 30 □m. **(B)** Representative images of E13.5 control and *Pard3* cKO cortices stained for PAX6 (green) and oRG marker PTPRZ1 (red), and counter-stained for DAPI (blue). High magnification images of the cortex (broken line rectangles) are shown to the right. Arrows indicate PTPRZ1 signal in the LGE. Asterisk indicates ectopic $PAX6^+$ progenitors in *Pard3* cKO cortex. Scale bars: 100 μm (left) and 30 μm (right). **(C)** Representative images of E13.5 control and *Pard3* cKO cortices stained for PAX6 (green) and oRG marker TNC (red), and counter-stained for DAPI (blue). High magnification images of the cortex (broken line rectangles) are shown to the right. Arrows indicate TNC signal in the LGE. Asterisk indicates ectopic $PAX6^+$ progenitors in *Pard3* cKO cortex. Scale bars: 100 μm (left) and 30 μm (right).

Figure 2.14: Morphological analysis of RGPs in *Pard3* cKO cortex.

(A) Representative confocal images of the *Pard3* cKO cortex received *in utero* intraventricular injection of low-titer EGFP-expressing retrovirus at E13.5, stained for PAX6 (red) and EGFP (green), and counter-stained with DAPI (blue) at E14.5. Filled arrowheads show the long radial glial fiber of a $PAX6^+$ RGP in the VZ reaching the pia surface. High-magnification images of an EGFP-expressing, $PAX6^-$ differentiating progeny closely associated with the radial glial fiber (broken line square) are shown to the right. Scale bars: 30 μm (left) and 10 μm (right). **(B)** Representative confocal images of E14.5 control and *Pard3* cKO cortices stained for PAX6 (red) and pVIMENTIN (green), and counter-stained for DAPI (blue). High-magnification images of dividing RGPs in the VZ (areas 1) and extra-VZ (area 2) are shown to the right. Broken line polygons indicate the cell bodies of representative dividing RGPs in each group. RGP fibers are highlighted by arrowheads. Asterisk indicates ectopic $PAX6^+$ progenitors in *Pard3* cKO cortex. Scale bars: 30 μm (left) and 10 μm (right). **(C)** Representative confocal images of the *Pard3* cKO cortex received *in utero* intraventricular injection of EGFP-expressing retrovirus at E12.5, stained for PAX6 (red) and EGFP (green), and counter-stained for DAPI (blue) at E14.5. High-magnification images of EGFP-expressing $PAX6^+$ RGPs in extra-VZ (broken line rectangle) are shown to the right. Broken line polygons indicate the cell bodies of the representative RGPs. Note that the ectopic $PAX6^+$ cells grow multiple short processes. Scale bars: 30 μm (left) and 10 μm (right).

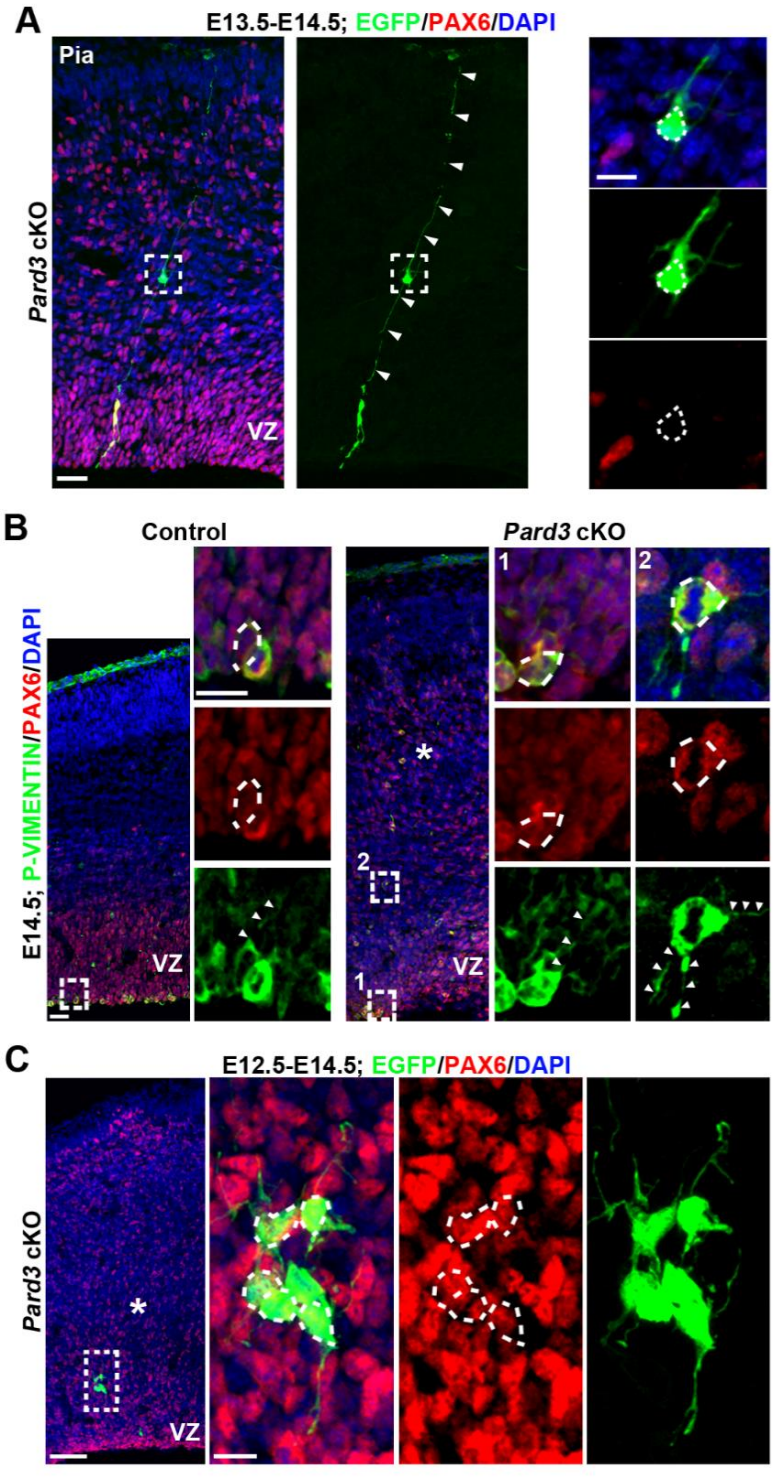
A
E13.5-E14.5; EGFP/PAX6/DAPI
Pia
Pard3 cKO
VZ
B
Control
Pard3 cKO
E14.5; P-VIMENTIN/PAX6/DAPI
VZ
1
2
C
E12.5-E14.5; EGFP/PAX6/DAPI
Pard3 cKO
VZ

Consistent with the giant SBH formation, PARD3 removal also disrupted neuronal migration in the developing cortex **(Figure 2.15)**.

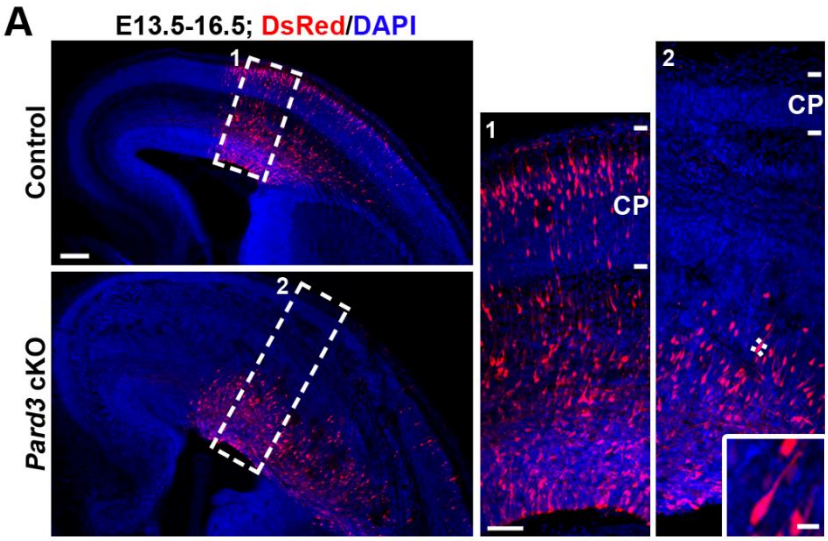

Figure 2.15: PARD3 removal disrupts neuronal migration in the developing cortex.

(A) Representative confocal images of the control and *Pard3* cKO cortices received *in utero* intraventricular electroporation of DsRed-expressing plasmid at E13.5, stained for PAX6 (red) and EGFP (green), and counter-stained with DAPI (blue) at E16.5. High-magnification images (broken line areas 1 and 2) are shown to the right. Image of representative cells with a bipolar morphology in the SVZ/IZ is shown as the inset.
Note that, while a significant fraction of DsRed-expressing cells migrates to the cortical plate in the control cortex, very few DsRed-expressing cells are found in the cortical plate of the *Pard3* cKO cortex (control, 31.0±2.4%; *Pard3* cKO, 1.9±1.1%; n=3 per genotype; $p<0.0001$; unpaired two-tailed t-test with Welch's correction; mean ± SEM). Scale bars: 150 μm (left) and 30 μm (middle) and 10 μm (right).

The changes in RGP number and localization in the *Pard3* cKO cortex occurred at E12.5 and E13.5, prior to any obvious defect in the junction and apical domain organization at the VZ surface **(Figure 2.2)**, suggesting that the original defects in the *Pard3* cKO cortex arise from abnormal behavior of RGPs, but not junction or VZ disorganization. Consistent with this, we observed a significant increase in the number of dividing cells at the VZ surface in the *Pard3* cKO cortex at E11.5 **(Figure 2.16A, B)**. Notably, this increase in mitosis appeared before any significant change in the overall

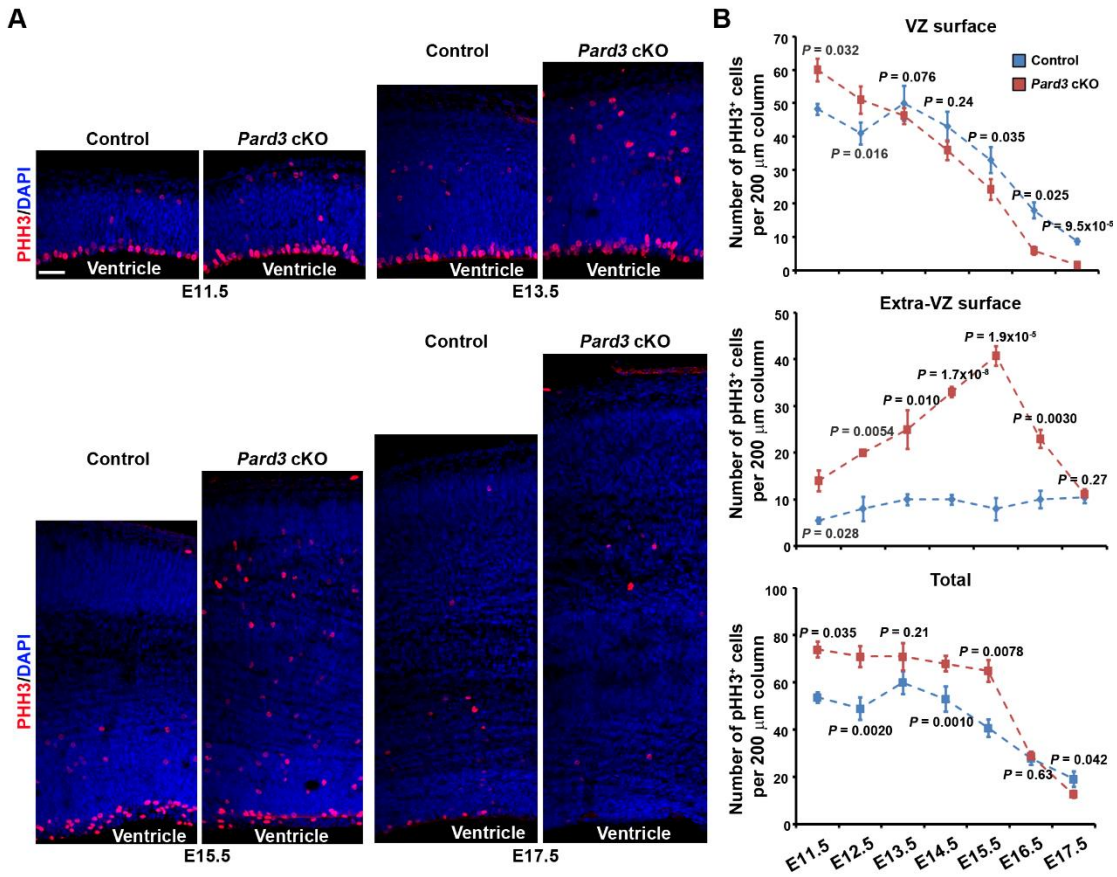

Figure 2.16: *Pard3* deletion leads to biphasic changes in the number and localization of the dividing cells.

(A) Representative confocal images of control and *Pard3* cKO cortices stained for mitotic cell marker pHH3 (red) and counter-stained for DAPI (blue) at E11.5 (top left), E13.5 (top right), E15.5 (bottom left) and e17.5 (bottom right). Scale bars: 30 μm. **(B)** Quantification of the number of $pHH3^+$ cells per 200 μm radial column at the VZ surface (top), extra-VZ surface (middle), or in the entire cortex (bottom) of the control (blue broken line) and *Pard3* cKO (red broken line) mice (two-tailed Mann-Whitney test). Data are presented as mean ± SEM. E11.5: control, n=4; *Pard3* cKO, n=6; E12.5: control, n=6; *Pard3* cKO, n=4; E13.5: control, n=4; *Pard3* cKO, n=4; E14.5: control, n=6; *Pard3* cKO, n=5; E15.5: control, n=5; *Pard3* cKO, n=4; E16.5: control, n=4; *Pard3* cKO, n=10; E17.5: control, n=4; *Pard3* cKO, n=4.

density of RGPs **(Figure 2.11)**. Together, these results suggest that PARD3 removal changes the mitotic behavior of RGPs. The increase in mitotic cells at the VZ surface persisted at E12.5 **(Figure 2.16B, top)**. Interestingly, we observed a robust and progressive increase in the number of mitotic cells away from the VZ surface between

E11.5 and E15.5 in the *Pard3* cKO cortex **(Figure 2.16B, middle)**. As a result, the total number of mitotic cells increased until E15.5 **(Figure 2.16B, bottom)**. Consistent with the biphasic changes in RGP number and localization, we also observed a rapid and significant decrease in the number of mitotic cells at the VZ surface as well as away from the VZ surface after E15.5 **(Figure 2.16B)**.

During cortical neurogenesis, RGPs divide at the VZ surface to produce neurons as well as IPs that continue to divide in the SVZ (Haubensak et al. 2004; Noctor et al. 2004; Englund et al. 2005). The increase in extra-VZ surface division in the *Pard3* cKO cortex may be attributable to IPs. To test this, we examined the production and organization of IPs **(Figure 2.17)**. We stained brain sections with an antibody against TBR2 (red), a T-box transcription factor highly expressed in IPs (Englund et al. 2005). As expected, $TBR2^+$ IPs were predominantly found in the SVZ of the control cortex **(Figure 2.17A, left)**. In contrast, $TBR2^+$ IPs were frequently observed in the SVZ as well as the intermediate zone (IZ) and cortical plate (CP) (asterisks) **(Figure 2.17A, right)**, where ectopic $PAX6^+$ RGPs were located, in the *Pard3* cKO cortex. Interestingly, the relative ratio of $TBR2^+$ IPs to $PAX6^+$ RGPs was significantly lower in the *Pard3* cKO cortex than in the control cortex across the embryonic stages **(Figure 2.17B)**, indicating an overall reduction in IP generation by RGPs lacking PARD3. Collectively, these results suggest that PARD3 removal drastically alters the mitotic behavior and organization of RGPs, leading to dynamic changes in the number and localization of RGPs, as well as IPs.

2.2.5 *Pard3* deletion promotes RGP symmetric proliferation at early neurogenic phase

To further dissect progenitor behavior that may be responsible for altered neurogenesis and enlarged cortex with massive heterotopia in the *Pard3* cKO brain, we

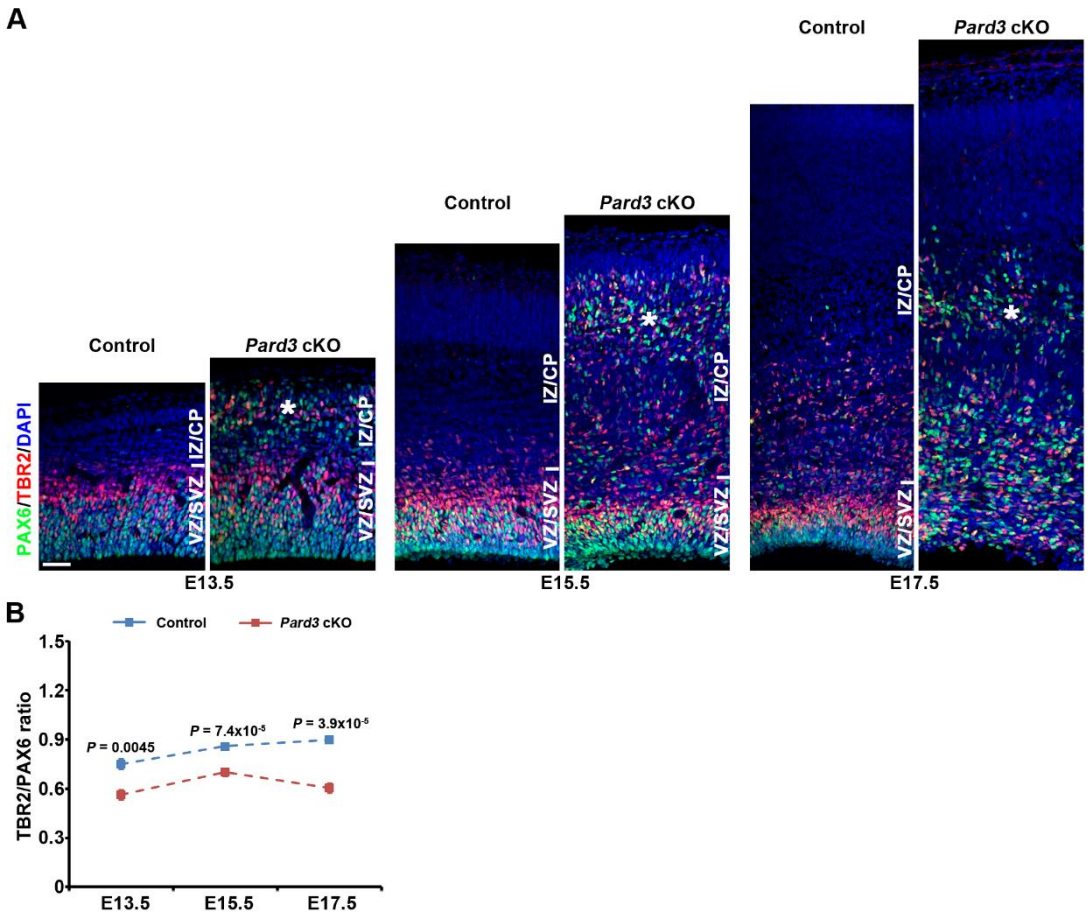

Figure 2.17: *Pard3* deletion causes a reduction in IP generation by RGPs.

(A) Representative confocal images of control and *Pard3* cKO cortices stained for PAX6 (green) and IP marker TBR2 (red), and counter-stained for DAPI (blue) at E13.5 (left), E15.5 (middle), and E17.5 (right). Asterisks indicate ectopic RGPs and IPs in the IZ and CP. Scale bar: 30 μm. **(B)** The TBR2/PAX6 ratio in control (broken blue line) and *Pard3* cKO (broken red line) mice at E13.5, E15.5 and E17.5 (n=4 per genotype; two-tailed Mann-Whitney test). Data are presented as mean ± SEM.

examined the cell cycle exit index of cortical progenitors prior to E15.5, when a progressive increase in RGPs was observed **(Figure 2.11)**. A single pulse of EdU was administered at E13.5 and brains were extracted at E14.5 and stained for the proliferative marker Ki67 **(Figure 2.18A)**. We analyzed the fraction of EdU^+ cells that were $Ki67^-$ (i.e., exited the cell cycle) and found that there was a significant reduction

Figure 2.18: Pard3 deletion promotes RGP symmetric proliferation at early neurogenic phase.

(A) Representative confocal images of E14.5 control and *Pard3* cKO cortices stained for proliferating marker Ki67 (green) and EdU (red), and counter-stained with DAPI (blue). Schematic protocol of the cell cycle exit assay is shown at the top. High-magnification images (broken lines) are shown at the bottom. Arrows indicate $Ki67^{+}/EdU^{+}$ progenitors and arrowheads indicate $Ki67^{-}/EdU^{+}$ post-mitotic cells. Scale bars: 30 μm (top) and 5 μm (bottom). **(B)** Quantification of the cell cycle exit index in control and *Pard3* cKO cortices at E14.5 (n=3 per genotype; unpaired two-tailed t-test with Welch's correction). Box-whisker plot: center line, median; box, interquartile range; whiskers, minimum and maximum. **(C)** Representative images of EGFP-expressing retrovirus-labeled two-cell clones stained with EGFP (green), PAX6 (red), and Ki67 (grey) in E14.5 control and *Pard3* cKO cortices. Schematic protocol of in vivo RGP division pattern assay is shown at the top. High-magnification images of representative clones (broken line rectangles) are shown to the right. Broken line polygons indicate the cell bodies of EGFP-expressing cells. Note that the clone in the control cortex is composed of one bipolar $PAX6^{+}/Ki67^{+}$ RGP and one multi-polar $PAX6^{-}/Ki67^{-}$ neuron, whereas the clone in the *Pard3* cKO cortex is composed of two $PAX6^{+}/Ki67^{+}$ RGPs with a multi-polar morphology. Scale bars: 30 μm (left), 15 μm (middle), and 5 μm (right). **(D)** Representative 3D reconstruction images of a cortical hemisphere with all EGFP-labeled clones in control (top) and *Pard3* cKO (bottom) embryos. Colored lines represent the pial surface and the lateral ventricle; Green filled circles represent RGPs, yellow filled circles represent IPs, and red filled circles represent Ns. **(E)** Percentage of EGFP-labeled RGP-IP/N (green), IP-IP or N-N (red), and RGP-RGP (blue) clones in control (n=4) or *Pard3* cKO (n=4) embryos at E14.5 (Chi-square test).

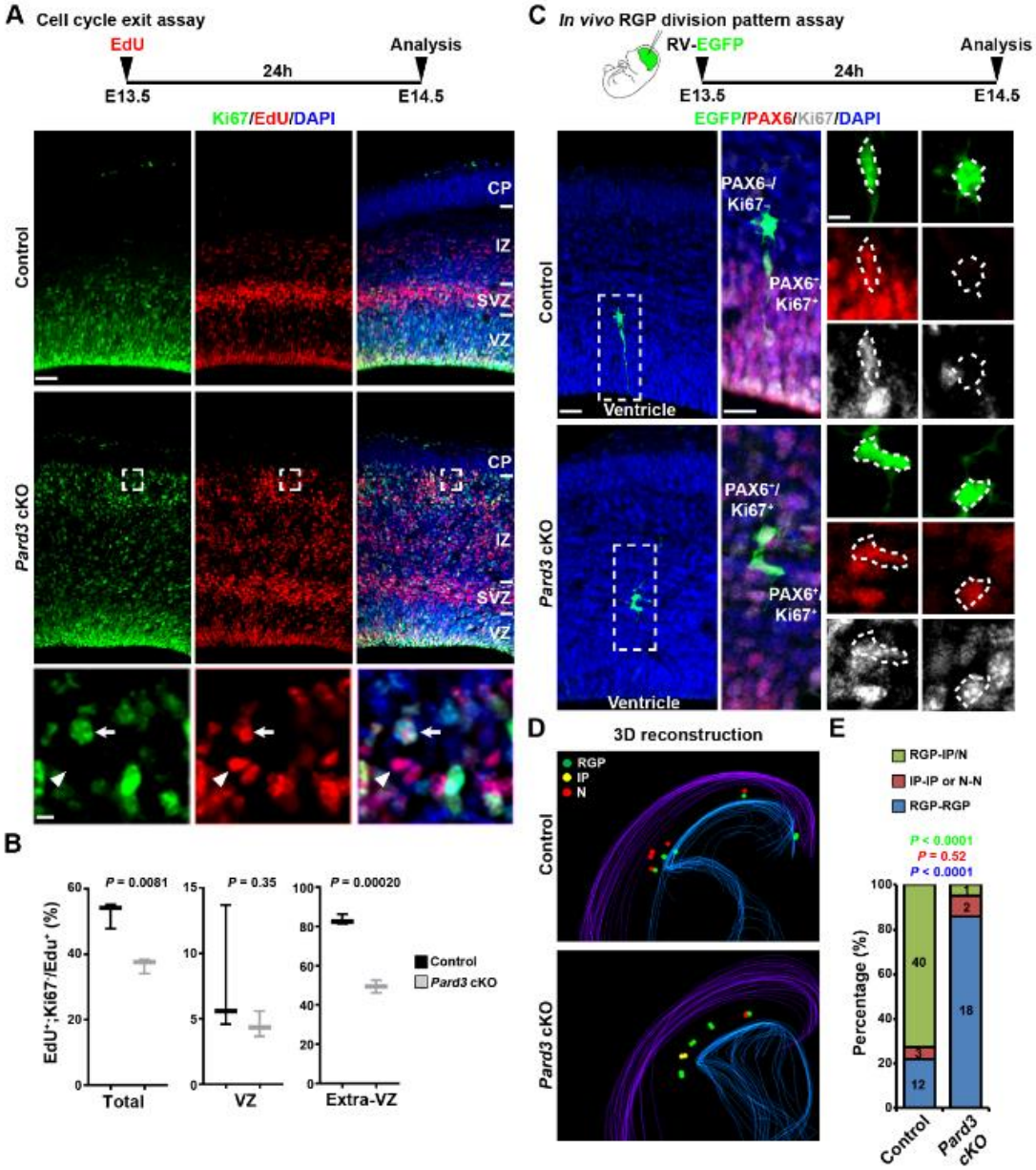
A
Cell cycle exit assay
EdU
24h
Analysis
E13.5
E14.5
Ki67/EdU/DAPI
Control
Pard3 cKO
CP
IZ
SVZ
VZ
B
P = 0.0081
P = 0.35
P = 0.00020
EdU+;Ki67+/Edu+ (%)
Total
VZ
Extra-VZ
Control
Pard3 cKO
C
In vivo RGP division pattern assay
RV-EGFP
EGFP/PAX6/Ki67/DAPI
PAX6-/Ki67-
PAX6+/Ki67+
Ventricle
D
3D reconstruction
RGP
IP
N
E
RGP-IP/N
IP-IP or N-N
RGP-RGP
P < 0.0001
P = 0.52
P < 0.0001
Percentage (%)
40
2
12
18

in cell cycle exit in the *Pard3* cKO cortex, compared with the control **(Figure 2.18B)**.

The reduced rate of cell cycle exit is consistent with an overproduction of RGPs **(Figure 2.11)** and also suggests a change in the division mode of RGPs. To test this, we performed *in vivo* clonal analysis to directly examine the division mode of RGPs **(Figure 2.18C)**. We injected serially diluted, low-titer retroviruses expressing enhanced green fluorescent protein (EGFP) into the lateral ventricle at E13.5 and recovered the brains at E14.5 for analysis. To assess the division mode of labeled RGPs, brains were serially sectioned and stained with antibodies against PAX6 and Ki67. We identified all sparsely labeled cell pairs in the cortex that originated from individual dividing RGPs by three-dimensional (3D) reconstruction **(Figure 2.18C, D)**. In these experiments, $PAX6^+/Ki67^+$, $PAX6^-/Ki67^+$, and $PAX6^-/Ki67^-$ cells corresponded to RGPs, IPs, and neurons (Ns), respectively. As expected, the majority of cell pairs in the control cortex contained a bipolar RGP and a multi-polar IP or N **(Figure 2.18C top, 2.18D top, 2.18E)**, indicating asymmetric neurogenic division. In contrast, the vast majority of cell pairs in the *Pard3* cKO cortex contained two RGPs **(Figure 2.18C bottom, 2.18D bottom, 2.18E)**, indicating symmetric proliferative division. Notably, the RGP pairs observed in the *Pard3* cKO cortex often exhibited a multi-polar morphology and were located outside the VZ **(Figure 2.18C bottom and Figure 2.14C)**. Together, these results suggest that PARD3 removal leads to a switch in RGP division mode from asymmetric neurogenic division to symmetric proliferative division. This division mode switch would account for the progressive overproduction of RGPs at the early phase of cortical neurogenesis and the concomitant loss of early-born deep layer neurons.

2.2.6 *Pard3* deletion promotes RGP differentiation and accelerates neurogenesis at late neurogenic phase

While the production of early-born neurons was reduced due to abnormal symmetric proliferation of RGPs, the cortical volume was increased with excessive late-born neurons in the *Pard3* cKO brain. These results indicate an accelerated neurogenesis at the late embryonic stage. To test this, we examined the embryonic production of $SATB2^+$ neurons **(Figure 2.19)**. At E15.5, the density of $SATB2^+$ neurons in the *Pard3* cKO cortex was significantly lower than that in the control cortex **(Figure 2.19A, left and 5B)**. In sharp contrast, at E17.5, the density of $SATB2^+$ neurons in the *Pard3* cKO cortex was substantially higher than that in the control cortex **(Figure 2.19A, right and 5B)**. This accelerated increase in $SATB2^+$ neurons between E15.5 and E17.5 in the *Pard3* cKO cortex occurred predominantly below the CP (the future HC), whereas the rate of increase in the CP (the future NC) was similar to that in the control cortex **(Figure 2.19C)**. An accelerated production of $CTIP2^+$ neurons was also observed in the *Pard3* cKO cortex **(Figure 2.20)**. Together, these results suggest that PARD3 removal leads to an accelerated neurogenesis at the late neurogenic phase, predominantly producing superficial layer neurons that occupy the future HC.

To further understand the cellular basis of the accelerated neurogenesis, we examined the division mode of RGPs *in vivo* at the late neurogenic stage (i.e., after E15.5) by performing *in vivo* clonal analysis **(Figure 2.19D)**. In the control cortex, the vast majority of sparsely labeled cell pairs contained a RGP and an IP or neuron **(Figure 2.19D top, 2.19E top, 2.19F)**, indicative of asymmetric neurogenic division. In contrast, in the *Pard3* cKO cortex, a large fraction of sparsely labeled cell pairs contained two IPs or two neurons **(Figure 2.19D bottom, 2.19E bottom, 2.19F)**, indicative of symmetric differentiation/neurogenic division. Together, these results suggest that PARD3 removal results in a switch in RGP division mode from asymmetric neurogenic division to symmetric differentiation division at the late neurogenic phase. Notably, PARD3 removal also led to a randomization of the mitotic spindle orientation of

Figure 2.19: *Pard3* deletion promotes RGP symmetric differentiation and accelerates neurogenesis at late neurogenic phase.

(A) Representative confocal images of control and *Pard3* cKO cortices stained for layer II/III/V neuronal marker SATB2 (red) and counter-stained with DAPI (blue) at E15.5 (left) and E17.5 (right). Asterisks indicate $SATB2^+$ neurons located below the CP (i.e. the future 'HC'). Scale bar: 30 μm. **(B)** Quantification of the number of $SATB2^+$ cells per 200 um radial column of the control (n=3, blue) and *Pard3* cKO (n=4, red) embryos at E15.5 and E17.5 (unpaired two-tailed t-test with Welch's correction). Data are presented as mean ± SEM. **(C)** Quantification of the ratio of $SATB2^+$ cells at E17.5 versus E15.5 per 200 μm radial column in CP (left) and below CP (right, i.e. the future 'HC') of the control (n=3) and *Pard3* cKO (n=4) embryos (unpaired two-tailed t-test with Welch's correction). Box-whisker plot: center line, median; box, interquartile range; whiskers, minimum and maximum. **(D)** Representative confocal images of EGFP-expressing retrovirus-labeled two-cell clones stained with EGFP (green), PAX6 (red), and Ki67 (grey) in E16.5 control and *Pard3* cKO cortices. Schematic protocol of *in vivo* RGP division pattern assay is shown at the top. High-magnification images of representative clones (broken line rectangles) are shown to the right. Broken line polygons indicate the cell bodies of EGFP-expressing cells. Note that the clone in the control cortex is composed of one bipolar $PAX6^+/Ki67^+$ RGP and one multi-polar $PAX6^-/Ki67^-$ neuron, whereas the clone in the *Pard3* cKO cortex is composed of two $PAX6^-/Ki67^+$ IPs. Scale bars: 30 μm (left), 15 μm (middle in control and top in *Pard3* cKO), and 5 μm (right in control and bottom in *Pard3* cKO). **(E)** Representative 3D reconstruction images of a cortical hemisphere with all EGFP-labeled clones in control (top) and *Pard3* cKO (bottom) embryos. Colored lines represent the pial surface and the lateral ventricle; Green filled circles represent RGPs, yellow filled circles represent IPs, and red filled circles represent Ns. **(F)** Percentage of EGFP-labeled RGP-IP/N (green), IP-IP, or N-N (red), and RGP-RGP (blue) clones in control (n=4) or *Pard3* cKO (n=4) embryos at E16.5 (Chi-square test).

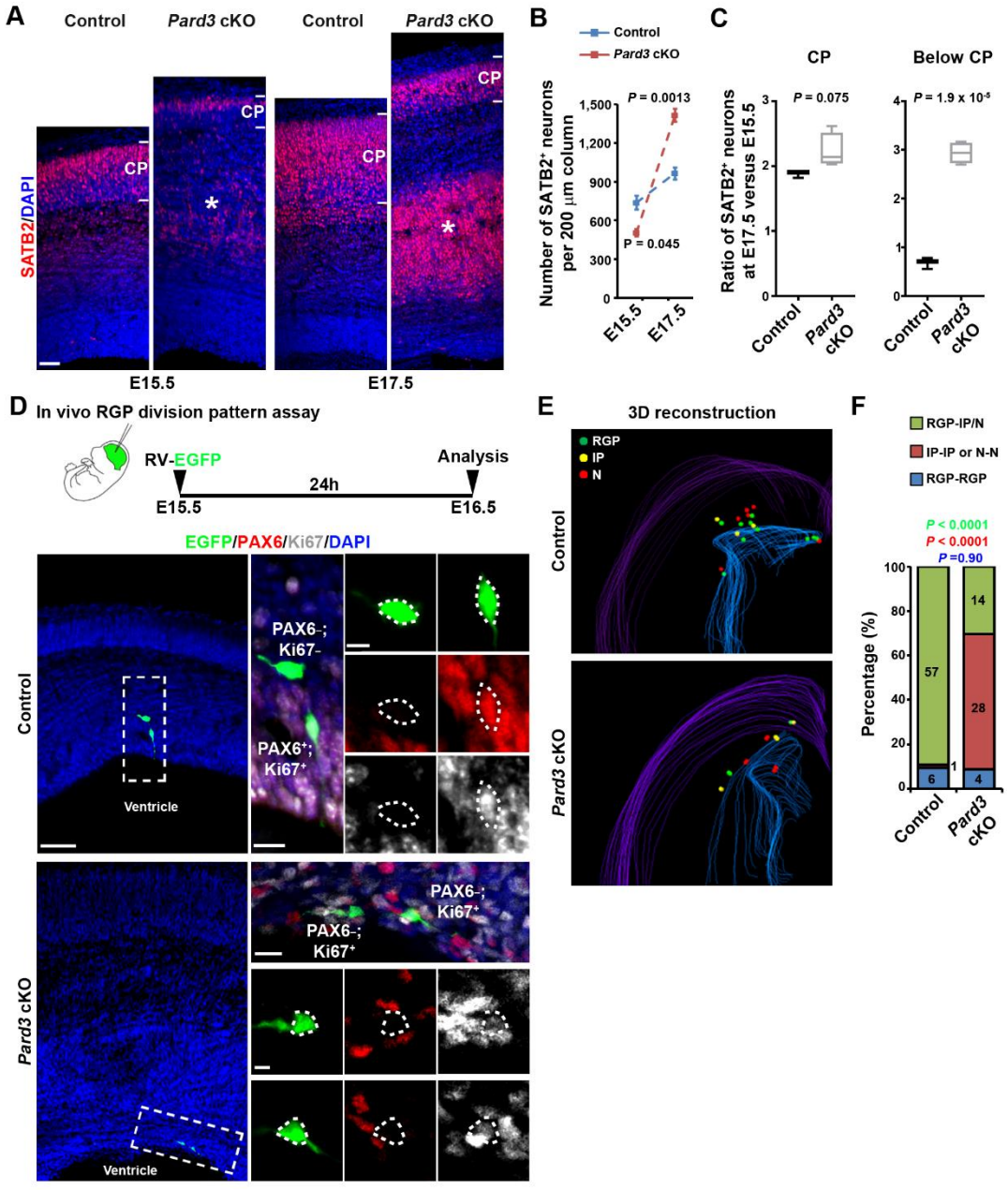
A
Control
Pard3 cKO
Control
Pard3 cKO
SATB2/DAPI
CP
CP
CP
CP
*
*
E15.5
E17.5
B
Control
Pard3 cKO
Number of SATB2+ neurons per 200 μm column
P = 0.0013
P = 0.045
1,500
1,200
900
600
300
0
E15.5
E17.5
C
CP
Below CP
Ratio of SATB2+ neurons at E17.5 versus E15.5
P = 0.075
P = 1.9 x 10-5
Control
Pard3 cKO
Control
Pard3 cKO
D
In vivo RGP division pattern assay
RV-EGFP
Analysis
24h
E15.5
E16.5
EGFP/PAX6/Ki67/DAPI
Control
Ventricle
PAX6-; Ki67-
PAX6+; Ki67+
Pard3 cKO
PAX6-; Ki67+
PAX6-; Ki67+
Ventricle
E
3D reconstruction
RGP
IP
N
Control
Pard3 cKO
F
RGP-IP/N
IP-IP or N-N
RGP-RGP
P < 0.0001
P < 0.0001
P =0.90
Percentage (%)
100
80
60
40
20
0
57
1
6
14
28
4
Control
Pard3 cKO

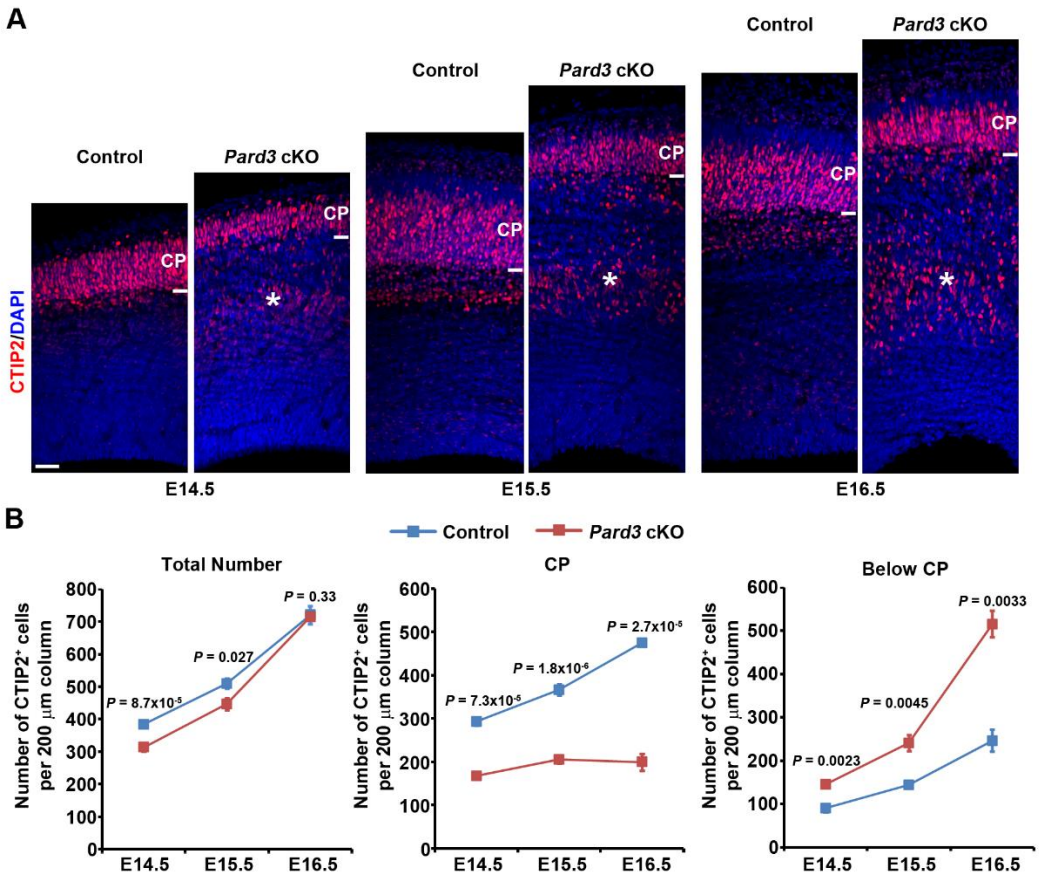

Figure 2.20: *Pard3* deletion suppresses production of CTIP2$^+$ neurons in the CP while accelerating generation of CTIP2$^+$ neurons located below the CP.

(A) Representative confocal images of control and *Pard3* cKO cortices stained for CTIP2 (red) and counter-stained for DAPI (blue) from E14.5 to E16.5 (from left to right). Asterisks indicate CTIP2$^+$ cells located below CP (i.e. the future 'HC') in *Pard3* cKO cortices. Scale bar: 30 μm. **(B)** Quantification of the number of CTIP2$^+$ cells per 200 μm radial column in the entire cortex (left), CP (middle), or below CP (right) of control (blue line) and *Pard3* cKO (red line) mice from E14.5 to E16.5. Data are presented as mean ± SEM. Two-tailed Mann-Whitney test was used to assess statistical significance. E14.5: control, n=4; *Pard3* cKO, n=5; E15.5: control, n=7; *Pard3* cKO, n=5; E16.5: control, n=3; *Pard3* cKO, n=3.

dividing RGPs at or away from the VZ surface **(Figure 2.21)**, indicating that PARD3 regulates the mitotic spindle orientation of RGPs. Given the initial overproduction of RGPs, this division mode switch would lead to an accelerated and excessive production of late-born neurons that largely contribute to the heterotopia and enlarged cortex.

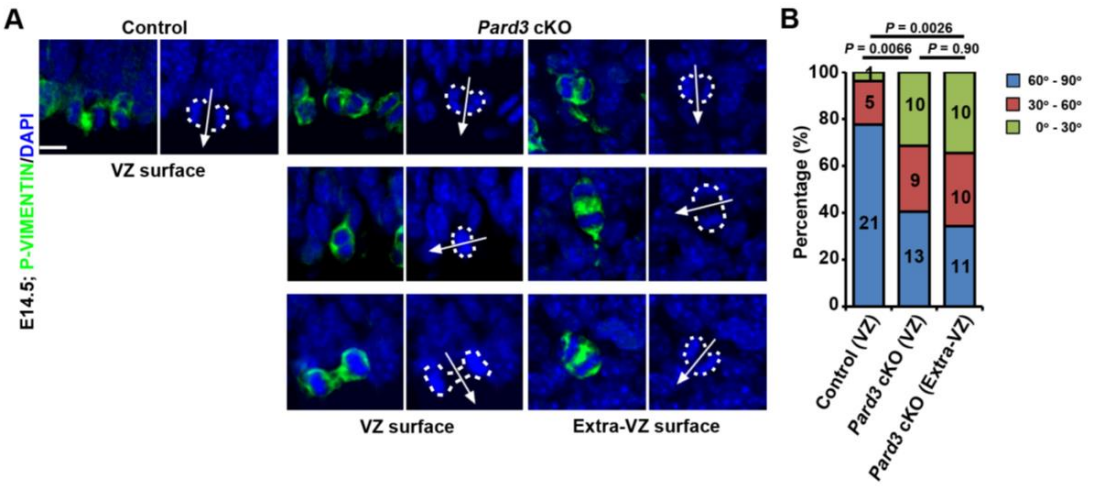

Figure 2.21: *Pard3* deletion randomizes the mitotic spindle orientation of dividing RGPs.

(A) Representative confocal images of mitotic RGPs stained for P-VIMENTIN (green) and counter-stained with DAPI (blue) at E14.5 in the control and *Pard3* cKO cortices. Broken lines indicate the contour of dividing RGPs and arrows indicate the cleavage plane. Scale bars: 5 μm. **(B)** Percentage of the dividing RGPs with 60º-90º (blue), 30º-60º (red), or 0º-30º (green) mitotic cleavage plane orientation, determined as the angle between the mitotic cleavage plane and the VZ surface, in the control (n=3) or *Pard3* cKO (n=3) cortices at E14.5 (Chi-square test). Note that the mitotic cleavage plane of dividing RGPs at or away from the VZ surface becomes randomized in the *Pard3* cKO cortex compared with the control.

2.2.7 Temporally distinct alterations in RGP division coincide with HIPPO signaling

Our results showed that PARD3 removal leads to temporally distinct changes in RGP mitotic behavior, raising the intriguing question on the underlying mechanism of the differences. Recent studies in cell cultures suggest that cell polarity proteins including PARD3 regulate the HIPPO pathway (Lv et al., 2015; Zhang et al., 2016), a conserved signaling pathway that controls cell proliferation and tissue development (Pan, 2010; Yu and Guan, 2013). To test whether HIPPO signaling is associated with abnormal behavior of RGPs in the *Pard3* cKO cortex, we stained cortical sections with an antibody against YAP, a major downstream effector of the HIPPO pathway (Pan

2010; Yu and Guan 2013) **(Fig. 2.22)**. Suppression of HIPPO signaling typically leads to elevated YAP expression and/or reduced YAP phosphorylation, and thereby promotes cell proliferation, whereas activation of HIPPO signaling usually results in decreased YAP expression and/or increased YAP phosphorylation, and facilitates cell differentiation (Pan, 2010; Yu and Guan, 2013).

Interestingly, compared with the control, the expression of YAP in RGPs, including in the nucleus, was increased **(Figure 2.22A, C)**, whereas the expression of phosphorylated YAP (pYAP) in RGPs was significantly decreased **(Figure 2.22B, D)**, in the *Pard3* cKO cortex at E13.5. These results suggest that PARD3 removal in RGPs leads to decreased HIPPO activity at the early neurogenic stage, which would promote excessive RGP proliferation. In contrast, compared with the control, YAP expression in RGPs was substantially reduced in the *Pard3* cKO cortex at the late neurogenic phase **(Figure 2.22E, F)**, consistent with accelerated differentiation/neurogenesis at this stage. Notably, no obvious change in the expression of YAP or pYAP in the blood vessels was observed **(Figure 2.22A, B, E open arrowheads)**. Together, these results suggest that PARD3 removal causes temporally distinct changes in HIPPO signaling in RGPs that coincide with the alterations in their mitotic behavior.

2.2.8 HIPPO signaling regulation depends on both *Pard3* deletion and NOTCH activity

Temporally distinct changes in YAP expression in *Pard3*-deficient RGPs indicate that additional factors are critical for HIPPO signaling regulation in response to PARD3 removal. To explore this, we examined the role of NOTCH signaling, a central signaling pathway in regulating RGP division and progeny output (Chenn and McConnell, 1995; Dong et al., 2012; Gaiano et al., 2000; Li et al., 2003; Petersen et al.,

Figure 2.22: *Pard3* deletion leads to temporally distinct alterations in the level of HIPPO signaling.

(A) Representative confocal images of E13.5 control and *Pard3* cKO cortices stained for PAX6 (green) and HIPPO pathway effector YAP (red), and counter-stained with DAPI (blue). High-magnification images (broken line rectangles) of RGPs in the VZ (arrows, areas 1) and extra-VZ (filled arrowheads; areas 2) are shown to the right. Open arrowheads indicate YAP expression in the blood vessel, which exhibits no obvious change between control and *Pard3* cKO cortices. High magnification images, including those of individual RGPs (broken lines), are shown to the right. Note the increased nuclear YAP signals in RGPs in the VZ and extra-VZ upon *Pard3* deletion. Scale bars: 30 μm (left), 15 μm (right, top), and 2.5μm (right, bottom). **(B)** Representative confocal images of E13.5 control and *Pard3* cKO cortices stained for PAX6 (green) and phospho-YAP (red), and counter-stained with DAPI (blue). Scale bars: 30 μm (top) and 15 μm (bottom). **(C)** Quantification of YAP staining signal intensity per RGP in the VZ and extra-VZ of the control and *Pard3* cKO cortices at E13.5 (n = 3 brains per genotype; unpaired two-tailed t-test with Welch's correction). A.U., arbitrary unit. **(D)** Quantification of phospho-YAP staining signal intensity per RGP in the VZ and extra-VZ of the control and *Pard3* cKO cortices at E13.5 (n = 3 brains per genotype; unpaired two-tailed t-test with Welch's correction). **(E)** Representative confocal images of E17.5 control and *Pard3* cKO cortices stained for PAX6 (green) and YAP (red), and counter-stained with DAPI (blue). Scale bars: 30 μm (left) and 15 μm (right). **(F)** Quantification of YAP staining signal intensity per RGP in the VZ and extra-VZ of the control and *Pard3* cKO cortices (n = 3 brains per genotype; unpaired two-tailed t-test with Welch's correction) at E17.5. For all box-whisker plots: center line, median; box, interquartile range; whiskers, minimum and maximum.

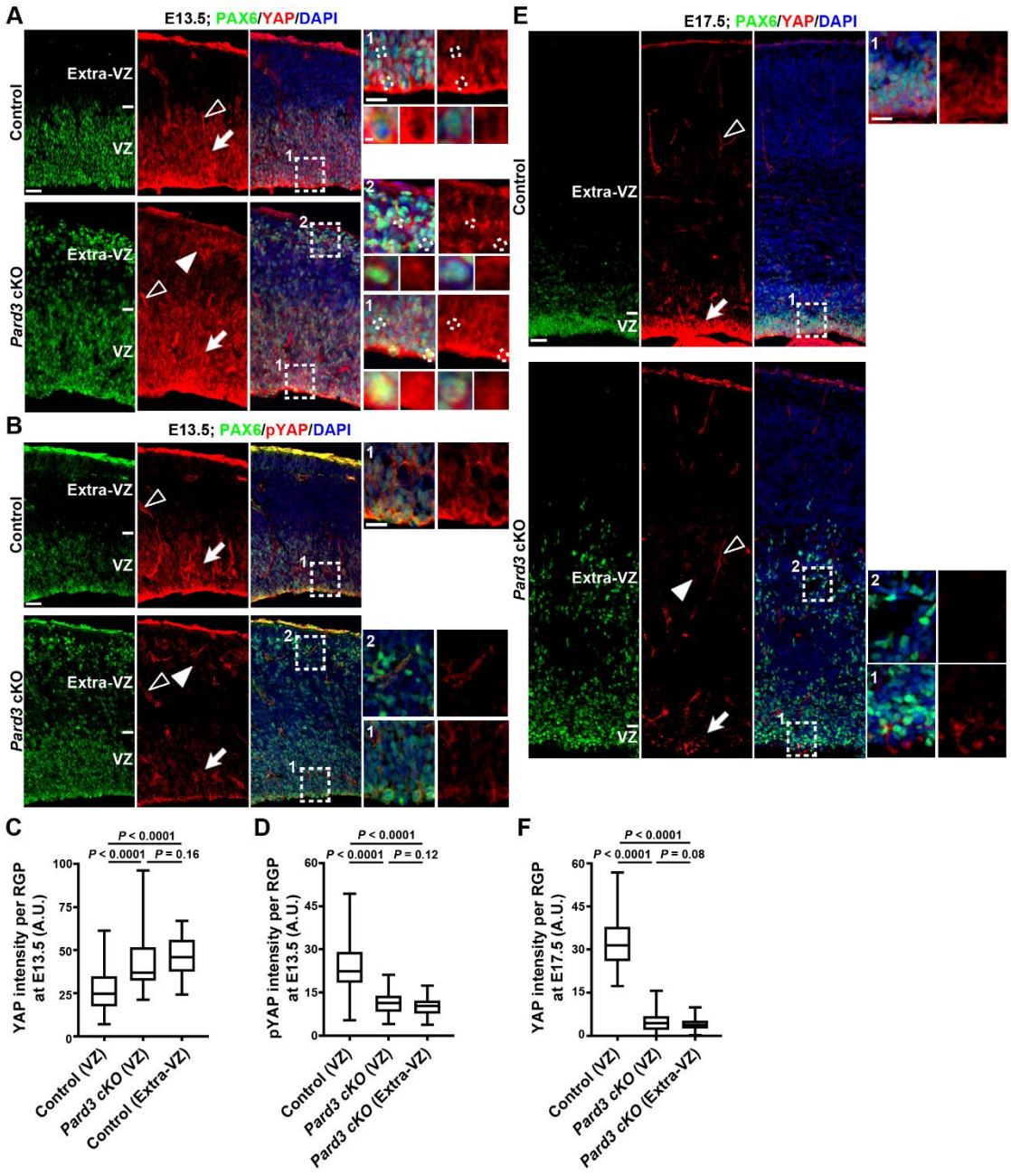
A
E13.5; PAX6/YAP/DAPI
Control
Pard3 cKO
Extra-VZ
VZ
B
E13.5; PAX6/pYAP/DAPI
E
E17.5; PAX6/YAP/DAPI
C
YAP intensity per RGP at E13.5 (A.U.)
P < 0.0001
P < 0.0001
P = 0.16
Control (VZ)
Pard3 cKO (VZ)
Control (Extra-VZ)
D
pYAP intensity per RGP at E13.5 (A.U.)
P < 0.0001
P < 0.0001
P = 0.12
Control (VZ)
Pard3 cKO (VZ)
Pard3 cKO (Extra-VZ)
F
YAP intensity per RGP at E17.5 (A.U.)
P < 0.0001
P < 0.0001
P = 0.08
Control (VZ)
Pard3 cKO (VZ)
Pard3 cKO (Extra-VZ)

2004). NOTCH signaling activity is thought to be high in RGPs to maintain their progenitor identity. To test whether NOTCH activity is related to temporally distinct changes in YAP expression and RGP mitotic behavior upon PARD3 removal, we first examined NOTCH activity in RGPs at different embryonic stages. To achieve this, we took advantage of a well-characterized NOTCH signaling activity reporter mouse line that contains the consensus NOTCH effector C-promoter binding factor 1 (CBF1; also called RBPJ) response element to direct the expression of a nuclear-localized Venus fluorescent protein (*CBF:H2B-Venus*) (Nowotschin et al., 2013). Using this reporter line, the endogenous NOTCH signaling activity can be inferred based on Venus expression. As expected, Venus expression was predominantly observed in the VZ, where RGPs reside **(Figure 2.23A)**. Moreover, the Venus intensity in RGPs progressively decreased as development proceeded **Figure 2.23B)**, indicative of a gradual decrease in NOTCH activity. Interestingly, the decrease in Venus expression was most prominent between E14.5 and E15.5, suggesting a sharp reduction in NOTCH signaling in RGPs at E15.5 under normal conditions. Notably, this drastic decrease in NOTCH activity temporally coincides with HIPPO signaling change as well as the alteration in RGP mitotic behavior in the *Pard3* cKO cortex. These results are consistent with the notion that NOTCH activity level influences HIPPO signaling and YAP expression and/or phosphorylation in RGPs in response to PARD3 removal.

To directly test this, we examined whether enhanced NOTCH signaling activity would promote YAP expression in RGPs lacking PARD3 at the late neurogenic stage. We took advantage of the conditional *Notch1* intracellular domain expression allele, *R26-LSL-NICD*, which allows Cre recombinase-dependent expression of NICD with constitutive signaling activity (Murtaugh et al., 2003). In addition, we used a tamoxifen (TM) inducible, cortical RGP-specific Cre mouse line, *Emx1-CreER* (Kessaris et al. 2006), to selectively remove *Pard3* as well as to drive NICD expression in a temporal-

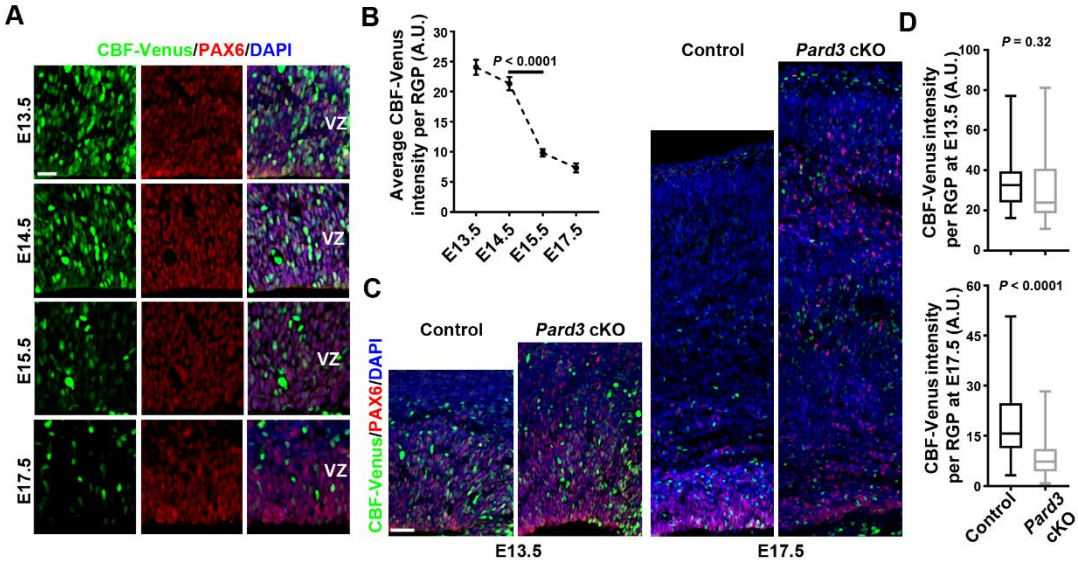

Figure 2.23: *Pard3* deletion does not disrupt Notch signaling at early neurogenic stage.

(A) Representative confocal images of the VZ of the control cortices stained for Venus (green) and PAX6 (red), and counter-stained for DAPI (blue) at E13.5, E14.5, E15.5, and E17.5 (from top to bottom). Scale bar: 20 μm. **(B)** Quantification of CBF-Venus intensity per RGP (n = 3 brains per genotype and per time point) at E13.5, E14.5, E15.5, and E17.5. Note the drastic decrease of CBF-Venus intensity between E14.5 and E15.5. **(C)** Representative images of control and *Pard3* cKO cortices stained for Venus (green) and PAX6 (red), and counter-stained for DAPI (blue) at E13.5 (left) and E17.5 (right). Scale bar: 30 μm. **(D)** Quantification of CBF-Venus intensity per RGP at E13.5 (top) and E17.5 (bottom) in control and *Pard3* cKO cortices (n = 3 brains per genotype, unpaired two-tailed t-test with Welch's correction).

specific manner. To ensure effective removal of PARD3 towards the late neurogenic phase, we treated timed pregnant single or double mutant mice with a single dose of TM at E13.5 and examined YAP expression in the cortex at E17.5 **(Figure 2.24)**. Consistent with our previous observation, YAP expression was reduced in *Pard3*-deleted RGPs compared with the control **(Figure 2.24A, top and 2.24B)**. Interestingly, while YAP expression in NICD-expressing RGPs did not obviously change, it was substantially increased in *Pard3*-deleted and NICD-expressing RGPs, especially in those located outside the VZ **(Figure 2.24A, bottom and 2.24B)**. Together, these results suggest that

Figure 2.24: PARD3 and NOTCH signaling work synergistically to regulate HIPPO signaling.

(A) Representative confocal images of E17.5 control (top left), *Emx1-CreER*;*Pard3*$^{fl/fl}$ (top right), *Emx1-CreER;R26-LSL-NICD* (bottom left) and *Emx1-CreER;Pard3*$^{fl/fl}$*;R26-LSL-NICD* (bottom right) cortices stained for PAX6 (green) and YAP (red), and counter-stained for DAPI (blue). Schematic protocol of tamoxifen induction is shown at the top. High-magnification images (broken line squares) of the RGPs in extra-VZ (filled arrowheads and insets) are shown to the right. Open arrowheads indicate YAP signal in the blood vessel. Broken line circles indicate the cell bodies of representative RGPs in extra-VZ and high magnification images are shown in the insets. Note that the VZ and ectopic PAX6^{+} cells in the *Emx1-CreER; Pard3*$^{fl/fl}$*; R26-LSL-NICD* cortex exhibit strong YAP staining signal. Scale bars: 50 μm (left), 15 μm (right) and 5μm (inset). **(B)** Quantification of YAP staining signal intensity per RGP in VZ (top) and Extra-VZ (bottom) at E17.5 (n = 3 brains per genotype; unpaired two-tailed t-test with Welch's correction). A.U., arbitrary unit. Box-whisker plot: center line, median; box, interquartile range; whiskers, minimum and maximum.

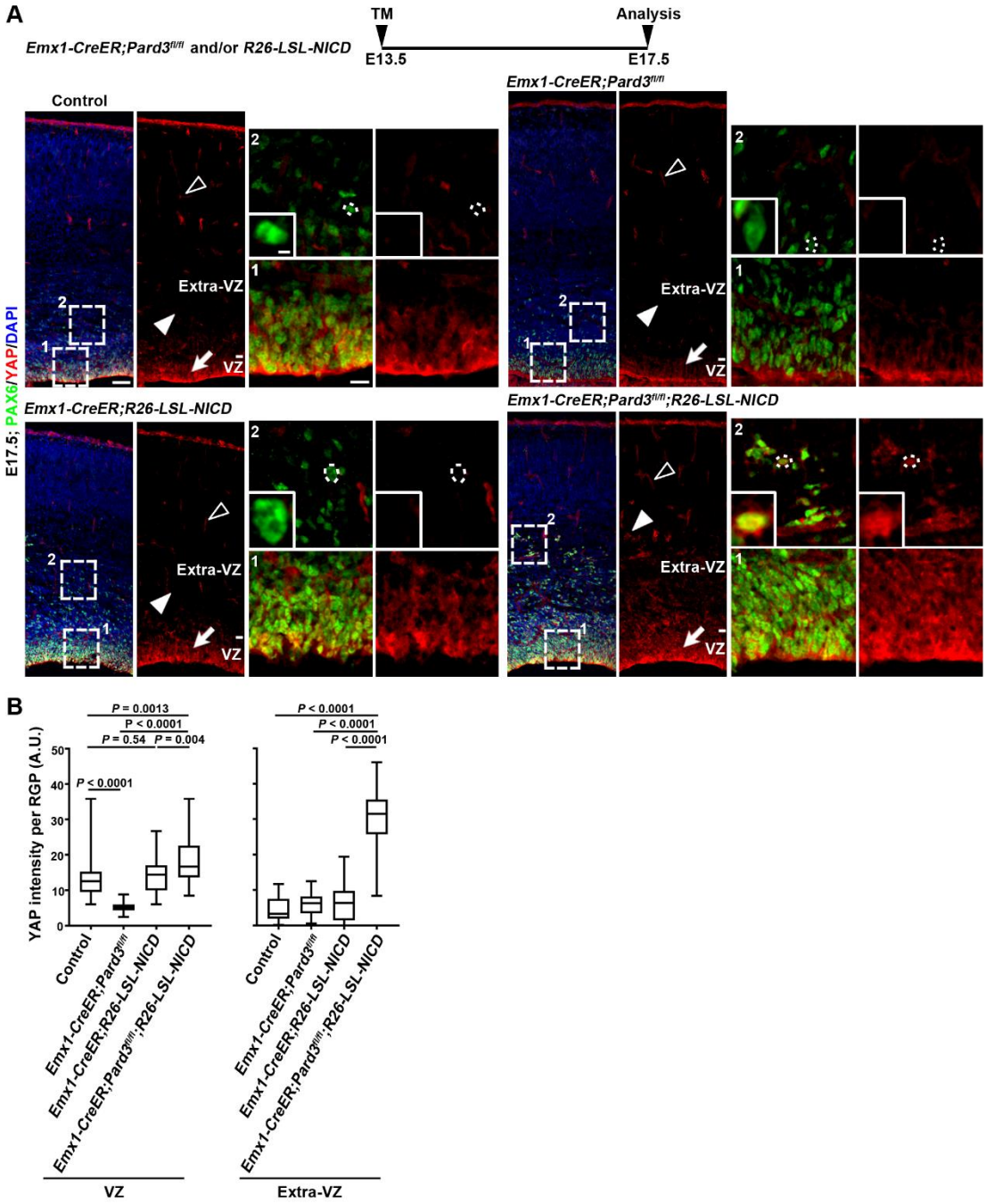
A
TM
Analysis
E13.5
E17.5
Emx1-CreER;Pard3fl/fl and/or R26-LSL-NICD
Control
Emx1-CreER;Pard3fl/fl
Emx1-CreER;R26-LSL-NICD
Emx1-CreER;Pard3fl/fl;R26-LSL-NICD
E17.5; PAX6/YAP/DAPI
Extra-VZ
VZ
1
2
B
YAP intensity per RGP (A.U.)
P = 0.0013
P < 0.0001
P = 0.54
P = 0.004
P < 0.0001
P < 0.0001
P < 0.0001
P < 0.0001
Control
Emx1-CreER;Pard3fl/fl
Emx1-CreER;R26-LSL-NICD
Emx1-CreER;Pard3fl/fl;R26-LSL-NICD
VZ
Extra-VZ

PARD3 removal in conjunction with high NOTCH activity promotes YAP expression in RGPs.

As expected on the basis of NOTCH and HIPPO signaling activities, while the number of PAX6^{+} RGPs was reduced in the *Pard3*-deleted cortex, it was increased in the NICD-expressing cortex, compared with the control **(Figure 2.25A, B)**. Importantly,

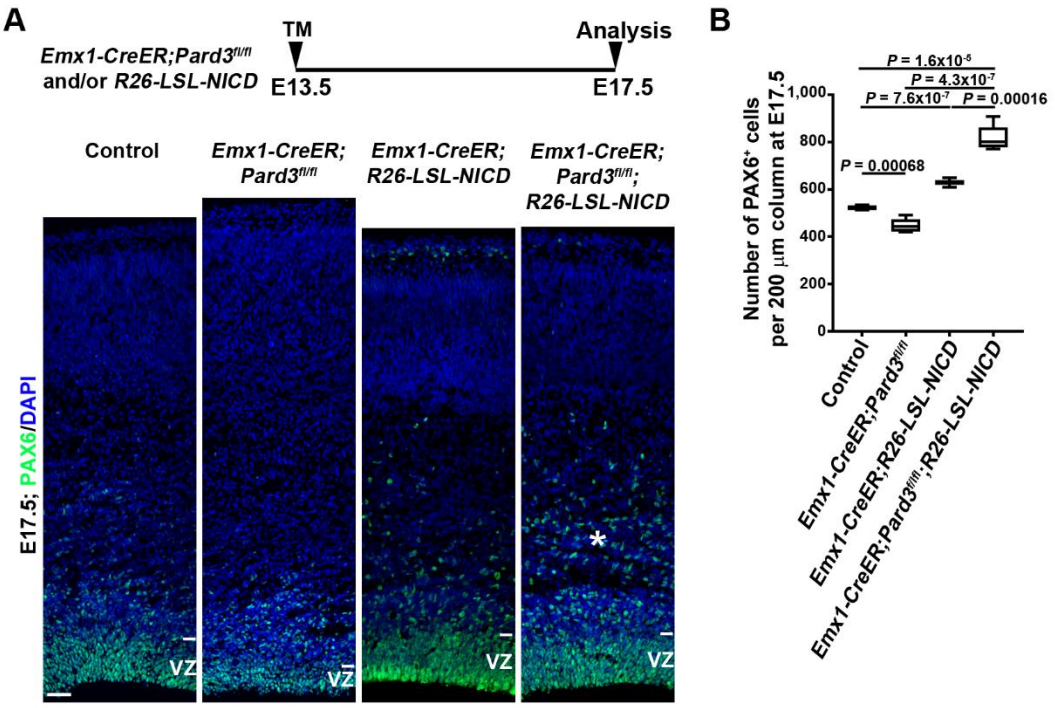

Figure 2.25: Functional interaction between PARD3 and NOTCH signaling.

(A) Representative confocal images of E17.5 control Emx1-CreER; *Pard3*$^{fl/fl}$, Emx1-CreER; R26-LSL-NICD, and Emx1-CreER; *Pard3*$^{fl/fl}$; R26-LSL-NICD (from left to right) cortices stained for PAX6 (green) and counter-stained for DAPI (blue). Asterisk indicates the ectopic PAX6^{+} cells in *Pard3* cKO cortex. Scale bar: 30 μm. **(B)** Quantification of the number of PAX6^{+} cells per 200 μm radial column in VZ (blue) and extra-VZ (red) of E17.5 cortices (n=6 per genotype; unpaired two-tailed t-test with Welch's correction).

the number of RGPs was further substantially increased in the *Pard3*-deleted and NICD-expressing cortex, especially outside the VZ **(Figure 2.25A, asterisk)**. Notably,

compared with the control, the NOTCH signaling activity did not exhibit any obvious change at the early neurogenic phase, but was significantly decreased at the late neurogenic phase in the *Pard3* cKO cortex **(Figure 2.23C, D)**, indicating that NOTCH signaling does not change prior to PARD3 removal. Together, these results suggest that PARD3, NOTCH activity, and HIPPO signaling act synergistically in regulating RGP mitotic behavior.

To further test this, we examined whether the initial excessive proliferation of RGPs and the reduction in HIPPO signaling upon PARD3 removal at the early neurogenic stage was dependent on NOTCH activity. To suppress NOTCH activity, we employed a conditional deletion allele of *Rbpj* (i.e., *Cbf1*) that encodes a transcriptional regulator essential for NOTCH signaling (Han et al. 2002). We generated cortex-specific single or double knockout of *Pard3* and *Rbpj* using *Emx1-Cre*. Notably, while we observed a drastic overproduction and ectopic localization of $PAX6^+$ RGPs in the *Pard3* cKO cortex, there was a strong reduction of $PAX6^+$ RGPs and a concomitant increase in $TUJ1^+$ post-mitotic neurons in the *Pard3* and *Rbpj* conditional double KO (*Pard3;Rbpj* cDKO) cortex, similar to that in the *Rbpj* cKO cortex **(Figure 2.26A-C)**. Moreover, YAP expression level was significantly decreased in the *Pard3;Rbpj* cDKO cortex compared with the control **(Figure 2.27A,B)**. Together, these results suggest that the excessive RGP proliferation and HIPPO signaling suppression at the early neurogenic phase caused by PARD3 removal depend on the relatively high NOTCH signaling.

2.2.9 Deletion of *Yap* and *Taz* fully suppresses giant heterotopia formation

To further determine the functional role of HIPPO signaling in driving defective RGP behavior and cortical malformation in the absence of PARD3, we took advantage of the conditional deletion alleles of *Yap* and *Taz* (Reginensi et al., 2013), and generated

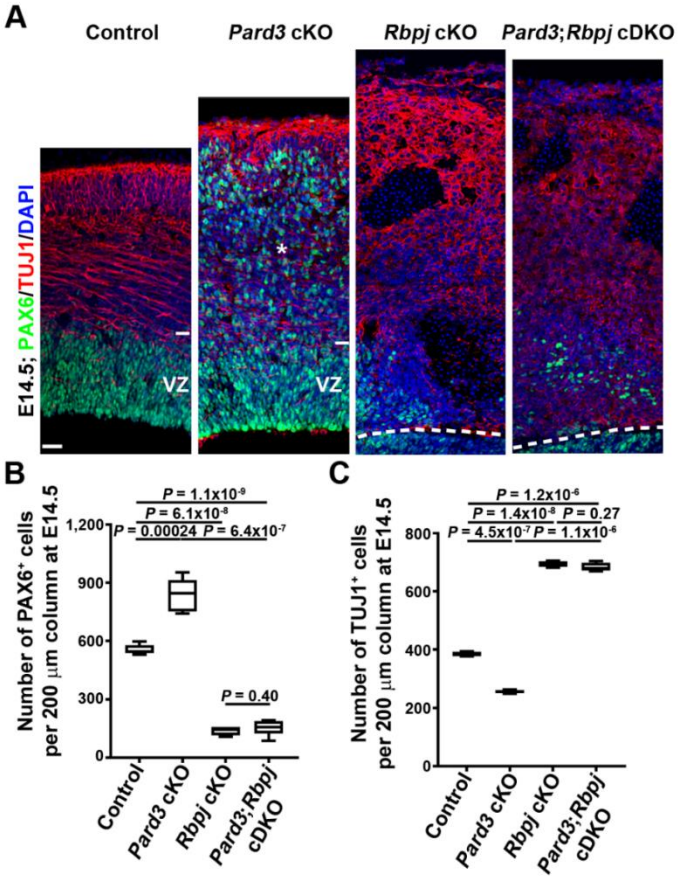

Figure 2.26: Neuronal differentiation in *Pard3; Rbpj* cDKO cortices.

(A) Representative confocal images of E14.5 control, *Pard3* cKO, *Rbpj* cKO, and *Pard3; Rbpj* cDKO (from left to right) cortices stained for PAX6 (green) and TUJ1 (red), and counter-stained for DAPI (blue). Asterisk indicates the ectopic $PAX6^+$ cells in *Pard3* cKO cortex. Broken lines indicate the VZ surface. Scale bar: 30 μm. **(B, C)** Quantification of the number of $PAX6^+$ (B) and $TUJ1^+$ (C) cells per 200 μm radial column of the cortex at E14.5 (n=4 per genotype; unpaired two-tailed t-test with Welch's correction). For all box-whisker plots: center line, median; box, interquartile range; whiskers, minimum and maximum.

cortical specific single, double, or triple knockout of *Pard3*, *Yap*, or *Taz* using *Emx1-Cre* **(Figure 2.28 and Figure 2.29)**. Notably, simultaneous deletion of *Yap* and *Taz* suppressed the drastic overproduction and ectopic localization of $PAX6^+$ RGPs in the *Pard3* cKO cortex at the embryonic stage **(Figure 2.28A, B)**. No obvious change in the density or localization of RGPs was observed in the *Yap* and *Taz* single or double cKO

Figure 2.27: YAP signal intensity in *Pard3; Rbpj* cDKO cortices.

(A) Representative confocal images of E14.5 control (top left), *Pard3* cKO (top right), *Rbpj* cKO (bottom left), and *Pard3*; *Rbpj* cDKO (bottom right) cortices stained for PAX6 (green) and YAP (red), and counter-stained with DAPI (blue). High-magnification images (broken line rectangles) of RGPs in VZ (filled arrows and insets) are shown to the right. Open arrowheads indicate YAP signal in the blood vessel. Broken line circles indicate the cell bodies of representative RGPs in VZ and high magnification images are shown in the insets. Scale bars: 30 μm (left), 15 μm (right), and 5 μm (inset). **(B)** Quantification of YAP staining signal intensity in VZ at E14.5 (n=3 per genotype; unpaired two-tailed t-test with Welch's correction). A.U., arbitrary unit. For all box-whisker plots: center line, median; box, interquartile range; whiskers, minimum and maximum.

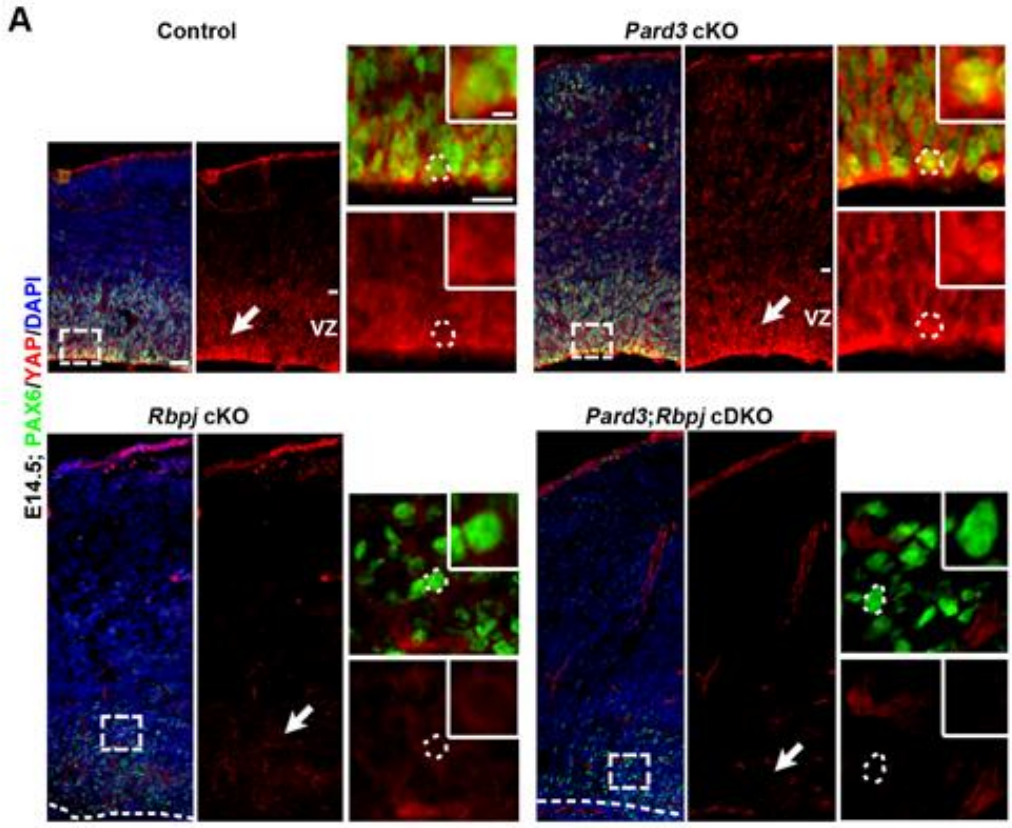
A
Control
Pard3 cKO
Rbpj cKO
Pard3;Rbpj cDKO
E14.5; PAX6/YAP/DAPI
VZ
VZ

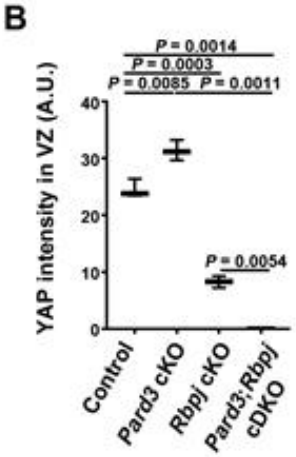
B
P = 0.0014
P = 0.0003
P = 0.0085
P = 0.0011
P = 0.0054
YAP intensity in VZ (A.U.)
40
30
20
10
0
Control
Pard3 cKO
Rbpj cKO
Pard3;Rbpj cDKO

cortex **(Figure 2.28A, B)**. These results strongly suggest that YAP and TAZ play an essential role in mediating abnormal behavior and organization of RGPs lacking PARD3. Strikingly, in contrast to the massive heterotopia formation in the *Pard3* cKO cortex, we observed no heterotopia formation in the *Pard3, Yap, and Taz* conditional triple knockout (*Pard3;Yap;Taz* cTKO) cortex at the postnatal stage **(Figure 2.28C)**. Compared with the control, the lamination was largely normal in the *Pard3;Yap;Taz* cTKO cortex. There was no increase in the density of superficial layer neurons; instead, we observed a relatively small but significant reduction in the densities of both superficial and deep layer neurons in the *Pard3;Yap;Taz* cTKO cortex, as well as in the *Yap;Taz* cDKO cortex **(Figure 2.28D, E)**. Consistent with a previously reported role of YAP in regulating the generation of ependymal cells that line the ventricle (Park et al. 2016), we observed a loss of ependymal cells **(Figure 2.29)** and severe hyhrocephalus **(Figure 2.28C, arrowheads)** in the *Yap;Taz* cDKO and *Pard3;Yap;Taz* cTKO brains, which may contribute to the small decrease in cortical size. Together, these results clearly suggest that cortical enlargement and massive heterotopia formation in the *Pard3* cKO cortex depend on YAP and TAZ, two essential transcriptional co-activators of the HIPPO pathway.

2.3 Discussion

Proper RGP organization and division are instrumental to orderly neurogenesis and cortical development; however, the molecular control of the orderly RGP behavior in the embryonic cortex remains poorly understood. In this study, we reveal for the first time the temporally distinct activities of PARD3 in concert with dynamic HIPPO and NOTCH signaling regulate RGP division and cortical formation. At the early neurogenic phase when NOTCH activity is relatively high, PARD3 removal suppresses HIPPO signaling and promotes RGP symmetric proliferation, leading to an excessive

Figure 2.28: *Yap* and *Taz* deletion suppresses ectopic RGP generation and heterotopia formation in *Pard3*-deficient cortex.

(A) Representative confocal images of E14.5 control, *Pard3* cKO, *Yap;Taz* cDKO, and *Pard3*;*Yap;Taz* cTKO cortices stained for PAX6 (green) and counter-stained for DAPI (blue). Asterisk indicates the ectopic $PAX6^+$ RGPs in *Pard3* cKO cortex. Scale bar: 30 μm. **(B)** Quantification of the number of $PAX6^+$ cells per 200 μm radial column in E14.5 control, *Pard3* cKO, *Yap;Taz* cDKO, and *Pard3*;*Yap;Taz* cTKO cortices (n=6 brains per genotype; unpaired two-tailed t-test with Welch's correction). **(C)** Representative nissl staining images of P12 control, *Pard3* cKO, *Yap;Taz* cDKO, and *Pard3*;*Yap;Taz* cTKO brain sections. Asterisks indicate the giant heterotopia. Arrows indicate the defective VZ surface and hydrocephalus. Scale bar: 2.5 mm. **(D)** Representative confocal images of P12 control, *Pard3* cKO, *Yap;Taz* cDKO, and *Pard3;Yap;Taz* cTKO cortices stained for layer V/VI neuronal marker CTIP2 (green) and layer II-IV neuronal marker CUX1 (red), and counter-stained for DAPI (blue). The 'NC' stands for the normotopic cortex and 'NC' stands for the heterotopic cortex. Scale bar: 70 μm. **(E)** Quantification of the number of $CTIP2^+$ (top) and $CUX1^+$ (bottom) cells per 300 μm radial column in control, *Pard3* cKO, *Yap;Taz* cDKO, and *Pard3;Yap;Taz* cTKO cortices at P12 (n=6 brains per genotype; unpaired two-tailed t-test with Welch's correction). For all box-whisker plots: center line, median; box, interquartile range; whiskers, minimum and maximum.

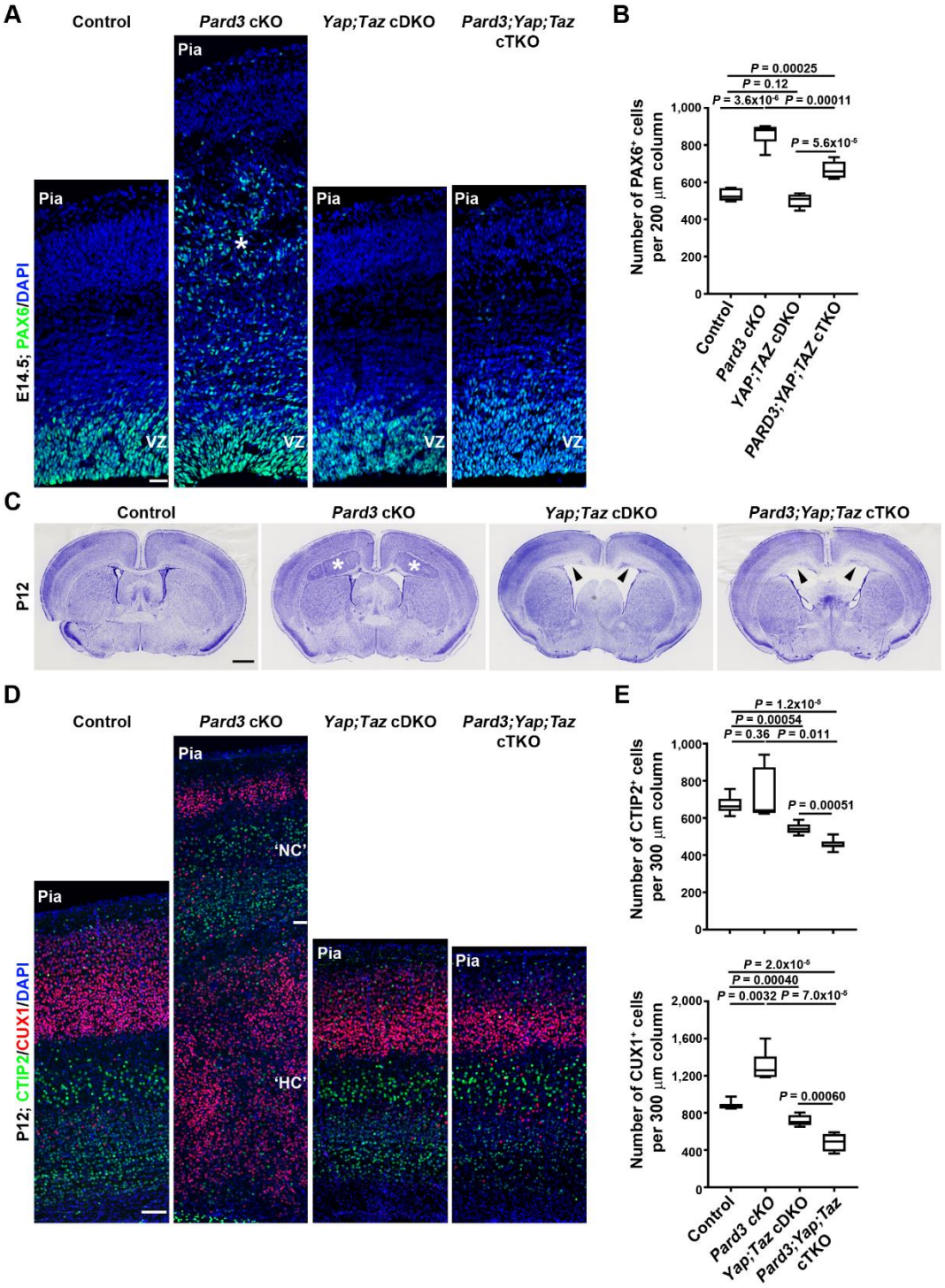
A
Control
Pard3 cKO
Yap;Taz cDKO
Pard3;Yap;Taz cTKO
Pia
VZ
E14.5; PAX6/DAPI
B
P = 0.00025
P = 0.12
P = 3.6x10-6
P = 0.00011
P = 5.6x10-5
Number of PAX6+ cells per 200 μm column
1,000
800
600
400
200
0
Control
Pard3 cKO
YAP;TAZ cDKO
PARD3;YAP;TAZ cTKO
C
Control
Pard3 cKO
Yap;Taz cDKO
Pard3;Yap;Taz cTKO
P12
D
Control
Pard3 cKO
Yap;Taz cDKO
Pard3;Yap;Taz cTKO
Pia
'NC'
'HC'
P12; CTIP2/CUX1/DAPI
E
P = 1.2x10-5
P = 0.00054
P = 0.36
P = 0.011
P = 0.00051
Number of CTIP2+ cells per 300 μm column
1,000
800
600
400
200
0
P = 2.0x10-5
P = 0.00040
P = 0.0032
P = 7.0x10-5
P = 0.00060
Number of CUX1+ cells per 300 μm column
2,000
1,600
1,200
800
400
0
Control
Pard3 cKO
Yap;Taz cDKO
Pard3;Yap;Taz cTKO

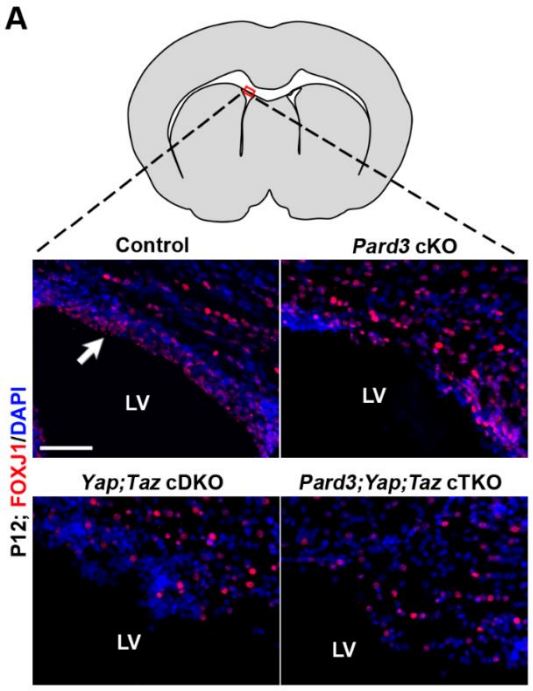

Figure 2.29: A loss of ependymal cells in the *Yap;Taz* cDKO and *Pard3;Yap;Taz* cTKO brains.

(A) Representative confocal images of P12 control, *Pard3* cKO, *Yap;Taz* cDKO, and *Pard3;Yap;Taz* cTKO cortices stained for FOXJ1 (red), an ependymal cell marker, and counter-stained with DAPI (blue). The schematic of the dorsal surface of the lateral ventricle where the images were taken is shown at the top. Arrows indicate $FOXJ1^+$ ependymal cells at the dorsal side of the lateral ventricle. LV, lateral ventricle. Scale bar: 70 μm.

production of RGPs or RG-like progenitors largely located outside the VZ at the expense of early-born deep layer neurons. In sharp contrast, at the late neurogenic phase when NOTCH activity is relatively low, PARD3 removal enhances HIPPO signaling, reduces NOTCH activity, and facilitates RGP symmetric differentiation, resulting in an accelerated and overproduction of late-born superficial layer neurons predominantly residing below the emerging cortex. As a result, the mutant cortex is significantly enlarged with massive SBH, and the mutant animal exhibits increased seizure susceptibility. Simultaneous removal of YAP and TAZ, two key transcriptional co-

activators of the HIPPO pathway, prevents RGP over-proliferation and delocalization in the absence of PARD3 and fully suppresses excessive neurogenesis and giant heterotopia formation. Together, our data define a key molecular and signaling program of PARD3, HIPPO signaling, and NOTCH activity that act in concert to ensure orderly RGP division behavior and neuronal production in the mammalian cortex.

Previous studies using short hairpin RNAs or morpholinos have implicated PARD3 in regulating neural progenitor cell division in vertebrates. However, its function appears to be contrary in different systems (i.e., zebrafish versus mice) with regard to promoting the generation of progenitors (proliferation) (Alexandre et al. 2010; Dong et al. 2012) or neurons (differentiation) (Costa et al. 2008; Bultje et al. 2009). Interestingly, we found that PARD3 removal can facilitate either proliferation or differentiation of RGPs depending on the developmental stage in conjunction with HIPPO and NOTCH signaling activities. Our finding that PARD3 removal promotes RGP proliferation at the early neurogenic stage (e.g., E13.5) is essentially opposite to the previous study showing that PARD3 knockdown causes RGP premature cell cycle exit and depletion (Costa et al. 2008). The temporally distinct function of PARD3 in regulating progenitor behavior has not been suggested in the previous studies, including those in C. elegans and Drosophila. Our data indicate that PARD3 acquires complex functions in supporting RGP division and orderly neurogenesis in the mammalian cortex.

A recently study in Madin-Darby Canine Kidney Epithelial (MDCK) epithelial or tumor cells suggested that PARD3 has a dual role in regulating HIPPO signaling, depending on the cellular context (Zhang et al., 2016). Our data suggest that NOTCH activity can be a key factor in determining the precise regulation of HIPPO signaling by PARD3. Previous genome-wide analysis has implicated YAP as a direct transcriptional target of NOTCH activity (Li et al., 2012). Notably, we found that elevated NOTCH activity alone (e.g., NICD expression) is ineffective in promoting YAP expression. On

the other hand, elevated NOTCH activity together with PARD3 removal strongly promotes YAP expression. These results suggest that cellular organization such as polarity and junction formation related to PARD3 expression is critical for HIPPO signaling regulation, consistent with their functional context in tissue development and homeostasis (Pan, 2010; Yu and Guan, 2013). PARD3 has also been recently shown to regulate the activation of TAZ (Lv et al. 2015), the other downstream transcription co-activator of the HIPPO pathway (Pan, 2010). As shown in our functional analysis, both YAP and TAZ play a critical role in PARD3-dependent regulation of RGP behavior and cortical neurogenesis.

The initial excessive proliferation of RGPs upon PARD3 removal occurs at E11-12, prior to any obvious defects in the organization of the VZ, including the integrity of the apical VZ surface. While PARD3 has previously been shown to be enriched at the VZ surface junction formed between the endfeet of neighboring RGPs (Bultje et al., 2009), our data suggest that PARD3 is not essential for the maintenance of existing junctions at the VZ surface. Moreover, our data suggest that a primary function of PARD3 is to regulate progenitor division mode and daughter cell fate specification in concert with NOTCH and HIPPO signaling activities. On the other hand, PARD3 is likely required for junction formation by newly specified RGPs. As a result, overproduced RGPs lacking PARD3 fail to form junctions at the VZ surface (i.e., be anchored to the apical junction belt of the VZ) and consequently become ectopically localized outside the VZ. As time proceeds, accumulating RGPs become ectopically located and the junction organization at the VZ surface is progressively disrupted.

Of note, even when junction defects were observed towards the late neurogenic stage, there was no drastic global disorganization of the VZ in the *Pard3* cKO cortex. This is clearly distinct from the *RhoA* or junction gene (e.g., *Cadherin2* or *α-E-Catenin*) mutant cortex (Cappello et al., 2006; Gil-Sanz et al., 2014; Schmid et al., 2014), despite

the fact that a similar SBH (but with no obvious cortical enlargement) is observed. Due to the severe disruption of the junction and VZ, dividing cells labeled by PHH3 in the embryonic *RhoA* or junction gene mutant cortex are broadly dispersed. It is unclear whether the division mode of RGPs in these mutant cortices exhibits any changes. In contrast, many dividing cells in the embryonic *Pard3* cKO cortex remain aligned at the VZ surface (e.g. E15.5), as expected for dividing VZ RGPs, in addition to those ectopically localized dividing cells. Therefore, our data reveal that the initial switch in RGP division mode producing excessive ectopically localized RGPs followed by an accelerated neurogenesis triggers the formation of massive SBH and an enlarged cortex. Consistent with this, we found that simultaneous deletion of *Yap* and *Taz* suppresses the excessive production and ectopic localization of RGPs due to *Pard3* deletion, and completely prevents the formation of heterotopia. Our data not only demonstrate that the over-proliferation of RGPs depends on HIPPO signaling, but also show that RGP over-proliferation is responsible for their delocalization away from the VZ and the subsequent heterotopia formation.

While the overall thickness of the NC in the *Pard3* cKO brain is greatly reduced, the relative proportion of individual neuronal layers appears to be largely comparable to the control cortex. On the other hand, the HC or hetertopia is predominantly composed of late-born superficial layer neurons. These results suggest that the progenitor origins of the NC and heterotopia are different. It is intriguing that a normally laminated cortex consisting of both superficial and deep layer neurons forms above the massive heterotopia. The orderly production and migration of neurons occupying the NC likely occur in the *Pard3* cKO brain before E15.5, when the VZ and radial glial fiber scaffold remain prominent. On the other hand, the accumulating RGPs in the ectopic location undergo excessive proliferation and do not effectively generate neurons initially. Remarkably, the heterotopia is completely suppressed in the *Pard3;Yap;Taz*

cTKO brain. In accordance, the ectopic RGPs are greatly reduced in the *Pard3;Yap;Taz* cTKO cortex at the embryonic stage. These results confirm that the massive heterotopia originates from the ectopic RGPs. While cortical heterotopia has been observed previously (Cappello et al., 2006; Gil-Sanz et al., 2014; Jossin et al., 2017; Schmid et al., 2014), our study defines the distinct progenitor origin of heterotopia as well as the underlying signaling mechanism.

The initial change in RGP mitotic behavior and adult phenotype in the *Pard3* cKO cortex are reminiscent of those in the HeCo mouse that carries a retrotransposon insertion in *Echinoderm microtubule associated protein-like* 1 (*Eml1*) (Croquelois et al., 2009; Kielar et al., 2014). It is intriguing that both PARD3 and EML1 are microtubule-interacting proteins (Chen et al., 2013), indicating a potential importance of microtubule regulation in RGPs for division mode control. Interestingly, *EML1* mutations have been genetically linked to human megalencephaly and giant ribbon-like heterotopia with epilepsy and intellectual disability (Kielar et al., 2014). This relatively rare type of cortical malformation is distinct from the classic human SBH linked to mutations in genes encoding other microtubules or microtubule-associated proteins predominantly involved in controlling neuronal migration, such as *α1-Tubulin* (*TUBA1A*), *Lissencephaly 1* (*LIS1*, also known as *PAFAH1B1*), and *Doublecortin* (*DCX*) (Bizzotto and Francis, 2015). Notably, the etiology of megalencephaly in association with giant heterotopia in human patients remains largely unclear, as the cortex in the HeCo mouse is not obviously enlarged (normocephalic). In comparison, our study demonstrates that *Pard3* deletion causes a drastic cortical malformation that is highly reminiscent of human megalencephaly with giant ribbon-like heterotopia, as well as increased seizure susceptibility. Therefore, our study highlights a progenitor origin of cortical malformation linked to progenitor organization and division mode control, and provides insights into the pathophysiology of a severe, atypical form of human disorder.

Chapter 3 PARD3 links progenitor behavior and interneuron specification in the mammalian brain

3.1 Introduction

Accurate information processing in the CNS entails the balance of excitation and inhibition. Excitation comes from the excitatory neurons which secret the neurotransmitter glutamate and produce the main output of neural circuits. Inhibition, on the other hand, arises from interneurons which employ the neurotransmitter gamma aminobutyric acid (GABA) to inhibit the target neuron from firing. Although outnumbered by excitatory neurons in the cerebral cortex, inhibitory interneurons are incredibly diverse in terms of their morphology, molecular marker expression, electrical properties, subcellular connectivity and cellular connectivity **(Figure 3.1)** (DeFelipe et al., 2013; Maass et al., 2004; Markram et al., 2004; Miyoshi et al., 2007; Petilla Interneuron Nomenclature Group et al., 2008; Wonders and Anderson, 2006; Xu et al., 2004), and it is such the high variety of interneuron subtypes that equips the inhibition system with the power to accurately sense the level of excitation across a broad dynamic range.

Early population level lineage tracing studies demonstrated the distinct developmental origin of interneurons from that of excitatory neurons (Anderson et al., 2002; Luskin et al., 1993; Parnavelas et al., 1991; Tan et al., 1998). While excitatory neurons are born in the dorsal telencephalon, most if not all interneurons come from the ventral telencephalon, which is composed of ganglionic eminence (GE) and the PoA. The GE is a transient structure which only exists during embryonic development, and can be further subdivided into lateral, medial, and caudal domains (LGE, MGE, and

CGE, respectively). The PoA localizes ventral to the MGE. In the forebrain of mice, except for the interneurons destined for the striatum and olfactory bulb, all remaining

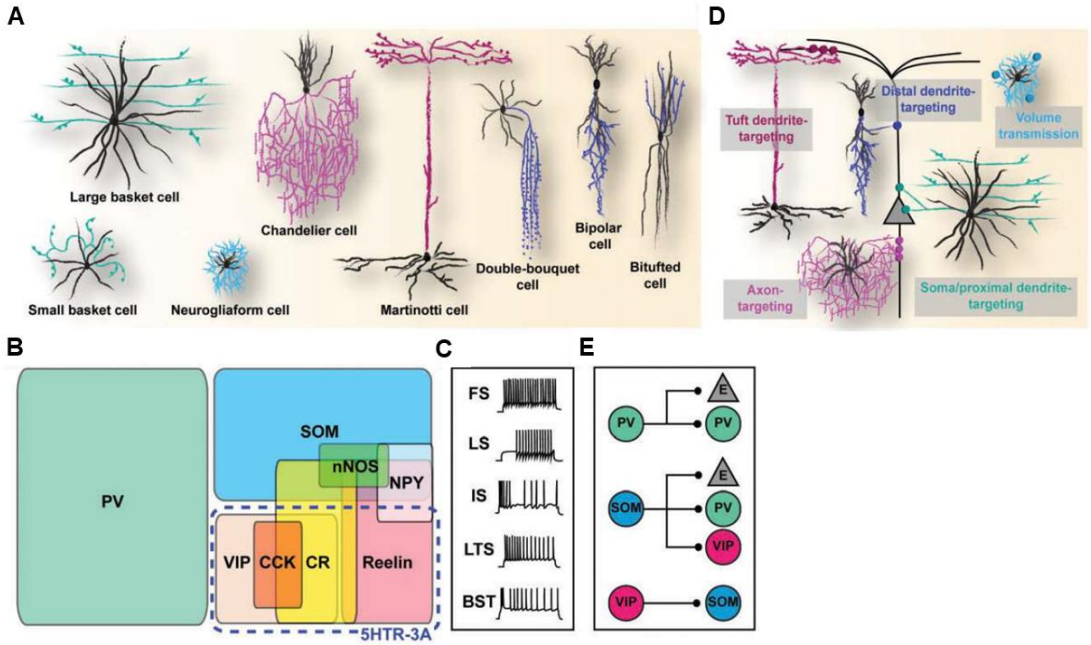

Figure 3.1: Multiple dimensions of cortical interneuron diversity.

(A) Morphologically defined subtypes of interneurons. **(B)** Classification of subtypes based on molecular marker expression. PV, parvalbumin; SOM, somatostatin; VIP, vasointestinal peptide; CR, calretinin; CCK, cholecystokinin; NPY, neuropeptide Y; 5HTR-3A, serotonin receptor 3A. **(C)** Electrophysiological classification of interneurons based on the action potential response pattern upon electrical stimulation. FS, fast-spiking; LS, late-spiking; IS, irregular-spiking; LTS, low threshold spiking; BST, bursting. **(D)** Diversity in subcellular targeting. **(E)** Diversity in cellular targeting. E, excitatory neuron. Adapted from Sultan and Shi (2018).

are derived from the MGE, CGE, and PoA **(Figure 3.2)** (Deacon et al., 1994; Olsson et al., 1995, 1998; Stenman et al., 2003; Wichterle et al., 2001). Among these three regions, the major source of cortical interneurons is the MGE which produces around 70% of all cortical interneurons in mice (Rakic, 2009). Previous studies have identified two

prominent non-overlapping interneuron populations originating in the MGE: SOM-positive (Martinotti and other) cells and PV-positive (basket and chandelier) cells

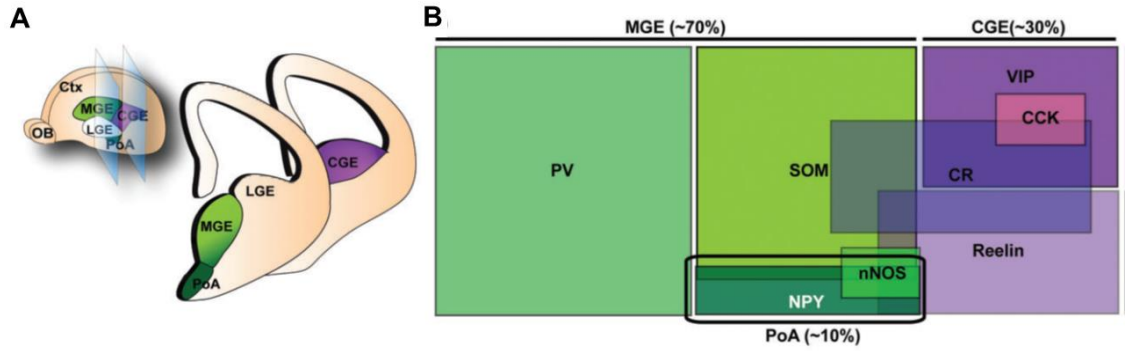

Figure 3.2: Developmental origins of cortical interneurons.

(A) Cortical interneurons in mice are derived from progenitor cells located in the proliferative zone of the ventral telencephalon, specifically in the medial ganglionic eminence (MGE), caudal ganglionic eminence (CGE) and preoptic area (PoA). LGE, lateral ganglionic eminence; Ctx, cortex; OB, olfactory bulb. **(B)** The major source of interneurons is the MGE, generating ~70% of cortical interneurons comprised of two nonoverlapping populations expressing parvalbumin (PV) and somatostatin (SOM). Approximately 30% of cortical interneurons are a heterogeneous group of cells generated by the CGE, all of which express 5HTR (serotonin receptor)-3A as well as either vasointestinal peptide (VIP) or reelin. In addition, CGE is the main source of calretinin (CR) and cholecystokinin (CCK)-expressing cells. The PoA generates ~10% of interneurons a fraction of which express neuropeptide Y (NPY), neuronal nitric oxide synthase (nNOS), and SOM. Adapted from Sultan and Shi (2018).

(Rudy et al., 2011; Xu et al., 2008). The two populations are found throughout different layers of the cortex with slightly different distribution pattern. SOM-expressing interneurons are preferentially enriched in deep layers whereas PV-expressing interneurons localize evenly across all layers. The two populations have distinct temporal origins as well. The fate-mapping analysis of MGE progenitors revealed that SOM-positive interneurons display a temporal decline in output: around 30% of the labeled interneurons are positive for SOM between E9.5 and E12.5, however, only around 10% of the labeled interneurons express SOM at E15.5. On the other hand, the percentages of PV-positive cells in total labeled interneurons are relatively constant at

any time point from E9.5 to E15.5 (Miyoshi et al., 2007). These results indicate that SOM-positive interneurons are produced earlier whereas PV-positive interneurons are generated at a constant rate throughout the embryonic interneuron generation in the MGE.

It is well established that interneurons generated from the MGE and PoA come from the neuron stem cells sitting in the VZ of these two areas. By taking advantage of mouse genetics combined with in utero retroviral injection, one previous study from our lab was able to sparsely label the dividing progenitors and their progeny in the MGE and PoA, and reported their radial glial cell nature (Brown et al., 2011). During the interneuron generation period (between E9.5 and E17.5), the RGPs in the MGE and PoA undergo interkinetic nuclear migration and divide in an asymmetric fashion to self-renew and simultaneously generate either a postmitotic interneuron or an IP. IPs then migrate into the SVZ and undergo symmetric division to further give rise to multiple interneurons (Brown et al., 2011).

Recently, another study of our lab showed two populations of RGPs with distinct radial glial fiber characteristics in the embryonic MGE (Tan et al., 2016). One population of RGPs projects long radial glial fibers reaching the pial surface, while the other exhibits relatively shorter radial glial fibers anchoring to the periventricular vessels. After systematically analyzing the temporal development of RGP-vessel association in the MGE, the authors found a progressive increase of vessel-anchored RGPs and a concomitant loss of pia-anchored RGPs. At the early embryonic stage (before E12.5), the majority of RGPs are anchored to the pial basement membrane with no obvious association with vessels, similar to those in the dorsal telencephalon responsible for producing neocortical excitatory neurons. However, as development proceeded, proliferative RGPs in the MGE became progressively anchored to the

periventricular vessels, so that by E16.5, vessel-anchored RGPs became the dominant population of mitotic RGPs in the MGE. In addition, specific disruption of the vessel-anchored RGPs lead to a loss of PV- and, to a lesser extent, SOM-expressing interneurons (Tan et al., 2016). These results suggest an important role of vessel-anchored RGPs in the production and proper function of neocortical interneurons.

Comparing to the significant progress made in the field of excitatory neurogenesis, our understanding of interneuron neurogenesis, specifically, how progenitor behavior influences interneuron diversity, has largely lagged. It remains unclear whether the diverse interneurons originate from a common pool of multipotent neural progenitors or a fate-restricted pool of progenitors in the MGE/PoA, and whether the asymmetric division of RGPs in the MGE/PoA play any roles in interneuron subtype specification. In the study introduced in this chapter, we attempted to investigate the function of PARD3 in division mode control of RGPs in MGE/PoA and interneuron subtype specification.

3.2 *Pard3* deletion in MGE/PoA RGPs leads to an increase in the number of SOM-expressing interneurons at the expense of PV-expressing interneurons

To dissect the function of PARD3 in controlling RGP organization and division during MGE interneuron development, we first set out to analyze the spatial expression pattern of PARD3 in the embryonic MGE. At E11.5, a strong enrichment of PARD3 immunoreactivity was observed at the apical surface of the VZ in the MGE. This pattern is similar to that in neocortex, and suggests that PARD3 might also be able to mediate asymmetric division of RGPs in the MGE **(Figure 3.3B, left)**.

We next crossed *Pard3*$^{fl/fl}$ mouse line to the *NKX2.1*-Cre (Xu et al., 2008), in which Cre recombinase is selectively expressed in RGPs of the development MGE/PoA as early as E9.5. While PARD3 was extensively expressed at the VZ surface in the wild

type MGE/PoA, it was depleted in the VZ of the *Pard3* cKO MGE/PoA at E11.5 **(Figure 3.3A, B)**.

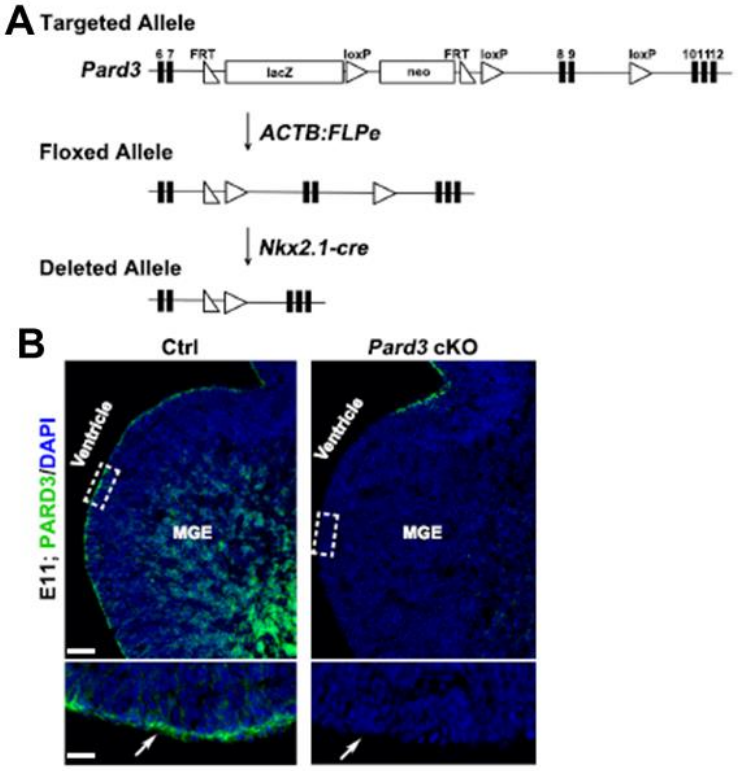

Figure 3.3: Selective removal of PARD3 in NKX2.1^{+} MGE/PoA RGPs.

(A) Schematic diagram showing the generation of *Nkx2.1-Cre; Pard3*$^{fl/fl}$ (referred to as *Pard3* cKO) mice. Numbered black boxes represent exons. Deletion of exons 8 and 9 leads to a frame shift of subsequent exons. **(B)** Images of control and *Pard3* cKO MGE at E11 stained for PARD3 (green) and counterstained with DAPI (blue). High magnification images of the VZ surface (broken rectangles) are shown at the bottom. Note the loss of PARD3 at the VZ surface in the *Pard3* cKO MGE (arrows). Scale bars: 70 µm and 15 µm.

In order to accurately assess the interneuron population originating from the MGE/PoA, we took advantage of a well-established Ai9 reporter mouse line (Madisen et al., 2010), in which the red fluorescent signal from tdTomato is strictly driven by Cre recombinase. We integrated *Ai9* reporter allele into the *NKX2.1*-Cre; *Pard3*$^{fl/fl}$ mouse line to specifically mark the interneurons generated by the RGPs in the MGE/PoA, and

quantified the number of tdTomato-expressing cells, PV/tdTomato and SOM/tdTomato double positive interneurons in the cortex. The quantification results showed that PARD3 removal leads to a 25% reduction of the density of PV/tdTomato double positive interneurons but a 15% promotion of the density of SOM/tdTomato double positive interneurons. Collectively, the total density of tdTomato expressing cells was decreased by 10% in *Pard3* cKO cortices compared with the control brains **(Figure 3.4)**.

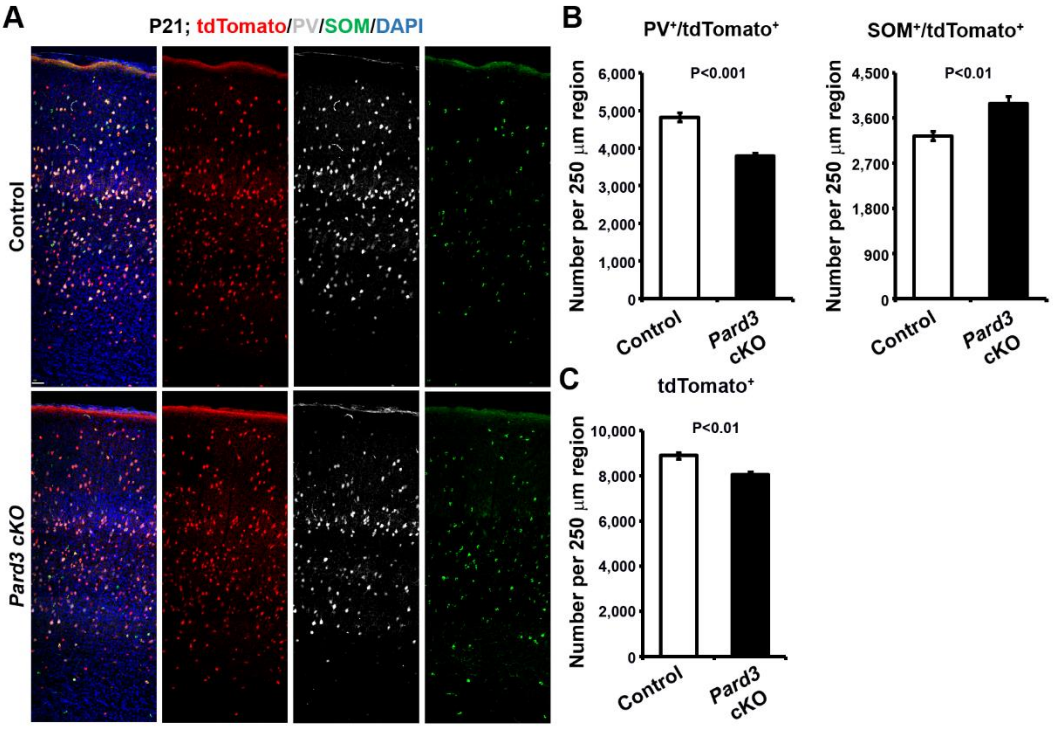

Figure 3.4: Selective removal of PARD3 in NKX2.1$^+$ MGE/PoA RGPs leads to the overproduction of SOM-expressing interneurons at the expense of PV-expressing interneurons.

(A) Representative confocal images of P21 control, *Pard3* cKO, cortices stained for TdTomato (red), PV (grey), and SOM (green) and counter-stained for DAPI (blue). Scale bar: 30 μm. **(B)** Quantification of the number of PV$^+$/tdTomato$^+$ (left) and SOM$^+$/tdTomato$^+$ (right) cells per 200 μm radial column in P21 control, *Pard3* cKO cortices (n=6 brains per genotype; unpaired two-tailed t-test with Welch's correction). **(C)** Quantification of the number of tdTomato$^+$ cells per 200 μm radial column in P21 control, *Pard3* cKO cortices (n=6 brains per genotype; unpaired two-tailed t-test with Welch's correction).

These results suggest that PARD3 deletion in the RGPs of the MGE/PoA results in an overproduction of early born SOM-positive interneurons and a concomitant reduction in the number of constantly generated PV-positive interneurons.

3.3 *Pard3* deletion disrupts asymmetric division of RGPs in a temporal distinct fashion

To understand the origins of altered interneuron generation in the *Pard3* cKO brains, we next examined RGP behavior at multiple embryonic stages which cover almost the entire period of embryonic interneuron development in the MGE/PoA. The wild type and *Pard3* cKO brains were stained with an antibody against OLIG2 (Miyoshi et al., 2007), a transcription factor highly expressed in RGPs of the ventral telencephalon including the MGE/PoA. We observed a significant increase in the density of $OLIG2^+$ cells in both VZ and extra-VZ regions of the MGE/PoA in the *Pard3* cKO brains at early time points (E11.5 and E13.5 in **Figure 3.5**). However, the generation of $OLIG2^+$ cells was gradually suppressed at late time points upon *Pard3* deletion, and hence the density of $OLIG2^+$ cells in the MGE/PoA was reduced in the *Pard3* cKO brains compared with the wild type brains at E16.5 **(Figure 3.5)**. One caveat of such assessment is that OLIG2 signal can be found in oligodendrocyte precursor cells (OPCs) as well. OPCs are mitotically active cells that are restricted to the oligodendroglial lineage and are characterized by the expression of platelet-derived growth factor receptor alpha (PDGFRα) (Tripathi et al., 2010). Oligodendrogenesis within the MGE/PoA commences at E11.5 and peaks at E13.5. Around E15.5, OPCs in the MGE/PoA migrate into the cerebral cortex and differentiate into myelinating oligodendrocytes. Whereas PDGFRα expression in the embryonic MGE/PoA is specific to the OPC lineage, OLIG2 is also expressed in multipotent progenitors (Petryniak et al., 2007). In order to examine oligodendrogenesis in *Pard3*cKO MGE/PoA, PDGFRα immunostaining was employed to assess the production of OPCs

Figure 3.5: *Pard3* deletion causes abnormal RGP dynamics in the MGE/PoA.

(A) Representative confocal images of E11.5, E13.5, E15.5 and E16.5 MGE/PoA in control and *Pard3* cKO mouse brains stained for OLIG2 (green) and counterstained with DAPI (blue). Scale bar: 100 μm. **(B)** Quantification of the density of $OLIG2^{+}$ cells in the VZ per 250 μm column in the VZ and extra-VZ areas of the MGE/PoA. (n=7 sections from 3 control brains, and n=10 sections from 7 *Pard3* cKO brains). N.S., not significant; (unpaired t-test with Welch's correction).

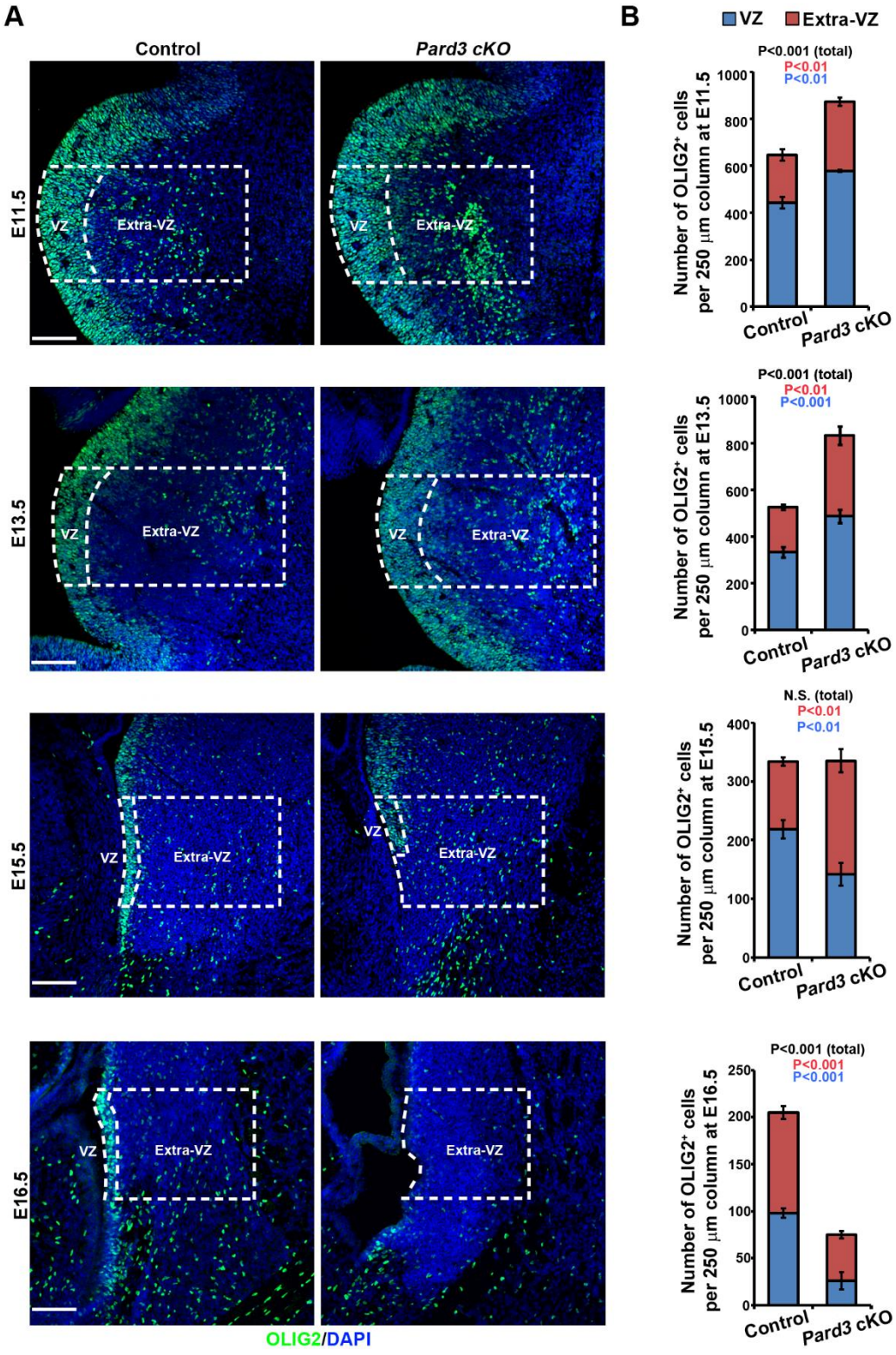
A
Control
Pard3 cKO
E11.5
E13.5
E15.5
E16.5
VZ
Extra-VZ
OLIG2/DAPI
B
VZ
Extra-VZ
P<0.001 (total)
P<0.01
P<0.01
Number of OLIG2+ cells per 250 μm column at E11.5
P<0.001 (total)
P<0.01
P<0.001
Number of OLIG2+ cells per 250 μm column at E13.5
N.S. (total)
P<0.01
P<0.01
Number of OLIG2+ cells per 250 μm column at E15.5
P<0.001 (total)
P<0.001
P<0.001
Number of OLIG2+ cells per 250 μm column at E16.5
Control
Pard3 cKO

in the *Pard3* cKO brains. The result indicated that there was no obvious change in the number or localization of OPCs at E11.5 and E13.5 **(Figure 3.6)**, and hence the observed alteration in the density of $OLIG2^{+}$ cells upon PARD3 depletion only reflects the abnormal RGP dynamics in the MGE/PoA.

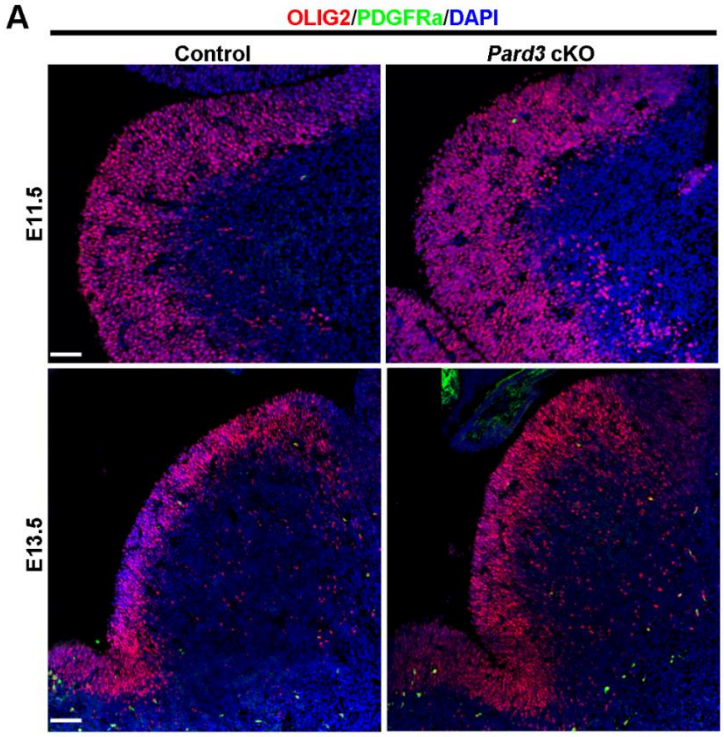

Figure 3.6: *Pard3* deletion does not impair OPC generation.

(A) Representative confocal images of E11.5, E13.5 MGE/PoA in control and *Pard3* cKO mouse brains stained for OLIG2 (red), PDGFRα (green) and counterstained with DAPI (blue). Scale bar: 100 μm.

Asymmetric division of RGPs ensures an intricate balance between RGP renewal/maintenance and neurogenesis. The change of RGP dynamics in the *Pard3* cKO MGE/PoA may be due to a defect in RGP asymmetric division. To directly test this, we performed *in vivo* clonal analysis to explicitly assess the division mode of individually dividing RGPs in the MGE/PoA. We injected serially diluted, low-titer

retroviruses expressing EGFP into the lateral ventricle at E12.5/E14.5 and recovered the brain at E13.5/E15.5 for analysis. To examine the division mode of sparsely labeled RGPs in the MGE/PoA, brains were serially sectioned and stained with antibodies against OLIG2 and Ki67, a proliferative cell marker. We identified all sparsely labeled cell pairs in the MGE/PoA that originated from individual dividing RGPs by 3D reconstruction. In these experiments, $OLIG2^{+}/Ki67^{+}$, $OLIG2^{-}/Ki67^{+}$, and $OLIG2^{-}/Ki67^{-}$ cells corresponded to RGPs, IPs, and post-mitotic interneurons (INs), respectively. As expected, at early neurogenesis stage (E13.5), the majority (~68%, 17 out of 25) of the cell pairs in the wild type control MGE contained a bipolar RGP and a multi-polar IP or IN, indicating asymmetric division. In contrast, only a small fraction (~19.0%, 8 out of 42) of the cell pairs in the *Pard3* cKO MGE contained a bipolar RGP and a multi-polar IP or IN; instead, the vast majority (~57.1%, 24 out of 42) of the cell pairs contained two RGPs **(Figure 3.7B-D)**, indicating symmetric proliferation division. The depletion of PARD3 at late neurogenesis stage (E15.5) disrupt asymmetric division of RGPs in the MGE/PoA as well (~ 80%, 28 out of 35 in control vs. ~19.5%, 8 out of 41 in *Pard3* cKO). But majority (~68.3%, 28 out of 41) of the cell pairs in *Pard3* cKO brains are composed of two IPs or two Ins, which is indicative of symmetric terminal division **(Figure 3.8B-D)**. Together, these results suggest that PARD3 removal leads to a switchin RGP division mode from asymmetric neurogenic division (one RGP and one IP or IN) to symmetric division (i.e., two RGPs at the early time point, whereas two IPs or two Ins at late time point).

3.4 PARD3 regulates chandelier cell production via RGP asymmetric division

We next further examined the consequence of impaired RGP asymmetric division on interneuron production. Here we exploited chandelier cells as an example

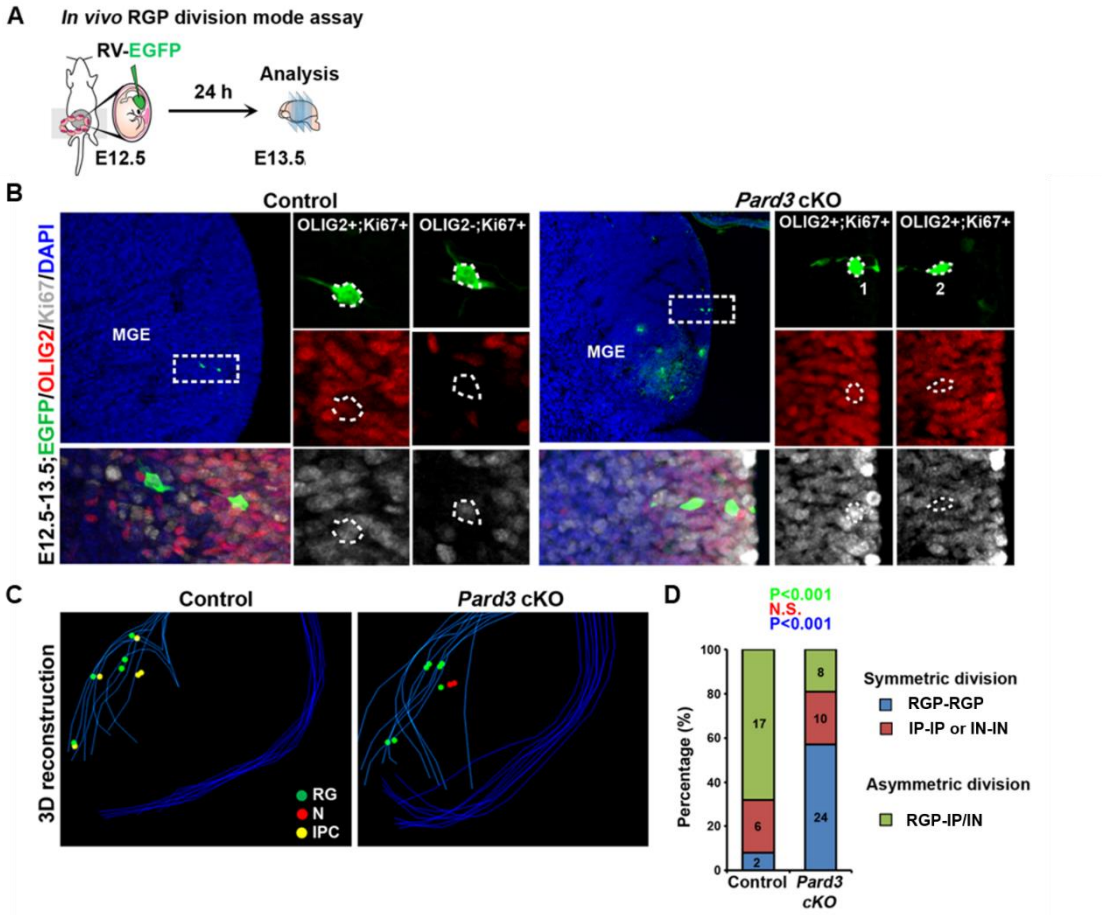

Figure 3.7: PARD3 deletion promotes NKX2.1^{+} MGP/PoA RGP asymmetric proliferative division at early neurogenesis stage.

(A) Schematic of *in vivo* clonal analysis to assess RGP division pattern. (B) Images of E13.5 control and *Pard3* cKO mouse brains injected with low-titer EGFP-expressing retrovirus (green) at E12.5, and stained for Ki67 (white) and OLIG2 (red), and counterstained with DAPI (blue). High magnification images of the EGFP-expressing cell pairs (broken rectangles) are shown to the right. Scale bars: 50 μm, 20 μm. (C) 3D reconstruction images of control and *Pard3* cKO MGE/PoA showing EGFP-expressing cell pairs containing RGP (green), IP (yellow), or interneurons (IN, red) from E12.5 to E13.5. (D) Percentage of EGFP-expressing cell pairs representing symmetric proliferative division, asymmetric neurogenic division, or symmetric terminal division in the MGE/PoA of control and *Pard3* cKO brains from E12.5 to E13.5. (Chi-square test).

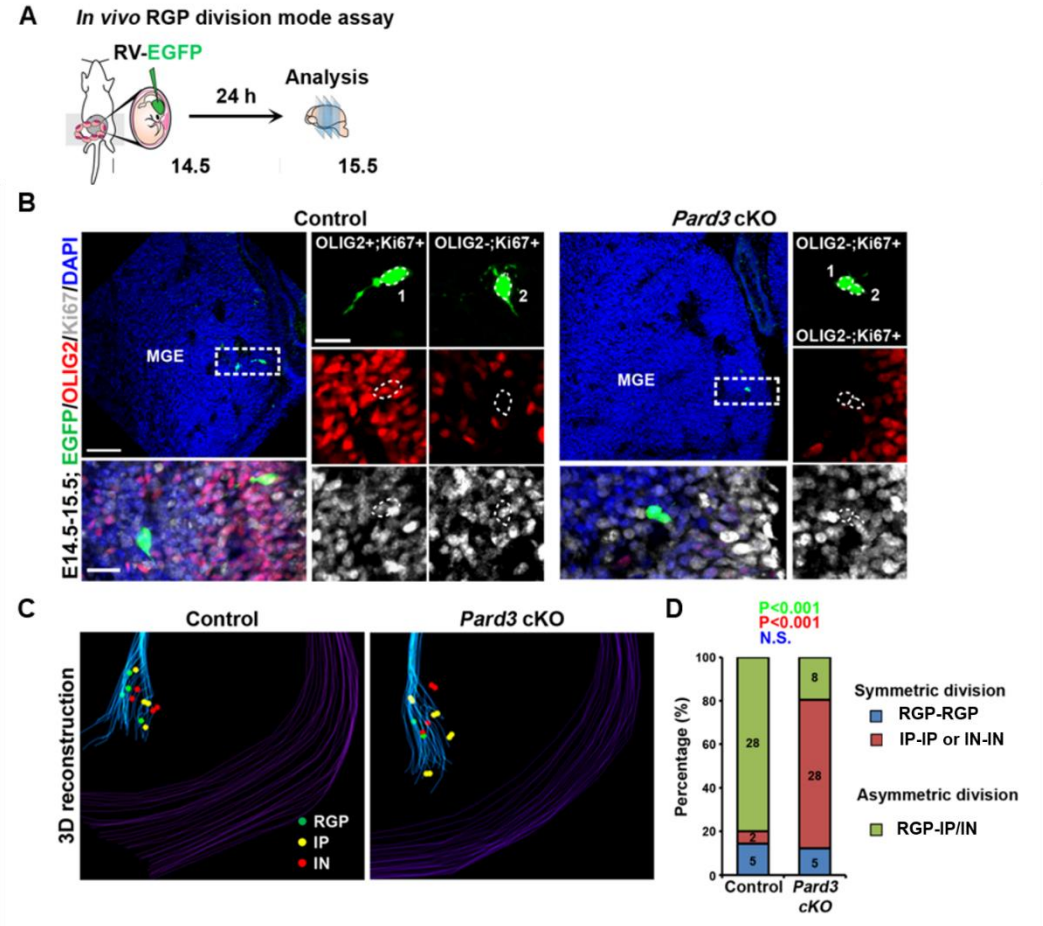

Figure 3.8: PARD3 deletion promotes NKX2.1^{+} MGP/PoA RGP asymmetric terminal division at late neurogenesis stage.

(A) Schematic of *in vivo* clonal analysis to assess RGP division pattern. (B) Images of E15.5 control and *Pard3* cKO mouse brains injected with low-titer EGFP-expressing retrovirus (green) at E13.5, and stained for Ki67 (white) and OLIG2 (red), and counterstained with DAPI (blue). High magnification images of the EGFP-expressing cell pairs (broken rectangles) are shown to the right. Scale bars: 50 µm, 20 µm. (C) 3D reconstruction images of control and *Pard3* cKO MGE/PoA showing EGFP-expressing cell pairs containing RGP (green), IP (yellow), or interneurons (IN, red) from E14.5 to E15.5. (D) Percentage of EGFP-expressing cell pairs representing symmetric proliferative division, asymmetric neurogenic division, or symmetric terminal division in the MGE/PoA of control and *Pard3* cKO brains from E14.5 to E15.5. (Chi-square test).

to assess interneuron generation deficit in the *Pard3* cKO brains. Chandelier cell, which possesses numerous characteristic vertical cartridges, is one of the few interneuron cell

types that can be meaningfully recognized based on the morphology alone, and has been recently suggested to be selectively generated by NKX2.1-expressing progenitor cell in the MGE/PoA at the late embryonic stage (after E15.5). In addition, one of the ongoing studies of our lab, by combining retrovirus fate mapping experiment with EdU pulse-chase analysis, revealed that chandelier cells born at the late neurogenic stage (E15.5) are originated from the early labeled (E12.5) $NKX2.1^{+}$ RGPs undergoing several rounds of asymmetric divisions before the final differentiate division. This result suggests a putative link between division mode of RGPs and interneuron subtype specification, and hence prompts us to analyze chandelier cell production in the *Pard3* cKO brains.

We performed *in utero* intraventricular injection of pUX-FLEX Cre-dependent EGFP-expressing retrovirus into the wild type control and *Pard3* cKO brains at E15.5 **(Figure 3.9)**. Brains were collected at P21 and subjected to 3D stereological analysis to systematically examine EGFP-expressing chandelier cells in the neocortex **(Figure 3.9A)**. While the control brain contained 16.0±4.0 chandelier cells per neocortical hemisphere (14.8±3.0% of EGFP-expressing population), the *Pard3* cKO brain contained only ~6.0±1.0 chandelier cells per neocortical hemisphere (5.5±0.8% of EGFP-expressing population) **(Figure 3.9B, C)**.

We further examined the superficial and deep layer chandelier cell output. Both superficial and deep layer chandelier cells are generated at the late embryonic stage, and deep layer population is largely produced after superficial layer population. There was a significant reduction in the number of labeled chandelier cells in layer 2 per neocortical hemisphere in the *Pard3* cKO brain (4.0±3.0; 19.2±2.4% of EGFP-expressing population in layer 2) compared with the control brain (10.0±3.0; 37.8±7.3%)

Figure 3.9: PARD3 regulates Chandelier cell production via RGP asymmetric division.

(A) Schematic of the experimental design. Animals received *in utero* injection of Cre-dependent EGFP-expressing retrovirus at E15 were analyzed at P21. **(B)** 3D reconstruction images of P21 control (Ctrl) and *Pard3* cKO neocortical hemispheres with EGFP-expressing chandelier cells and non-chandelier cells. Black and grey dots represent the cell bodies of EGFP-expressing chandelier cells and non-chandelier cells, respectively. A, anterior; P, posterior; D, dorsal; V, ventral; M, medial; L, lateral. **(C)** Quantification of the number (left) and percentage (right) of chandelier cells among EGFP-expressing interneurons per neocortical hemisphere (control, n=10 hemispheres; *Pard3* cKO, n=16 hemispheres). Center line, median; box, interquartile range; whiskers, minimum and maximum. ** P=0.003 (Mann-Whitney test). **(D)** 3D reconstruction images of P21 control and *Pard3* cKO neocortical hemispheres with EGFP-expressing chandelier cells and non-chandelier cells in layer 2. Red and grey dots represent the cell bodies of EGFP-expressing chandelier cells and non-chandelier cells, respectively, in layer 2. **(E)** Quantification of the number (left) and percentage (right) of chandelier cells among EGFP-expressing interneurons in layer 2 per neocortical hemisphere (control, n=10 hemispheres; *Pard3* cKO, n=16 hemispheres). Center line, median; box, interquartile range; whiskers, minimum and maximum. * P=0.04 (left); * P=0.03 (right) (Mann-Whitney test). **(F)** 3D reconstruction images of P21 control and *Pard3* cKO neocortical hemispheres with EGFP-expressing chandelier cells and non-chandelier cells in layers 5/6. Blue and grey dots represent the cell bodies of EGFP-expressing chandelier cells and non-chandelier cells, respectively, in layers 5/6. **(G)** Quantification of the number (left) and percentage (right) of chandelier cells among EGFP-expressing interneurons in layers 5/6 per neocortical hemisphere (control, n=10 hemispheres; *Pard3* cKO, n=16 hemispheres). Center line, median; box, interquartile range; whiskers, minimum and maximum. * P=0.01; *** P=0.0007 (Mann-Whitney test).

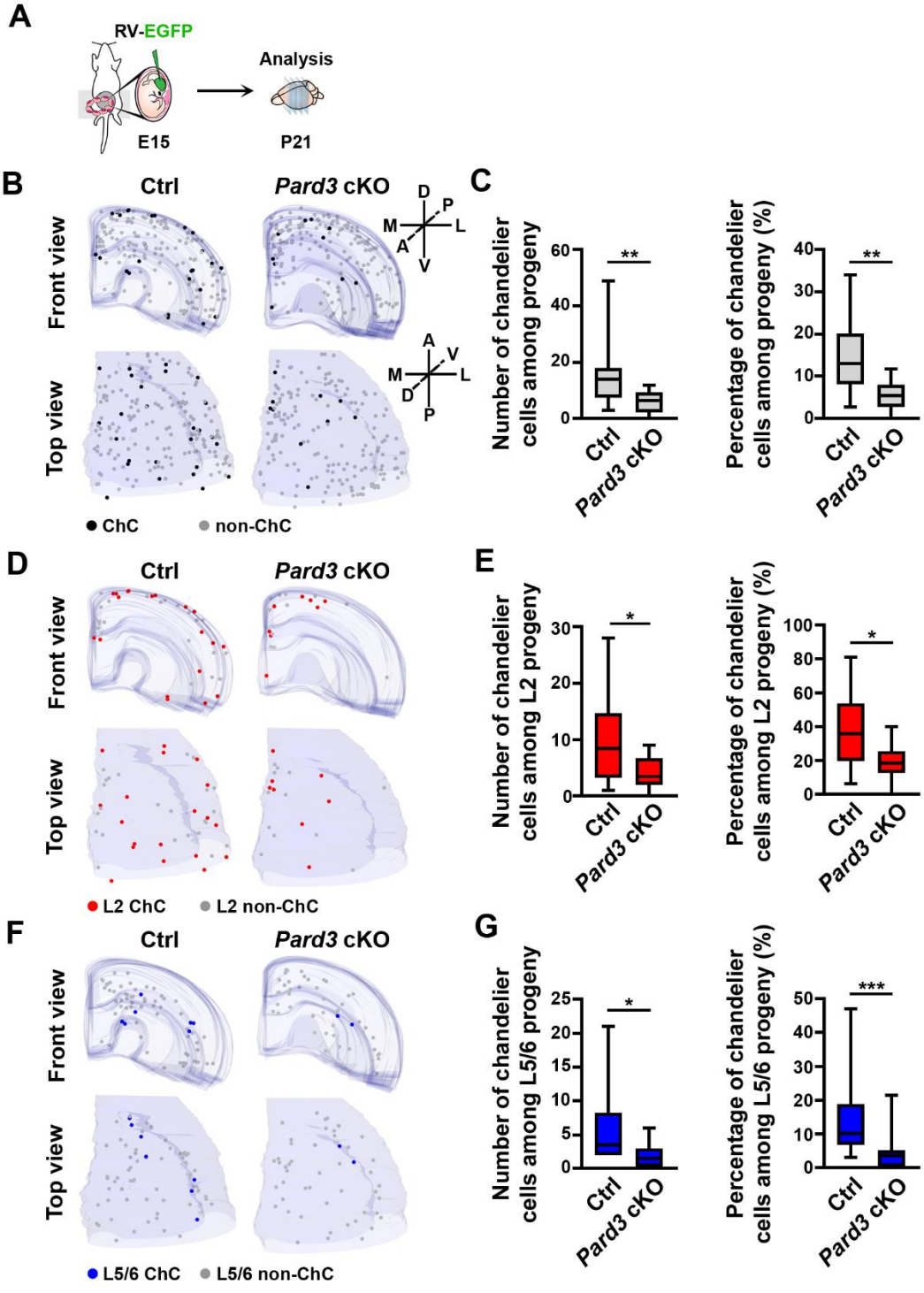
A
RV-EGFP
Analysis
E15
P21
B
Ctrl
Pard3 cKO
Front view
Top view
D
P
M
L
A
V
ChC
non-ChC
C
Number of chandelier cells among progeny
Percentage of chandelier cells among progeny (%)
**
Ctrl
Pard3 cKO
D
Ctrl
Pard3 cKO
Front view
Top view
L2 ChC
L2 non-ChC
E
Number of chandelier cells among L2 progeny
Percentage of chandelier cells among L2 progeny (%)
*
F
Ctrl
Pard3 cKO
Front view
Top view
L5/6 ChC
L5/6 non-ChC
G
Number of chandelier cells among L5/6 progeny
Percentage of chandelier cells among L5/6 progeny (%)
*
***

of EGFP-expressing population in layer 2) **(Figure 3.9D, E)**. Similarly, the number of labeled chandelier cells in layers 5/6 significantly decreased from 6.0±2.0 (14.7±4.2%of EGFP-expressing population in layers 5/6) in the control brain to 2.0±0.5 (4.1±1.3% of EGFP-expressing population in L5/6) in the *Pard3* cKO brain **(Figure 3.9F, G)**. Together, these results clearly suggest that PARD3 is crucial for the generation of both superficial and deep layer chandelier cells via regulating MGE/PoA RGP asymmetric division.

3.5 Discussion

Significant efforts have been made to delineate distinct types of interneurons in the neocortex, yet little is known about the developmental program of producing diverse neocortical interneurons. Specifically, it remains largely unclear how RGPs in the MGE/PoA give rise to different subtypes of neocortical interneurons. One of the ongoing studies of our lab might have potential to provide insights into this field. By systematically examining the developmental origins of chandelier cells, which is one of the well-established interneuron subtypes, and born at late neurogenic stages, our lab found a pool of MGE/PoA RGPs with multipotency that divide in a consecutive asymmetric fashion to progressively generate distinct subtypes of neocortical interneurons, with chandelier cells among the last output. This finding suggests a putative link between asymmetric division of RGPs in the MGE/PoA and interneuron subtype specification, and hence prompts us to investigate interneuron generation in *Pard3* cKO brains.

In our mutant analysis, at late neurogenic stages (after E14.5), selectively deletion of PARD3 in MGE/PoA RGPs leads to a switch from asymmetric division to symmetric terminal division, and consequently significant loss of both deep and

superficial layer chandelier cells. These results are in line with the interneuron population analysis of our lab mentioned above, and further demonstrate that proper RGP asymmetric division is critical for the generation of the correct number and types of neocortical interneurons.

In addition to the reduction in the number of chandelier cells of both deep and superficial layer, we found the overproduction of early-born SOM-positive interneurons. Unfortunately, the current dataset we have fails to explain the mechanisms underlying this overproduction. One of the putative contributors to the deficit of SOM-expressing interneurons in *Pard3* cKO brains is IPs. Several previous studies revealed the robust amplification of SVZ divisions in the ventral region of the telencephalon. Different from their dorsal counterparts, IPs in the MGE/PoA were found to undergo multiple rounds of symmetric divisions by live imaging and clonal labeling (Brown et al., 2011). Moreover, the SVZ, the region where a majority of IPs are located, in the MGE is greatly expanded as development proceeds, whereas the number of RGPs in the VZ of the MGE appears to decrease progressively. Although IPs may play an increased role in the generation of the appropriate numbers and diversity of cortical interneurons, the *bona fide* marker of this type of progenitor still remains to be found. Our analysis of IP generation in the *Pard3* cKO brains is halted as well due to the lack of well-established IP marker. Notably, the rapid advances in single cell sequencing techniques open the possibility of identifying accurate markers of various cell types in the MGE/PoA. These efforts may provide us powerful tools to investigate IP generation and dissect the putative link between IP and interneuron subtype specification.

Another potential contributor to the overgrowth of SOM-expressing interneurons is the ectopic OLIG2$^+$ RGPs in the *Pard3* cKO brains. Our immunostaining result revealed the excessive OLIG2$^+$ RGPs in the SVZ upon *Pard3* deletion between

E11.5 and E13.5, the time points in which the peak generation of SOM+ interneurons occurs (Miyoshi et al., 2007). Meanwhile, our *in vivo* division pattern analysis demonstrated that the symmetric terminal division does not impaired in the *Pard3* cKO brains at early neurogenic stage (E12.5-13.5). These results suggest a possibility that ectopic $OLIG2^+$ RGPs in the SVZ may undergo symmetric terminal division to selectively produce SOM^+ interneurons before E13.5. This hypothesis, generally, is consistent with our mutant analysis results of the neocortex discussed in chapter 2: the outcome of the symmetric division upon *Pard3* removal is affected by the environment/niche parameters, such as NOTCH/HIPPO signaling intensity (Liu et al., 2018). Indeed, a significant population of RGPs accumulate in the SVZ in *Pard3* cKO MGE, a niche where extensive symmetric terminal divisions of IPs happen. Therefore, it would be interesting to selectively examine the dividing behavior and output of ectopic RGPs by a combination of single cell dissection, *in vitro* cell culture, and transplantation experiments.

Sonic hedgehog signaling (SHH) can be a potential contributor to SOM^+ interneuron overproduction in the *Pard3* cKO brains as well. One elegant study published on Neuron reported that a high level of SHH signaling favors the generation of the SOM-expressing interneurons at the expense of PV-expressing subgroup (Xu et al., 2010). Although PARD3 hasn't been reported to directly regulate SHH signaling, aPKC, another key member of PAR complex which interacts with PARD3 is identified as a novel SHH regulator in mouse basal cell carcinoma (BCC) cell lines (Atwood et al., 2013). Therefore, one of the future directions for the MGE/PoA mutant analysis would be the assessment of SHH signaling level in the *Pard3* cKO brains.

Chapter 4 Conclusion and future directions

4.1 Introduction

My thesis study attempted to define functions of polarity protein, PARD3, in cortical neurodevelopment. By generating a conditional *Pard3* mutant mouse line, and crossed it to two distinct Cre mouse lines, Emx1-Cre and NKX2.1-Cre, in which Cre recombinase is selectively expressed in RGPs of the developing neocortex and MGE/PoA, respectively, I was able to conduct mutant analyses and assess the roles of PARD3 during development of the two key brain regions.

In chapter 2, which discusses my work performed in the developing cortex, the mutant analysis results showed that neocortical RGP behavior and cortical development are controlled by temporally distinct actions of PARD3 in concert with HIPPO signaling. Upon PARD removal, RGPs exhibit developmental stage-dependent abnormal switches in division mode, leading to an initial over-production of RGPs largely located outside the VZ at the expense of deep-layer neurons. Ectopically localized RGPs subsequently undergo accelerated and excessive neurogenesis, resulting in the formation of an enlarged cortex with massive heterotopia and increased seizure susceptibility. Simultaneous removal of HIPPO pathway effectors YAP and TAZ suppresses cortical enlargement and heterotopia formation. Taken together, these results define a dynamic regulatory program of mammalian cortical development and highlight a progenitor origin of megalencephaly with ribbon heterotopia and epilepsy.

In chapter 3, my mutant analysis done in the MGE/PoA demonstrated that proper RGP asymmetric division is critical for the generation of the correct number and types of neocortical interneurons. Similar to their counterparts in the neocortex, MGE/PoA RGPs lacking PARD3 display temporally distinct changes in division mode:

asymmetric division switches to symmetric proliferative/terminal division at early/late neurogenic stages, respectively. The division mode impairment leads to the initial overproduction of $OLIG2^{+}$; $PDGFR\alpha^{-}$ RGPs located within and outside the VZ of the MGE/PoA before E14.5, and a gradual reduction in the number of MGE/PoA RGPs after that. Moreover, this perturbation in asymmetric division suppresses the generation of chandelier cells of both deep and superficial layer. In conjunction with one of the ongoing studies of our lab, which identified that chandelier cells born at the late neurogenic stage (E15.5) are originated from the early labeled (E12.5) $NKX2.1^{+}$ RGPs undergoing several rounds of asymmetric divisions, my PARD3 mutant analysis in the MGE/PoA directly supports a progressive interneuron fate specific program in which neocortical interneuron diversity comes from consecutive asymmetric division of multipotent MGE/PoA RGPs.

4.2 The molecular underpinnings of temporally distinct function of PARD3

My dissertation studies in two key brain areas, neocortex and the MGE/PoA, reveal the regional conserved developmental stage-dependent role of PARD3 in determining the progeny output of RGPs' asymmetric division. At early neurogenic stage, between the two daughter cells of RGPs, the one inheriting PARD3 becomes the postmitotic neuron. On the contrary, PARD3 promotes the progenitor identity during late neurogenesis. These results help to resolve the controversy over reports of PARD3 knockdown phenotypes in mouse and zebrafish (Alexandre et al., 2010; Bultje et al., 2009; Costa et al., 2008; Dong et al., 2012), but the molecular mechanisms underlying the temporally distinct function of this protein is still unknown.

One of the putative contributors could be the multiple isoforms of PARD3. Three major PARD3 isoforms (180, 150 and 100 kDa) have been identified in a lysate prepared from E13.5 mouse embryonic tissue (Traweger et al., 2008). According to my western blot result shown in chapter 2 (**(Figure 2.1B)**, at least two PARD3 protein isoforms (180 and 100 kDa) can be detected in mouse neocortex at E12.5. This is in line with previous reports demonstrating that PARD3 protein variants are often expressed simultaneously within a specific cell type or tissue (Gao et al., 2002). The three major PARD3 isoforms share the conserved N terminal domain and three PDZ1 domains, but differ in C terminal elements. Although our understanding of the function of individual PARD3 variant is limited, one study revealed the different aPKC binding and phosphorylation affinities among major three PARD3 isoforms (Gao et al., 2002). Therefore, it is likely that distinct isoform of PARD3 may active at different neurogenic stages and contribute to the developmental phase-dependent function of PARD3. It would be interesting to identify the temporal expression pattern of each variant through the entire cortical neurogenesis by western blot, and selectively manipulate the level of single isoform to further assess the function.

Another potential contributor to the temporally distinct function of PARD3 could be the concentration difference of this protein between early and late neurogenic phases. The idea is inspired by one of the previous studies of our lab, which illustrated the conformation-dependent regulation of microtubule bundling by PARD3 in specifying neuronal polarity (Chen et al., 2013). As stated in this elegant work, under low concentration, PARD3 functions in the closed conformation through the intramolecular interaction between the N- and C- terminal domains, and possesses low

microtubule regulation activity. Whereas under high concentration, the intermolecular oligomerization of PARD3 promotes an open conformation and subsequently leads to strong microtubule bundling and stabilization activity. Notably, the expression intensity of PARD3 is gradually deceased during cortical neurogenesis: immunoreactivity is strong in early neurogenic stage and was almost absent in late stage (Costa et al., 2008). This reduction of PARD3 level correlates with the switch of division mode in *Pard3* cKO cortices, and therefore prompts the idea that this concentration mediated conformation change might result in the temporally distinct function of PARD3 in regulating the progeny output of asymmetric division of RGPs.

4.3 The identity and mitotic behavior of ectopic RGPs upon PARD3 deletion

Another regionally conserved phenotype upon PARD3 deletion, in addition to the developmental stage-dependent division mode change, is the generation of ectopically located RGP population. In chapter 2, by conducting a series of immunostaining experiments, we demonstrated that this population is positive for RGP markers, but negative for oRG makers. Retrovirus labeling experiment revealed the multipolar morphology of this population. Moreover, the division pattern clonal analysis suggested that ectopic $PAX6^+$ cells can actively divide to give rise to either progenitors or postmitotic neurons. All these results together proved that the newly generated $PAX6^+$ cells in extra-VZ upon PARD3 deletion are RGP-like progenitors. However, it is unclear that whether VZ RGPs and ectopic RGPs are the same with regard to transcriptome profile and mitotic behavior.

Since PARD3 has been reported to establish and maintain polarized distribution of cell fate determinants, it is expected that the two daughter cells from symmetric division of PARD3 deleted RGPs acquire the same amount of progenitor fate determinants as well as neuron fate determinants simultaneously. Consequently, the progenitors in PARD3 cKO brains would exhibit features of postmitotic neurons, migrate away from the VZ, and hence become the ectopic cells positive for progenitor markers.

Taken together, it will be interesting to conduct the comparisons of transcriptome profiles among ectopic RGPs in PARD3 cKO brains, VZ RGPs in PARD3 cKO brains and RGPs in control brains in order to further characterize this unique type of cells resulted from PARD3 removal. Performing live cell imaging to monitor the mitotic and migratory behaviors of ectopic RGPs would be another exciting future direction of this study.

EXPERIMENTAL PROCEDURES

Animals

The *Pard3* knockout-first (*Pard3*$^{tm1a(KOMP)Wtsi}$) ES cell line (EPD0334_1_C04) was obtained from the International Knockout Mouse Consortium (IKMC). After confirmation, ESC clones were injected into C57BL/6J blastocysts, and the resulting chimeras were crossed with C57BL/6J females to obtain germ-line transmission. The knockout-first allele was converted to the conditional allele by crossing with *B6.Cg-Tg(ACTFLPe*) mice (stock# 005703; The Jackson Laboratory) to excise the gene trap cassette. The resulting *Pard3*$^{fl/+}$ (fl, floxed allele) conditional mice were subsequently intercrossed to generate *Pard3*$^{fl/fl}$ mice, in which exons 8 and 9 were flanked by loxP sites. Deletion of exons 8 and 9 causes a frameshift in the subsequent exons. *Emx1-Cre* (stock#005628) and *Nex-Cre (Schwab et al. 2000)* mice were used to delete *Pard3* in the cortex. *R26-LSL-NICD* mice (stock#008159) and *Ai9-tdTomato* mice (stock# 007909) were purchased from The Jackson Laboratory. *Emx1-CreER, Rbpj*$^{fl/fl}$, *CBF:H2B-Venus*, *Yap*$^{fl/fl}$, and *Taz*$^{fl/fl}$ (Reginensi et al. 2013) mouse lines were kindly provided by Dr. N. Kessaris (University College London, UK), Dr. B. G. Novitch (University of California at Los Angles), Dr. A. K. Hadjantonakis (Memorial Sloan Kettering Cancer Center, MSKCC), Dr. Alexander L. Joyner (MSKCC) and Dr. Jeff Wrana (The Lunenfeld-Tanenbaum Research Institute, Canada), respectively. Genotyping was carried out using standard PCR protocols. The mice were maintained at the facilities of Memorial Sloan Kettering Cancer Center (MSKCC) and all animal procedures were approved by the MSKCC Institutional Animal Care and Use Committee (IACUC). For timed pregnancies, the plug date was designated as E0 and the date of birth was defined as P0.

Tissue Preparation, Immunohistochemistry, Confocal Imaging, and Quantification

Embryonic or adult mice were transcardially perfused with 4% ice-cold paraformaldehyde (PFA) in PBS (pH 7.4). Brains were dissected out and post-fixed in 4% PFA solution at 4°C for 4 hours. Coronal sections were prepared at 20 μm with a cryostat (Leica Microsystem) or at 40 μm with a vibratome (Leica Microsystem). Sections were blocked in 10% serum and 0.1% Triton-X in PBS, and incubated with the primary antibody at 4 °C overnight. Primary antibodies used included: rabbit antibody to PARD3 (Sigma, HPA030443, 1:200 for IF and 1:1000 for WB), biotin-conjugated antibody to ISOLECTIN B4 (Sigma, L2140, 1:500), mouse antibody to SMI-312 (Biolegend, smi-312r,1:500), goat antibody to FOXP2 (Santa Cruz, sc-21069,1:200), rat antibody to CTIP2 (Abcam, ab18465,1:200), rabbit antibody to CUX1 (Santa Cruz, sc-13024,1:500), rabbit antibody to SATB2 (Abcam, ab92446,1:500), rabbit antibody to PAX6 (BioLegend, prb-278p, 1:500), mouse antibody to PAX6 (Developmental Hybridoma Bank, PAX6s, 1:50), chicken antibody to GFP (Fisher, GFP-1020, 1:1000), mouse antibody to Ki67 (BD Transduction Laboratories, 610968, 1:200), mouse antibody to TUJ1 (Covance, MMS-435P,1:500), rabbit antibody to PCNT (BioLegend, prb-432c. 1:500), mouse antibody to ZO-1 (Fisher, 33-9100, 1:500), mouse antibody to N-CADHERIN (BD Biosciences, 610920, 1:200), rabbit antibody to β-CATENIN (BD Biosciences, 610153, 1:200), rat antibody to TBR2 (eBioscience, 12-4875-12, 1:200), mouse antibody to YAP (Santa Cruz, sc-101119, 1:200), rabbit antibody to phospho-YAP (Cell Signaling, #4911, 1:200), mouse antibody to S100β (ThermoFisher, MA1-25005, 1:500), rabbit antibody to OLIG2 (Millipore, AB9610, 1:500), rat antibody to

phosphorylated histone H3 (Abcam, ab10543, 1:200), rabbit antibody to BLBP (Abcam, ab32423, 1:200), mouse antibody to P-VIMENTIN (Abcam, ab22651, 1:500), rabbit antibody to PTPRZ1 (Sigma-Aldrich, HPA015103, 1:1000), rabbit antibody to TNC (Abcam, ab108930, 1:200) and rabbit antibody to FOXJ1 (Invitrogen, 19-9965-80, 1:200). EdU staining was performed according to the manufacturer's protocol (Life Technologies). Nuclei were stained with DAPI (Sigma, D8417). Alexa fluor 488-, 546- or 647-conjugated secondary antibodies (Life Technologies, 1:1000) were used to visualize the signals of primary antibodies. For Nissl staining, the 40 μm vibratome sections were mounted onto positively charged plus slides and air-dried overnight. After the de-fat step, slides were briefly submerged in staining solution (5 g/L cresyl violet acetate in 0.3% acetic acid, Sigma-Aldrich), dehydrated, and mounted. Images were acquired with a confocal microscope (FV1000, Olympus) or a brain scanner (NanoZoomer 2.0-HT, Hamamatsu Photonics), and analyzed with Volocity (ImproVision), Neurolucida (MBF Bioscience) and Photoshop (Adobe Systems).

Animals were assigned to groups according to the genotyping results. Age-matched wild type littermates were used as the controls in all experiments. For cell density/number quantification (except the chandelier cell number quantification in chapter 3), all cells positive for the corresponding markers were counted in a 200 μm-width (embryonic neocortex), 250 μm-width (embryonic MGE) or 300 μm-width (postnatal) columnar area from the lateral ventricle to the pial surface in similar regions of the neocortex/MGE (embryonic) or the primary somatosensory cortex (postnatal). At least 3 animals in each group, and two sections in each hemisphere were analyzed in all

experiments. Both male and female mice were used in experiments. Data were presented as mean ± S.E.M. (standard error of the mean) and statistical differences were determined using Student's two-tailed t-test, Chi-square test, ANOVA test, or nonparametric Mann–Whitney test and Kruskal-Wallis test. Statistical significance was set as $p<0.05$.

As for the chandelier cell number quantification, serial coronal sections along the rostrocaudal axis were examined sequentially using Neurolucida (MBF Bioscience) installed on an upright microscope. The boundaries of the cerebral cortex and midline were manually traced and aligned. Individual chandelier cells were marked by colored dots. Based on the number of sections spanning the rostrocaudal axis of the neocortex, the total number of chandelier cells per neocortical hemisphere, as well as the number in different neocortical layers, were calculated. 5 control (10 hemispheres) and 8 *Pard3*cKO (16 hemispheres) brains were analyzed in this experiment.

Cell Cycle Exit Analysis

To label proliferating cells, pregnant females were intraperitoneally injected with 10 mg/kg body weight of EdU. At 24 hours after the injection, embryonic brains were collected, sectioned, and stained with the antibodies to EdU and Ki67. The cell cycle exit index was analyzed as the fraction of $EdU^+/Ki67^-$ cells among all EdU^+ cells.

***In vivo* RGP Division Pattern Assay**

To sparsely label dividing RGPs at the VZ surface of the embryonic cortex, serially diluted, low titer of replication-incompetent EGFP-expressing retroviruses were

injected into the lateral ventricle of embryos in utero, as previously described (Yu et al. 2009). At 24 hours after the injection, embryonic brains were collected and serially sectioned using a vibratome (Leica Microsystem). Consecutive sections covering the entire cortex were collected and stained with the antibodies against EGFP, PAX6 in neocortical assay or OLIG2 in MGE/PoA assay, and Ki67. The entire cortex or MGE/PoA was reconstructed to recover all EGFP-labeled cell pairs by Neurolucida (MBF Bioscience) on an upright microscope equipped with epifluorescence illumination and cooled charged-coupled device camera (Zeiss), and the composition of 2-cell clones were analyzed based on the triple staining results. In the neocortical experiments, $PAX6^{+}/Ki67^{+}$, $PAX6^{-}/Ki67^{+}$, and $PAX6^{-}/Ki67^{-}$ cells corresponded to RGPs, IPs, and neurons (Ns), respectively. In the MGE/PoA assays, $OLIG2^{+}/Ki67^{+}$, $OLIG2^{-}/Ki67^{+}$, and $OLIG2^{-}/Ki67^{-}$ cells corresponded to RGPs, IPs, and post-mitotic interneurons (INs), respectively.

Seizure Susceptibility Analysis

Seizure susceptibility analysis was carried out as previously described (Croquelois et al. 2009). In brief, *Pard3* cKO mice and control littermates at 3-4 months of age received intraperitoneal injections of 1 mg/kg (−)-Scopolamine methyl bromide (Sigma, S8502) in sterile saline 30 minutes prior to pilocarpine injection to reduce its peripheral cholinergic effects. Subsequently, mice were intraperitoneally injected with 300 mg/kg body weight of pilocarpine hydrochloride (Sigma, P6503) in sterile saline. Mice were observed continuously for 100 minutes after the injection, and the most severe symptom was documented every 10 minutes. Seizure severity was determined by the following 5

stages: stage 0, normal; stage 1, single jerk; stage 2, multiple jerks; stage 3, violent convulsion; stage 4, generalized seizure; and stage 5, death. Jerks refer to an uncontrolled shake of the neck and head, convulsion refer to an uncontrolled shake of the whole body, and generalized seizure refer to the loss of consciousness followed by generalized body stiffening for 30-60 seconds.

Magnetic Resonance Imaging (MRI)

Ex vivo MRI of 4% PFA fixed mouse brain specimens was performed on a horizontal 7 Tesla MR scanner (BrukerBiospin, Billerica, MA, USA) with a triple-axis gradient system. Images were acquired using a quadrature volume excitation coil (72 mm diameter) and a receive-only 4-channel phased array cryogenic coil. The specimens were imaged with skull intact and placed in a syringe filled with Fomblin to prevent tissue dehydration. High-resolution diffusion MRI data were acquired using a modified 3D diffusion-weighted gradient- and spin-echo (DW-GRASE) sequence (Wu et al. 2013) with the following parameters: echo time (TE)/repetition time (TR) = 33/400 msec; two signal averages; field of view (FOV) = 16 mm x 12.8 mm x 18 mm, resolution = 0.125 mm x 0.125 mm x 0.2 mm; two non-diffusion weighted image (b_0); 10 diffusion directions; and b = 2000 sec/mm^2. The total imaging time was approximately 1 hour for each specimen. From the diffusion MRI data, the average diffusion weighted images (DWIs) were used to manually segment the entire brain. Diffusion tensors (Basser and Jones 2002) were calculated using the log-linear fitting method implemented in DTIStudio (http://www.mristudio.org) at each pixel. The fractional anisotropy (FA) (Basser and Jones 2002) maps generated from the diffusion tensor data provided strong white matter and gray matter contrasts and were used to segment the cortex and

heterotopia. Structural volumes were calculated based on the results of manual segmentation.

REFERENCES

Afonso, C., and Henrique, D. (2006). PAR3 acts as a molecular organizer to define the apical domain of chick neuroepithelial cells. J. Cell Sci. *119*, 4293–4304.

Albertson, D.G. (1984). Formation of the first cleavage spindle in nematode embryos. Dev. Biol. *101*, 61–72.

Alexandre, P., Reugels, A.M., Barker, D., Blanc, E., and Clarke, J.D.W. (2010). Neurons derive from the more apical daughter in asymmetric divisions in the zebrafish neural tube. Nat. Neurosci. *13*, 673–679.

Anderson, S.A., Kaznowski, C.E., Horn, C., Rubenstein, J.L.R., and McConnell, S.K. (2002). Distinct origins of neocortical projection neurons and interneurons in vivo. Cereb. Cortex N. Y. N 1991 *12*, 702–709.

Angevine, J.B., and Sidman, R.L. (1961). Autoradiographic study of cell migration during histogenesis of cerebral cortex in the mouse. Nature *192*, 766–768.

Anthony, T.E., Klein, C., Fishell, G., and Heintz, N. (2004). Radial glia serve as neuronal progenitors in all regions of the central nervous system. Neuron *41*, 881–890.

Atwood, S.X., Li, M., Lee, A., Tang, J.Y., and Oro, A.E. (2013). GLI activation by atypical protein kinase C ι/λ regulates the growth of basal cell carcinomas. Nature *494*, 484–488.

Barkovich, A.J., Guerrini, R., Kuzniecky, R.I., Jackson, G.D., and Dobyns, W.B. (2012). A developmental and genetic classification for malformations of cortical development: update 2012. Brain J. Neurol. *135*, 1348–1369.

Benton, R., and St Johnston, D. (2003). A conserved oligomerization domain in drosophila Bazooka/PAR-3 is important for apical localization and epithelial polarity. Curr. Biol. CB *13*, 1330–1334.

Betizeau, M., Cortay, V., Patti, D., Pfister, S., Gautier, E., Bellemin-Ménard, A., Afanassieff, M., Huissoud, C., Douglas, R.J., Kennedy, H., et al. (2013). Precursor diversity and complexity of lineage relationships in the outer subventricular zone of the primate. Neuron *80*, 442–457.

Betschinger, J., and Knoblich, J.A. (2004). Dare to be different: asymmetric cell division in Drosophila, C. elegans and vertebrates. Curr. Biol. CB *14*, R674-685.

Bielas, S., Higginbotham, H., Koizumi, H., Tanaka, T., and Gleeson, J.G. (2004). Cortical neuronal migration mutants suggest separate but intersecting pathways. Annu. Rev. Cell Dev. Biol. *20*, 593–618.

Bilder, D., Schober, M., and Perrimon, N. (2003). Integrated activity of PDZ protein complexes regulates epithelial polarity. Nat. Cell Biol. *5*, 53–58.

Bizzotto, S., and Francis, F. (2015). Morphological and functional aspects of progenitors perturbed in cortical malformations. Front. Cell. Neurosci. *9*, 30.

Brown, K.N., Chen, S., Han, Z., Lu, C.-H., Tan, X., Zhang, X.-J., Ding, L., Lopez-Cruz, A., Saur, D., Anderson, S.A., et al. (2011). Clonal production and organization of inhibitory interneurons in the neocortex. Science *334*, 480–486.

Bultje, R.S., Castaneda-Castellanos, D.R., Jan, L.Y., Jan, Y.-N., Kriegstein, A.R., and Shi, S.-H. (2009). Mammalian Par3 regulates progenitor cell asymmetric division via notch signaling in the developing neocortex. Neuron *63*, 189–202.

Cappello, S., Attardo, A., Wu, X., Iwasato, T., Itohara, S., Wilsch-Bräuninger, M., Eilken, H.M., Rieger, M.A., Schroeder, T.T., Huttner, W.B., et al. (2006). The Rho-GTPase cdc42 regulates neural progenitor fate at the apical surface. Nat. Neurosci. *9*, 1099–1107.

Chan, J.R., Jolicoeur, C., Yamauchi, J., Elliott, J., Fawcett, J.P., Ng, B.K., and Cayouette, M. (2006). The polarity protein Par-3 directly interacts with p75NTR to regulate myelination. Science *314*, 832–836.

Chen, X., and Macara, I.G. (2005). Par-3 controls tight junction assembly through the Rac exchange factor Tiam1. Nat. Cell Biol. *7*, 262–269.

Chen, S., Chen, J., Shi, H., Wei, M., Castaneda-Castellanos, D.R., Bultje, R.S., Pei, X., Kriegstein, A.R., Zhang, M., and Shi, S.-H. (2013). Regulation of microtubule stability and organization by mammalian Par3 in specifying neuronal polarity. Dev. Cell *24*, 26–40.

Cheng, N.N., Kirby, C.M., and Kemphues, K.J. (1995). Control of cleavage spindle orientation in Caenorhabditis elegans: the role of the genes par-2 and par-3. Genetics *139*, 549–559.

Chenn, A., and McConnell, S.K. (1995). Cleavage orientation and the asymmetric inheritance of Notch1 immunoreactivity in mammalian neurogenesis. Cell *82*, 631–641.

Chenn, A., Zhang, Y.A., Chang, B.T., and McConnell, S.K. (1998). Intrinsic polarity of mammalian neuroepithelial cells. Mol. Cell. Neurosci. *11*, 183–193.

Chia, W., and Yang, X. (2002). Asymmetric division of Drosophila neural progenitors. Curr. Opin. Genet. Dev. *12*, 459–464.

Costa, M.R., Wen, G., Lepier, A., Schroeder, T., and Götz, M. (2008). Par-complex proteins promote proliferative progenitor divisions in the developing mouse cerebral cortex. Dev. Camb. Engl. *135*, 11–22.

Croquelois, A., Giuliani, F., Savary, C., Kielar, M., Amiot, C., Schenk, F., and Welker, E. (2009). Characterization of the HeCo mutant mouse: a new model of subcortical band heterotopia associated with seizures and behavioral deficits. Cereb. Cortex N. Y. N 1991 *19*, 563–575.

Deacon, T.W., Pakzaban, P., and Isacson, O. (1994). The lateral ganglionic eminence is the origin of cells committed to striatal phenotypes: neural transplantation and developmental evidence. Brain Res. *668*, 211–219.

DeFelipe, J., López-Cruz, P.L., Benavides-Piccione, R., Bielza, C., Larrañaga, P., Anderson, S., Burkhalter, A., Cauli, B., Fairén, A., Feldmeyer, D., et al. (2013). New insights into the classification and nomenclature of cortical GABAergic interneurons. Nat. Rev. Neurosci. *14*, 202–216.

Doe, C.Q., Fuerstenberg, S., and Peng, C.Y. (1998). Neural stem cells: from fly to vertebrates. J. Neurobiol. *36*, 111–127.

Dong, Z., Yang, N., Yeo, S.-Y., Chitnis, A., and Guo, S. (2012). Intralineage directional Notch signaling regulates self-renewal and differentiation of asymmetrically dividing radial glia. Neuron *74*, 65–78.

Ebnet, K., Aurrand-Lions, M., Kuhn, A., Kiefer, F., Butz, S., Zander, K., Meyer zu Brickwedde, M.-K., Suzuki, A., Imhof, B.A., and Vestweber, D. (2003). The junctional adhesion molecule (JAM) family members JAM-2 and JAM-3 associate with the cell polarity protein PAR-3: a possible role for JAMs in endothelial cell polarity. J. Cell Sci. *116*, 3879–3891.

Englund, C., Fink, A., Lau, C., Pham, D., Daza, R.A.M., Bulfone, A., Kowalczyk, T., and Hevner, R.F. (2005). Pax6, Tbr2, and Tbr1 are expressed sequentially by radial glia, intermediate progenitor cells, and postmitotic neurons in developing neocortex. J. Neurosci. Off. J. Soc. Neurosci. *25*, 247–251.

Etemad-Moghadam, B., Guo, S., and Kemphues, K.J. (1995). Asymmetrically distributed PAR-3 protein contributes to cell polarity and spindle alignment in early C. elegans embryos. Cell *83*, 743–752.

Feng, W., Wu, H., Chan, L.-N., and Zhang, M. (2007). The Par-3 NTD adopts a PB1-like structure required for Par-3 oligomerization and membrane localization. EMBO J. *26*, 2786–2796.

Feng, W., Wu, H., Chan, L.-N., and Zhang, M. (2008). Par-3-mediated junctional localization of the lipid phosphatase PTEN is required for cell polarity establishment. J. Biol. Chem. *283*, 23440–23449.

Fietz, S.A., Kelava, I., Vogt, J., Wilsch-Bräuninger, M., Stenzel, D., Fish, J.L., Corbeil, D., Riehn, A., Distler, W., Nitsch, R., et al. (2010). OSVZ progenitors of human and ferret neocortex are epithelial-like and expand by integrin signaling. Nat. Neurosci. *13*, 690–699.

Florio, M., and Huttner, W.B. (2014). Neural progenitors, neurogenesis and the evolution of the neocortex. Dev. Camb. Engl. *141*, 2182–2194.

Gabel, L.A., Manglani, M., Ibanez, N., Roberts, J., Ramos, R.L., and Rosen, G.D. (2013). Differential seizure response in two models of cortical heterotopia. Brain Res. *1494*, 84–90.

Gaiano, N., Nye, J.S., and Fishell, G. (2000). Radial glial identity is promoted by Notch1 signaling in the murine forebrain. Neuron *26*, 395–404.

Gao, L., Macara, I.G., and Joberty, G. (2002). Multiple splice variants of Par3 and of a novel related gene, Par3L, produce proteins with different binding properties. Gene *294*, 99–107.

Gao, P., Postiglione, M.P., Krieger, T.G., Hernandez, L., Wang, C., Han, Z., Streicher, C., Papusheva, E., Insolera, R., Chugh, K., et al. (2014). Deterministic progenitor behavior and unitary production of neurons in the neocortex. Cell *159*, 775–788.

García-Moreno, F., Vasistha, N.A., Trevia, N., Bourne, J.A., and Molnár, Z. (2012). Compartmentalization of cerebral cortical germinal zones in a lissencephalic primate and gyrencephalic rodent. Cereb. Cortex N. Y. N 1991 *22*, 482–492.

Geschwind, D.H., and Rakic, P. (2013). Cortical evolution: judge the brain by its cover. Neuron *80*, 633–647.

Gil-Sanz, C., Landeira, B., Ramos, C., Costa, M.R., and Müller, U. (2014). Proliferative defects and formation of a double cortex in mice lacking Mltt4 and Cdh2 in the dorsal telencephalon. J. Neurosci. Off. J. Soc. Neurosci. *34*, 10475–10487.

Goldstein, B., and Hird, S.N. (1996). Specification of the anteroposterior axis in Caenorhabditis elegans. Dev. Camb. Engl. *122*, 1467–1474.

Goldstein, B., and Macara, I.G. (2007). The PAR proteins: fundamental players in animal cell polarization. Dev. Cell *13*, 609–622.

Gorski, J.A., Talley, T., Qiu, M., Puelles, L., Rubenstein, J.L.R., and Jones, K.R. (2002). Cortical excitatory neurons and glia, but not GABAergic neurons, are produced in the Emx1-expressing lineage. J. Neurosci. Off. J. Soc. Neurosci. *22*, 6309–6314.

Götz, M., Stoykova, A., and Gruss, P. (1998). Pax6 controls radial glia differentiation in the cerebral cortex. Neuron *21*, 1031–1044.

Greig, L.C., Woodworth, M.B., Galazo, M.J., Padmanabhan, H., and Macklis, J.D. (2013). Molecular logic of neocortical projection neuron specification, development and diversity. Nat. Rev. Neurosci. *14*, 755–769.

Guo, S., and Kemphues, K.J. (1995). par-1, a gene required for establishing polarity in C. elegans embryos, encodes a putative Ser/Thr kinase that is asymmetrically distributed. Cell *81*, 611–620.

Hansen, D.V., Lui, J.H., Parker, P.R.L., and Kriegstein, A.R. (2010). Neurogenic radial glia in the outer subventricular zone of human neocortex. Nature *464*, 554–561.

Hatten, M.E. (1999). Central nervous system neuronal migration. Annu. Rev. Neurosci. *22*, 511–539.

Haubensak, W., Attardo, A., Denk, W., and Huttner, W.B. (2004). Neurons arise in the basal neuroepithelium of the early mammalian telencephalon: a major site of neurogenesis. Proc. Natl. Acad. Sci. U. S. A. *101*, 3196–3201.

Hill, D.P., and Strome, S. (1988). An analysis of the role of microfilaments in the establishment and maintenance of asymmetry in Caenorhabditis elegans zygotes. Dev. Biol. *125*, 75–84.

Hird, S.N., and White, J.G. (1993). Cortical and cytoplasmic flow polarity in early embryonic cells of Caenorhabditis elegans. J. Cell Biol. *121*, 1343–1355.

Homem, C.C.F., Repic, M., and Knoblich, J.A. (2015). Proliferation control in neural stem and progenitor cells. Nat. Rev. Neurosci. *16*, 647–659.

Hung, T.J., and Kemphues, K.J. (1999). PAR-6 is a conserved PDZ domain-containing protein that colocalizes with PAR-3 in Caenorhabditis elegans embryos. Dev. Camb. Engl. *126*, 127–135.

Hurov, J.B., Watkins, J.L., and Piwnica-Worms, H. (2004). Atypical PKC phosphorylates PAR-1 kinases to regulate localization and activity. Curr. Biol. CB *14*, 736–741.

Itoh, M., Sasaki, H., Furuse, M., Ozaki, H., Kita, T., and Tsukita, S. (2001). Junctional adhesion molecule (JAM) binds to PAR-3: a possible mechanism for the recruitment of PAR-3 to tight junctions. J. Cell Biol. *154*, 491–497.

Izumi, Y., Hirose, T., Tamai, Y., Hirai, S., Nagashima, Y., Fujimoto, T., Tabuse, Y., Kemphues, K.J., and Ohno, S. (1998). An atypical PKC directly associates and colocalizes at the epithelial tight junction with ASIP, a mammalian homologue of Caenorhabditis elegans polarity protein PAR-3. J. Cell Biol. *143*, 95–106.

Izumi, Y., Ohta, N., Itoh-Furuya, A., Fuse, N., and Matsuzaki, F. (2004). Differential functions of G protein and Baz-aPKC signaling pathways in Drosophila neuroblast asymmetric division. J. Cell Biol. *164*, 729–738.

Jan, Y.N., and Jan, L.Y. (2001). Asymmetric cell division in the Drosophila nervous system. Nat. Rev. Neurosci. *2*, 772–779.

Joberty, G., Petersen, C., Gao, L., and Macara, I.G. (2000). The cell-polarity protein Par6 links Par3 and atypical protein kinase C to Cdc42. Nat. Cell Biol. *2*, 531–539.

Johnson, D.I. (1999). Cdc42: An essential Rho-type GTPase controlling eukaryotic cell polarity. Microbiol. Mol. Biol. Rev. MMBR *63*, 54–105.

Johnson, K., and Wodarz, A. (2003). A genetic hierarchy controlling cell polarity. Nat. Cell Biol. *5*, 12–14.

Jossin, Y., Lee, M., Klezovitch, O., Kon, E., Cossard, A., Lien, W.-H., Fernandez, T.E., Cooper, J.A., and Vasioukhin, V. (2017). Llgl1 Connects Cell Polarity with Cell-Cell Adhesion in Embryonic Neural Stem Cells. Dev. Cell *41*, 481-495.e5.

Keating, H.H., and White, J.G. (1998). Centrosome dynamics in early embryos of Caenorhabditis elegans. J. Cell Sci. *111 (Pt 20)*, 3027–3033.

Kelava, I., Reillo, I., Murayama, A.Y., Kalinka, A.T., Stenzel, D., Tomancak, P., Matsuzaki, F., Lebrand, C., Sasaki, E., Schwamborn, J.C., et al. (2012). Abundant occurrence of basal radial glia in the subventricular zone of embryonic neocortex of a lissencephalic primate, the common marmoset Callithrix jacchus. Cereb. Cortex N. Y. N 1991 *22*, 469–481.

Kemphues, K. (2000). PARsing embryonic polarity. Cell *101*, 345–348.

Kemphues, K.J., Priess, J.R., Morton, D.G., and Cheng, N.S. (1988). Identification of genes required for cytoplasmic localization in early C. elegans embryos. Cell *52*, 311–320.

Kessaris, N., Fogarty, M., Iannarelli, P., Grist, M., Wegner, M., and Richardson, W.D. (2006). Competing waves of oligodendrocytes in the forebrain and postnatal elimination of an embryonic lineage. Nat. Neurosci. *9*, 173–179.

Kielar, M., Tuy, F.P.D., Bizzotto, S., Lebrand, C., de Juan Romero, C., Poirier, K., Oegema, R., Mancini, G.M., Bahi-Buisson, N., Olaso, R., et al. (2014). Mutations in Eml1 lead to ectopic progenitors and neuronal heterotopia in mouse and human. Nat. Neurosci. *17*, 923–933.

Knoblich, J.A. (2008). Mechanisms of asymmetric stem cell division. Cell *132*, 583–597.

Krahn, M.P., Klopfenstein, D.R., Fischer, N., and Wodarz, A. (2010). Membrane targeting of Bazooka/PAR-3 is mediated by direct binding to phosphoinositide lipids. Curr. Biol. CB *20*, 636–642.

Kriegstein, A., and Alvarez-Buylla, A. (2009). The glial nature of embryonic and adult neural stem cells. Annu. Rev. Neurosci. *32*, 149–184.

Kriegstein, A.R., and Götz, M. (2003). Radial glia diversity: a matter of cell fate. Glia *43*, 37–43.

Kuchinke, U., Grawe, F., and Knust, E. (1998). Control of spindle orientation in Drosophila by the Par-3-related PDZ-domain protein Bazooka. Curr. Biol. CB *8*, 1357–1365.

Kwan, K.Y., Sestan, N., and Anton, E.S. (2012). Transcriptional co-regulation of neuronal migration and laminar identity in the neocortex. Dev. Camb. Engl. *139*, 1535–1546.

Levitan, D.J., Boyd, L., Mello, C.C., Kemphues, K.J., and Stinchcomb, D.T. (1994). par-2, a gene required for blastomere asymmetry in Caenorhabditis elegans, encodes zinc-finger and ATP-binding motifs. Proc. Natl. Acad. Sci. U. S. A. *91*, 6108–6112.

Li, B., Kim, H., Beers, M., and Kemphues, K. (2010). Different domains of C. elegans PAR-3 are required at different times in development. Dev. Biol. *344*, 745–757.

Li, H.S., Wang, D., Shen, Q., Schonemann, M.D., Gorski, J.A., Jones, K.R., Temple, S., Jan, L.Y., and Jan, Y.N. (2003). Inactivation of Numb and Numblike in embryonic dorsal forebrain impairs neurogenesis and disrupts cortical morphogenesis. Neuron *40*, 1105–1118.

Li, Y., Hibbs, M.A., Gard, A.L., Shylo, N.A., and Yun, K. (2012). Genome-wide analysis of N1ICD/RBPJ targets in vivo reveals direct transcriptional regulation of Wnt, SHH, and hippo pathway effectors by Notch1. Stem Cells Dayt. Ohio *30*, 741–752.

Lin, D., Edwards, A.S., Fawcett, J.P., Mbamalu, G., Scott, J.D., and Pawson, T. (2000). A mammalian PAR-3-PAR-6 complex implicated in Cdc42/Rac1 and aPKC signalling and cell polarity. Nat. Cell Biol. *2*, 540–547.

Liu, W.A., Chen, S., Li, Z., Lee, C.H., Mirzaa, G., Dobyns, W.B., Ross, M.E., Zhang, J., and Shi, S.-H. (2018). PARD3 dysfunction in conjunction with dynamic HIPPO signaling drives cortical enlargement with massive heterotopia. Genes Dev. *32*, 763–780.

Luskin, M.B., Parnavelas, J.G., and Barfield, J.A. (1993). Neurons, astrocytes, and oligodendrocytes of the rat cerebral cortex originate from separate progenitor cells: an

ultrastructural analysis of clonally related cells. J. Neurosci. Off. J. Soc. Neurosci. *13*, 1730–1750.

Lv, X.-B., Liu, C.-Y., Wang, Z., Sun, Y.-P., Xiong, Y., Lei, Q.-Y., and Guan, K.-L. (2015). PARD3 induces TAZ activation and cell growth by promoting LATS1 and PP1 interaction. EMBO Rep. *16*, 975–985.

Maass, W., Natschläger, T., and Markram, H. (2004). Fading memory and kernel properties of generic cortical microcircuit models. J. Physiol. Paris *98*, 315–330.

Madisen, L., Zwingman, T.A., Sunkin, S.M., Oh, S.W., Zariwala, H.A., Gu, H., Ng, L.L., Palmiter, R.D., Hawrylycz, M.J., Jones, A.R., et al. (2010). A robust and high-throughput Cre reporting and characterization system for the whole mouse brain. Nat. Neurosci. *13*, 133–140.

Malatesta, P., Hartfuss, E., and Götz, M. (2000). Isolation of radial glial cells by fluorescent-activated cell sorting reveals a neuronal lineage. Dev. Camb. Engl. *127*, 5253–5263.

Manabe, N., Hirai, S.-I., Imai, F., Nakanishi, H., Takai, Y., and Ohno, S. (2002). Association of ASIP/mPAR-3 with adherens junctions of mouse neuroepithelial cells. Dev. Dyn. Off. Publ. Am. Assoc. Anat. *225*, 61–69.

Marín, O., and Rubenstein, J.L.R. (2003). Cell migration in the forebrain. Annu. Rev. Neurosci. *26*, 441–483.

Markram, H., Toledo-Rodriguez, M., Wang, Y., Gupta, A., Silberberg, G., and Wu, C. (2004). Interneurons of the neocortical inhibitory system. Nat. Rev. Neurosci. *5*, 793–807.

Miyata, T., Kawaguchi, A., Okano, H., and Ogawa, M. (2001). Asymmetric inheritance of radial glial fibers by cortical neurons. Neuron *31*, 727–741.

Miyoshi, G., Butt, S.J.B., Takebayashi, H., and Fishell, G. (2007). Physiologically distinct temporal cohorts of cortical interneurons arise from telencephalic Olig2-expressing precursors. J. Neurosci. Off. J. Soc. Neurosci. *27*, 7786–7798.

Mizuno, K., Suzuki, A., Hirose, T., Kitamura, K., Kutsuzawa, K., Futaki, M., Amano, Y., and Ohno, S. (2003). Self-association of PAR-3-mediated by the conserved N-terminal domain contributes to the development of epithelial tight junctions. J. Biol. Chem. *278*, 31240–31250.

Morton, D.G., Roos, J.M., and Kemphues, K.J. (1992). par-4, a gene required for cytoplasmic localization and determination of specific cell types in Caenorhabditis elegans embryogenesis. Genetics *130*, 771–790.

Murtaugh, L.C., Stanger, B.Z., Kwan, K.M., and Melton, D.A. (2003). Notch signaling controls multiple steps of pancreatic differentiation. Proc. Natl. Acad. Sci. U. S. A. *100*, 14920–14925.

Nakaya, M., Fukui, A., Izumi, Y., Akimoto, K., Asashima, M., and Ohno, S. (2000). Meiotic maturation induces animal-vegetal asymmetric distribution of aPKC and ASIP/PAR-3 in Xenopus oocytes. Dev. Camb. Engl. *127*, 5021–5031.

Nance, J., Munro, E.M., and Priess, J.R. (2003). C. elegans PAR-3 and PAR-6 are required for apicobasal asymmetries associated with cell adhesion and gastrulation. Dev. Camb. Engl. *130*, 5339–5350.

Nishimura, T., and Kaibuchi, K. (2007). Numb controls integrin endocytosis for directional cell migration with aPKC and PAR-3. Dev. Cell *13*, 15–28.

Nishimura, T., Kato, K., Yamaguchi, T., Fukata, Y., Ohno, S., and Kaibuchi, K. (2004). Role of the PAR-3-KIF3 complex in the establishment of neuronal polarity. Nat. Cell Biol. *6*, 328–334.

Nishimura, T., Yamaguchi, T., Kato, K., Yoshizawa, M., Nabeshima, Y., Ohno, S., Hoshino, M., and Kaibuchi, K. (2005). PAR-6-PAR-3 mediates Cdc42-induced Rac activation through the Rac GEFs STEF/Tiam1. Nat. Cell Biol. *7*, 270–277.

Noctor, S.C., Flint, A.C., Weissman, T.A., Dammerman, R.S., and Kriegstein, A.R. (2001). Neurons derived from radial glial cells establish radial units in neocortex. Nature *409*, 714–720.

Noctor, S.C., Martínez-Cerdeño, V., Ivic, L., and Kriegstein, A.R. (2004). Cortical neurons arise in symmetric and asymmetric division zones and migrate through specific phases. Nat. Neurosci. *7*, 136–144.

Nowotschin, S., Xenopoulos, P., Schrode, N., and Hadjantonakis, A.-K. (2013). A bright single-cell resolution live imaging reporter of Notch signaling in the mouse. BMC Dev. Biol. *13*, 15.

Ohshiro, T., Yagami, T., Zhang, C., and Matsuzaki, F. (2000). Role of cortical tumour-suppressor proteins in asymmetric division of Drosophila neuroblast. Nature *408*, 593–596.

Olsson, M., Campbell, K., Wictorin, K., and Björklund, A. (1995). Projection neurons in fetal striatal transplants are predominantly derived from the lateral ganglionic eminence. Neuroscience *69*, 1169–1182.

Olsson, M., Björklund, A., and Campbell, K. (1998). Early specification of striatal projection neurons and interneuronal subtypes in the lateral and medial ganglionic eminence. Neuroscience *84*, 867–876.

Pan, D. (2010). The hippo signaling pathway in development and cancer. Dev. Cell *19*, 491–505.

Parmentier, M.L., Woods, D., Greig, S., Phan, P.G., Radovic, A., Bryant, P., and O'Kane, C.J. (2000). Rapsynoid/partner of inscuteable controls asymmetric division of larval neuroblasts in Drosophila. J. Neurosci. Off. J. Soc. Neurosci. *20*, RC84.

Parnavelas, J.G., Barfield, J.A., Franke, E., and Luskin, M.B. (1991). Separate progenitor cells give rise to pyramidal and nonpyramidal neurons in the rat telencephalon. Cereb. Cortex N. Y. N 1991 *1*, 463–468.

Patalano, S., Prulière, G., Prodon, F., Paix, A., Dru, P., Sardet, C., and Chenevert, J. (2006). The aPKC-PAR-6-PAR-3 cell polarity complex localizes to the centrosome attracting body, a macroscopic cortical structure responsible for asymmetric divisions in the early ascidian embryo. J. Cell Sci. *119*, 1592–1603.

Peng, C.Y., Manning, L., Albertson, R., and Doe, C.Q. (2000). The tumour-suppressor genes lgl and dlg regulate basal protein targeting in Drosophila neuroblasts. Nature *408*, 596–600.

Petersen, P.H., Zou, K., Krauss, S., and Zhong, W. (2004). Continuing role for mouse Numb and Numbl in maintaining progenitor cells during cortical neurogenesis. Nat. Neurosci. *7*, 803–811.

Petilla Interneuron Nomenclature Group, Ascoli, G.A., Alonso-Nanclares, L., Anderson, S.A., Barrionuevo, G., Benavides-Piccione, R., Burkhalter, A., Buzsáki, G., Cauli, B., Defelipe, J., et al. (2008). Petilla terminology: nomenclature of features of GABAergic interneurons of the cerebral cortex. Nat. Rev. Neurosci. *9*, 557–568.

Petryniak, M.A., Potter, G.B., Rowitch, D.H., and Rubenstein, J.L.R. (2007). Dlx1 and Dlx2 control neuronal versus oligodendroglial cell fate acquisition in the developing forebrain. Neuron *55*, 417–433.

Pollen, A.A., Nowakowski, T.J., Chen, J., Retallack, H., Sandoval-Espinosa, C., Nicholas, C.R., Shuga, J., Liu, S.J., Oldham, M.C., Diaz, A., et al. (2015). Molecular identity of human outer radial glia during cortical development. Cell *163*, 55–67.

Pontious, A., Kowalczyk, T., Englund, C., and Hevner, R.F. (2008). Role of intermediate progenitor cells in cerebral cortex development. Dev. Neurosci. *30*, 24–32.

Rakic, P. (1971). Guidance of neurons migrating to the fetal monkey neocortex. Brain Res. *33*, 471–476.

Rakic, P. (1988). Specification of cerebral cortical areas. Science *241*, 170–176.

Rakic, P. (2003). Developmental and evolutionary adaptations of cortical radial glia. Cereb. Cortex N. Y. N 1991 *13*, 541–549.

Rakic, P. (2009). Evolution of the neocortex: a perspective from developmental biology. Nat. Rev. Neurosci. *10*, 724–735.

Reginensi, A., Scott, R.P., Gregorieff, A., Bagherie-Lachidan, M., Chung, C., Lim, D.-S., Pawson, T., Wrana, J., and McNeill, H. (2013). Yap- and Cdc42-dependent nephrogenesis and morphogenesis during mouse kidney development. PLoS Genet. *9*, e1003380.

Reillo, I., de Juan Romero, C., García-Cabezas, M.Á., and Borrell, V. (2011). A role for intermediate radial glia in the tangential expansion of the mammalian cerebral cortex. Cereb. Cortex N. Y. N 1991 *21*, 1674–1694.

Rose, L.S., Lamb, M.L., Hird, S.N., and Kemphues, K.J. (1995). Pseudocleavage is dispensable for polarity and development in C. elegans embryos. Dev. Biol. *168*, 479–489.

Ross, M.E., and Walsh, C.A. (2001). Human brain malformations and their lessons for neuronal migration. Annu. Rev. Neurosci. *24*, 1041–1070.

Rudy, B., Fishell, G., Lee, S., and Hjerling-Leffler, J. (2011). Three groups of interneurons account for nearly 100% of neocortical GABAergic neurons. Dev. Neurobiol. *71*, 45–61.

Sadler, P.L., and Shakes, D.C. (2000). Anucleate Caenorhabditis elegans sperm can crawl, fertilize oocytes and direct anterior-posterior polarization of the 1-cell embryo. Dev. Camb. Engl. *127*, 355–366.

Schaefer, M., Shevchenko, A., Shevchenko, A., and Knoblich, J.A. (2000). A protein complex containing Inscuteable and the Galpha-binding protein Pins orients asymmetric cell divisions in Drosophila. Curr. Biol. CB *10*, 353–362.

Schmid, M.-T., Weinandy, F., Wilsch-Bräuninger, M., Huttner, W.B., Cappello, S., and Götz, M. (2014). The role of α-E-catenin in cerebral cortex development: radial glia specific effect on neuronal migration. Front. Cell. Neurosci. *8*, 215.

Schober, M., Schaefer, M., and Knoblich, J.A. (1999). Bazooka recruits Inscuteable to orient asymmetric cell divisions in Drosophila neuroblasts. Nature *402*, 548–551.

Sin, O., Michels, H., and Nollen, E.A.A. (2014). Genetic screens in Caenorhabditis elegans models for neurodegenerative diseases. Biochim. Biophys. Acta *1842*, 1951–1959.

von Stein, W., Ramrath, A., Grimm, A., Müller-Borg, M., and Wodarz, A. (2005). Direct association of Bazooka/PAR-3 with the lipid phosphatase PTEN reveals a link

between the PAR/aPKC complex and phosphoinositide signaling. Dev. Camb. Engl. *132*, 1675–1686.

Stenman, J., Toresson, H., and Campbell, K. (2003). Identification of two distinct progenitor populations in the lateral ganglionic eminence: implications for striatal and olfactory bulb neurogenesis. J. Neurosci. Off. J. Soc. Neurosci. *23*, 167–174.

Strome, S., and Wood, W.B. (1982). Immunofluorescence visualization of germ-line-specific cytoplasmic granules in embryos, larvae, and adults of Caenorhabditis elegans. Proc. Natl. Acad. Sci. U. S. A. *79*, 1558–1562.

Strome, S., and Wood, W.B. (1983). Generation of asymmetry and segregation of germ-line granules in early C. elegans embryos. Cell *35*, 15–25.

Sulston, J.E., Schierenberg, E., White, J.G., and Thomson, J.N. (1983). The embryonic cell lineage of the nematode Caenorhabditis elegans. Dev. Biol. *100*, 64–119.

Suzuki, A., Yamanaka, T., Hirose, T., Manabe, N., Mizuno, K., Shimizu, M., Akimoto, K., Izumi, Y., Ohnishi, T., and Ohno, S. (2001). Atypical protein kinase C is involved in the evolutionarily conserved par protein complex and plays a critical role in establishing epithelia-specific junctional structures. J. Cell Biol. *152*, 1183–1196.

Tabuse, Y., Izumi, Y., Piano, F., Kemphues, K.J., Miwa, J., and Ohno, S. (1998). Atypical protein kinase C cooperates with PAR-3 to establish embryonic polarity in Caenorhabditis elegans. Dev. Camb. Engl. *125*, 3607–3614.

Takekuni, K., Ikeda, W., Fujito, T., Morimoto, K., Takeuchi, M., Monden, M., and Takai, Y. (2003). Direct binding of cell polarity protein PAR-3 to cell-cell adhesion molecule nectin at neuroepithelial cells of developing mouse. J. Biol. Chem. *278*, 5497–5500.

Tamamaki, N., Nakamura, K., Okamoto, K., and Kaneko, T. (2001). Radial glia is a progenitor of neocortical neurons in the developing cerebral cortex. Neurosci. Res. *41*, 51–60.

Tan, S.S., Kalloniatis, M., Sturm, K., Tam, P.P., Reese, B.E., and Faulkner-Jones, B. (1998). Separate progenitors for radial and tangential cell dispersion during development of the cerebral neocortex. Neuron *21*, 295–304.

Tan, X., Liu, W.A., Zhang, X.-J., Shi, W., Ren, S.-Q., Li, Z., Brown, K.N., and Shi, S.-H. (2016). Vascular Influence on Ventral Telencephalic Progenitors and Neocortical Interneuron Production. Dev. Cell *36*, 624–638.

Tanentzapf, G., and Tepass, U. (2003). Interactions between the crumbs, lethal giant larvae and bazooka pathways in epithelial polarization. Nat. Cell Biol. *5*, 46–52.

Tassan, J.-P., and Le Goff, X. (2004). An overview of the KIN1/PAR-1/MARK kinase family. Biol. Cell *96*, 193–199.

Thomsen, E.R., Mich, J.K., Yao, Z., Hodge, R.D., Doyle, A.M., Jang, S., Shehata, S.I., Nelson, A.M., Shapovalova, N.V., Levi, B.P., et al. (2016). Fixed single-cell transcriptomic characterization of human radial glial diversity. Nat. Methods *13*, 87–93.

Traweger, A., Wiggin, G., Taylor, L., Tate, S.A., Metalnikov, P., and Pawson, T. (2008). Protein phosphatase 1 regulates the phosphorylation state of the polarity scaffold Par-3. Proc. Natl. Acad. Sci. U. S. A. *105*, 10402–10407.

Tripathi, R.B., Rivers, L.E., Young, K.M., Jamen, F., and Richardson, W.D. (2010). NG2 glia generate new oligodendrocytes but few astrocytes in a murine experimental autoimmune encephalomyelitis model of demyelinating disease. J. Neurosci. Off. J. Soc. Neurosci. *30*, 16383–16390.

von Trotha, J.W., Campos-Ortega, J.A., and Reugels, A.M. (2006). Apical localization of ASIP/PAR-3:EGFP in zebrafish neuroepithelial cells involves the oligomerization domain CR1, the PDZ domains, and the C-terminal portion of the protein. Dev. Dyn. Off. Publ. Am. Assoc. Anat. *235*, 967–977.

Wang, X., Tsai, J.-W., LaMonica, B., and Kriegstein, A.R. (2011). A new subtype of progenitor cell in the mouse embryonic neocortex. Nat. Neurosci. *14*, 555–561.

Watrin, F., Manent, J.-B., Cardoso, C., and Represa, A. (2015). Causes and consequences of gray matter heterotopia. CNS Neurosci. Ther. *21*, 112–122.

Watts, J.L., Etemad-Moghadam, B., Guo, S., Boyd, L., Draper, B.W., Mello, C.C., Priess, J.R., and Kemphues, K.J. (1996). par-6, a gene involved in the establishment of asymmetry in early C. elegans embryos, mediates the asymmetric localization of PAR-3. Dev. Camb. Engl. *122*, 3133–3140.

Wichterle, H., Turnbull, D.H., Nery, S., Fishell, G., and Alvarez-Buylla, A. (2001). In utero fate mapping reveals distinct migratory pathways and fates of neurons born in the mammalian basal forebrain. Dev. Camb. Engl. *128*, 3759–3771.

Wodarz, A., and Huttner, W.B. (2003). Asymmetric cell division during neurogenesis in Drosophila and vertebrates. Mech. Dev. *120*, 1297–1309.

Wodarz, A., Ramrath, A., Kuchinke, U., and Knust, E. (1999). Bazooka provides an apical cue for Inscuteable localization in Drosophila neuroblasts. Nature *402*, 544–547.

Wonders, C.P., and Anderson, S.A. (2006). The origin and specification of cortical interneurons. Nat. Rev. Neurosci. *7*, 687–696.

Wu, H., Feng, W., Chen, J., Chan, L.-N., Huang, S., and Zhang, M. (2007). PDZ domains of Par-3 as potential phosphoinositide signaling integrators. Mol. Cell *28*, 886–898.

Xu, Q., Cobos, I., De La Cruz, E., Rubenstein, J.L., and Anderson, S.A. (2004). Origins of cortical interneuron subtypes. J. Neurosci. Off. J. Soc. Neurosci. *24*, 2612–2622.

Xu, Q., Tam, M., and Anderson, S.A. (2008). Fate mapping Nkx2.1-lineage cells in the mouse telencephalon. J. Comp. Neurol. *506*, 16–29.

Xu, Q., Guo, L., Moore, H., Waclaw, R.R., Campbell, K., and Anderson, S.A. (2010). Sonic hedgehog signaling confers ventral telencephalic progenitors with distinct cortical interneuron fates. Neuron *65*, 328–340.

Yu, C.G., and Harris, T.J.C. (2012). Interactions between the PDZ domains of Bazooka (Par-3) and phosphatidic acid: in vitro characterization and role in epithelial development. Mol. Biol. Cell *23*, 3743–3753.

Yu, F.-X., and Guan, K.-L. (2013). The Hippo pathway: regulators and regulations. Genes Dev. *27*, 355–371.

Yu, F., Morin, X., Cai, Y., Yang, X., and Chia, W. (2000). Analysis of partner of inscuteable, a novel player of Drosophila asymmetric divisions, reveals two distinct steps in inscuteable apical localization. Cell *100*, 399–409.

Zhang, H., and Macara, I.G. (2006). The polarity protein PAR-3 and TIAM1 cooperate in dendritic spine morphogenesis. Nat. Cell Biol. *8*, 227–237.

Zhang, P., Wang, S., Wang, S., Qiao, J., Zhang, L., Zhang, Z., and Chen, Z. (2016). Dual function of partitioning-defective 3 in the regulation of YAP phosphorylation and activation. Cell Discov. *2*, 16021.